12-2006

Hydrodynamic Wave Contributions to Combustion Instability in Rockets

Esam M. T. Abu-Irshaid
University of Tennessee, Knoxville

To the Graduate Council:

I am submitting herewith a dissertation written by Esam M. T. Abu-Irshaid entitled "Hydrodynamic Wave Contributions to Combustion Instability in Rockets." I have examined the final electronic copy of this dissertation for form and content and recommend that it be accepted in partial fulfillment of the requirements for the degree of Doctor of Philosophy, with a major in Mechanical Engineering.

Joseph Majdalani, Major Professor

We have read this dissertation and recommend its acceptance:

Gary A. Flandro, John Steinhoff, Kenneth Kimble

Accepted for the Council:
Carolyn R. Hodges

Vice Provost and Dean of the Graduate School

(Original signatures are on file with official student records.)

To the Graduate Council:

I am submitting herewith a dissertation written by Esam M. T. Abu-Irshaid entitled "Hydrodynamic Wave Contributions to Combustion Instability in Rockets". I have examined the final paper copy of this dissertation for form and content and recommend that it be accepted in partial fulfillment of the requirements for the degree of Doctor of Philosophy, with a major in Mechanical Engineering.

Joseph Majdalani, Major Professor

We have read this dissertation
and recommend its acceptance:

Gary A. Flandro

John Steinhoff

Kenneth Kimble

Accepted for the Council:

Linda T. Painter
Interim Dean of Graduate Students

Hydrodynamic Wave Contributions to Combustion Instability in Rockets

A Dissertation

Presented for the

Doctor of Philosophy Degree

University of Tennessee, Knoxville

Esam M. T. Abu-Irshaid

December, 2006

Dedication

All praise and gratitude is due to God who has guided me through this accomplishment as I would not have ultimately gotten this far had it not been for his guidance. During the writing of my dissertation, I have been assisted morally and academically. I thus would like to dedicate my thesis to my family: My parents who have sacrificed every possible event and opportunity in order for me to reach this point in my life and who have unconditionally supported me throughout this journey; my brother, Osama, whose wisdom I have not seen the likes of which and whose opinions have inspired my thoughts; the rest of my family who have never turned me down and have always been there for me.

Acknowledgments

I would like to express my most sincere gratitude to my committee chairman, Dr. Joseph Majdalani, who gave the chance to work on this project, for supporting me through the NSF grant, and for providing me with assistance; my work advisor, Dr. Gary Flandro whose step-by-step guidance, experiences in the field of combustion Instability, and availability at any time was instrumental to the success of this project; Dr. John Steinhoff whose views were instructive to my project; Dr. Kimble who has kindly accepted to participate in my committee and for his contributions; Dr. Grégoire Casalis who, while at France, was the first to have introduced us to the hydrodynamic instability; to all of my friends and beloved ones for their continuous thoughtful and warm wishes. I would also like to especially thank Sean Fischbach for his enlightening efforts with my research in addition to his final touches in writing this dissertation. So to all of those who have been there for me, thank you.

Abstract

Experimental measurements suggest that a new source of instability in rocket motors is due to hydrodynamic disturbances. These disturbances, if ignored, could impact our assessment of rocket motor performance. In this work, the corresponding problem of hydrodynamic instability is considered. A mathematical model for these disturbances is carried out by perturbing the continuity and momentum equations. A one dimensional model which represents the wave disturbances in time and space is implemented to quantify the amplification rate, in time or space, and the wave amplitude. The only available measurements of these disturbances arise in cold flow experiments that simulate the gas dynamics in a solid rocket motor and where no real combustion takes place. The reason for cold flow experiments is the difficulty in measuring the hydrodynamic disturbances in real rockets. To gain better understanding of the interaction between hydrodynamic and combustion driven disturbances, a new approach is implemented that accounts for hydrodynamic effects on the combustion instability net system amplitude. In this model the impact of spatial hydrodynamic vortices in solid rocket motors is projected on the net system amplitude calculations. Results show that some factors play a significant role in controlling the hydrodynamic disturbances. These factors include the injection Mach number, chamber aspect ratio, admittance function and the tangential wave number. Here, the influence of each of these factors is examined. Finally, the hydrodynamic energy density is calculated and found to be small in comparison to the vortical-acoustic one.

Foreword

This report is the dissertation submitted by Esam Abu-Irshaid in partial fulfillment of the requirement for the degree of Doctor of Philosophy, December 2006. In addition to myself as chairman, the examining committee consisted of Professors G. A. Flandro, J. S. Steinhoff, and K. R. Kimble (Mathematics). In addition, Professor G. Casalis (ONERA/SUPAERO) was involved in this project.

This work was supported by the National Science Foundation under NSF Contract No. 0239267.

J. Majdalani

October 2006

Table of Contents

List of Tables

List of Figures

Nomenclature

a_0	=	isentropic speed of sound
A	=	wave amplitude
A_0	=	hydrodynamic initial amplitude
f	=	physical frequency based on $\omega_r U_w/(2\pi R) = k_m\, a_0/(2\pi R)$
l	=	motor aspect ratio L/R
L	=	chamber length
M	=	Mach number
n	=	exponential spatial amplification rate
q	=	tangential wave number
R	=	chamber radius
R_0	=	universal gas constant
Re	=	Reynolds number $U_w R/\nu$
$\boldsymbol{U}$	=	steady state (basic) flow
$\boldsymbol{V}$	=	total instantaneous velocity
ε	=	net pressure amplitude
γ	=	ratio of specific heats
σ_r	=	longitudinal wave number
σ_i	=	amplification of the wave amplitude with respect to time
$\boldsymbol{\Omega}$	=	steady state vorticity

ω	=	total instantaneous vorticity
ω_r	=	circular frequency
ω_i	=	amplification of the wave amplitude with respect to space

Subscripts and Symbols

0	=	reference property (usually, stagnation value at chamber origin)
h	=	headwall property
i, r	=	imaginary or real parts
w	=	sidewall property
$\bar{}$	=	dimensional property

1. Introduction

1.1. Brief History of Combustion Instability

Solid propellant rocket motors frequently exhibit unsteady behavior during their operation. The frequencies of pressure fluctuations observed in the cavity closely match those corresponding to the classical acoustic modes [1]. These gas oscillations can in turn lead to harmful consequences within the motor structure and flight vehicle. When the waves grow to moderate amplitudes, they can steepen into shock-like waves. Both mechanisms can severely damage the rocket motor causing propulsive failure and sometimes loss of payload during the flight.

Vortical and tangential combustion waves may also impose large roll torques on the rocket case and nozzle [2]; these, of course, can adversely affect the performance of the system. Moreover, specific impulse, burning rate and exhaust velocity can be affected. Another severe problem is the drastic increment in the pressure chamber (DC shift) that often accompanies nonlinear combustion instability [3]. The sudden increment in the pressure, if not taken into consideration, can result in rocket deflagration. To date, much progress has been achieved since the problem of combustion instability was first identified over five decades ago. Nonetheless the combustion instability remains the most difficult and troublesome system development problem faced by for rocket designers.

To track the origins of the problem of combustion instability, one must start from the burning surface where the oscillation waves originate. Their growth and evolution are due to the interaction between the combustion process and the gas dynamics in the cavity.

Perhaps the earliest effort to investigate the combustion instability problem in a liquid rocket engine was initiated in the fifties by Crocco and Cheng [4,5]. The first attempt to evaluate the growth or decay rate of combustion driven oscillations similarly through the application of the energy balance methods was carried out at the Johns Hopkins University by Hart and McClure [6]. Their model was later shown to fail to distinguish between acoustic (irrotational) and unsteady rotational flow effects. An alternative approach which has gained widespread acceptance is the perturbed acoustic wave equation method mainly attributed to Culick. At the California Institute of Technology [7-10] Culick applies the mathematical expansion procedure by starting with the full inviscid equations of fluid mechanics; he then develops the equations that govern the acoustic oscillations and their interactions with the mean flowfield. Based on his model, the growth or decay rate of an acoustic wave can be determined by whether the acoustic energy increases or decays. In this model, however, pure acoustics only are considered. In 1972, Culick [8-10] compares results from his 1-D and 3-D models and observes that the 3-D model is lacking terms that appear in the one-dimensional results (in particular, a term he calls "flow turning"). He argues that this inconsistency must be corrected by adding the missing terms to the 3-D model in an ad hoc manner. He refers to this process as "patching."

In a later and more careful analysis, Flandro [11,12] shows that the absence of the flow turning in the multidimensional approach is due to the failure to impose the no slip condition at the burning propellant surfaces. Furthermore, he demonstrates that by using the corrected unsteady radial velocity, a new driving term is created. Hence, the system is significantly less stable than predicted by the earlier theories. The origins of flow turning

are also clarified and it is demonstrated that rotational flow effects brought into play by using the correct boundary conditions lead to this phenomenon. Independent analysis by Majdalani and Van Moorhem [13-15] confirm the same. A complete representation of the vortical-acoustic wave motion in a solid rocket motor is later advanced by Majdalani and Flandro [16] for an arbitrary mean flow profile. Flandro [11,12] also argues the need to incorporate these rotational terms due to the poor performance of the standard stability prediction (SSP) code based on Culick's earlier theory. This is the most widely used software to assess the stability of solid propellant rocket motors. Flandro and Majdalani [17,18] also point out that a purely irrotational acoustic model does not account for the total energy gains or losses in a rocket motor. They emphasize that unsteady vorticity terms have to be incorporated in Culick's fundamental model [7,10,19] in order to satisfy the no slip condition at the propellant surface. New terms are derived that are equal in magnitude but opposite in direction to the so called *flow turning term*.

The portential importance of hydrodynamic instability and the resulting vortex shedding within combustion chambers was first recognized by Flandro and Jacobs [41] and was the subject of many studies. The first serious attempt to include these effects in rocket combustion stability assessments was by Flandro [42]. He used these ideas in solving actual pressure oscillation problems in the Minuteman III (third stage) rocket motor by aerodynamic streamlining of the internal propellant surface geometry to avoid vortex shedding. The work presents a more detailed representation of these effects, and in particular, addresses effects of the natural hydrodynamic instability of injection driven flows. In more recent work, Flandro, Majdalani and French [20] advance the classical Culick model by incorporating several rotational corrections in the Standard Stability

Prediction (SSP) code. However, considering that the propellant grain in a modern rocket has a complex geometry, the volume integrals are computationally very expensive to evaluate. Fischbach, Flandro and Majdalani [21] convert the ten stability growth rates from volume to surface integral form. Fischbach, Majdalani and Flandro [22] also formulate the equivalent problem in the slab rocket motor. Their work is further advanced and the terms converted to acoustic forms; as shown by Fischbach, Majdalani and Flandro [23], this makes them amenable to direct implementation in SSP.

1.2. Hydrodynamic Instability

The problem of hydrodynamic instability was first recognized and formulated in the nineteenth century, notably by Helmholtz, Kelvin, Rayleigh and Reynolds. It would be difficult to introduce these problems more clearly than in Osborn Reynolds' own description of his 1883 classic series of experiments on the instability of flow in a pipe.

Reynolds in his experiments shows that the laminar flow breaks down when a certain quantity exceeds a critical limit. This quantity is defined as the Reynolds number, a dimensionless quantity, relating the inertial and viscous forces. Several methods of analyzing the stability of flows were formulated in Reynolds' time.

Broadly speaking, one may say that the instability occurs because there are some disturbances of the equilibrium of the external forces, inertial and viscous forces. However, in the absence of external forces or viscosity, a fluid moves according to the equilibrium between its inertial and internal stresses. A small disturbance may upset the equilibrium. The analysis of linear hydrodynamic instability does not predict turbulence. In fact, turbulence is an experimentally observed fact. It has not been proven mathematically that turbulent flow is the proper stable state at high Reynolds numbers.

Another important observation is transition, which is defined as the change over a certain Reynolds number range from a laminar flow to turbulence. Although the linear stability theory predicts the breakdown of the fluid motion, it does not guarantee that the flow will transition to a fully turbulent field. It may go from one laminar state to another.

1.3. Scope of this Study

In this study of hydrodynamic instability in an SRM, three-dimensional linear instability theory is applied to an idealized representation of a full-length, cylindrical, hybrid rocket. The analysis also considers a long, full-length solid rocket motor (SRM) with reactive headwall. The Local Non Parallel (LNP) approach is used in which all of the non-zero components of the basic flow are retained in the viscous Navier-Stokes equations. In recent studies, Casalis and co-workers [24-29] have implemented this approach while investigating both the porous channel and tube; their mean flow expressions due to Taylor [30] and Culick [31] are often used to describe the bulk gas motion in slab and circular-port rocket motors. Their results have been corroborated by cold-flow experiments and have helped to point out the critical abscissas beyond which the flow becomes unstable [32]. These were found to occur around 5 and 3 for the planar and axisymmetric cases, respectively. This investigation follows suit by applying the LNP approach to a similar geometric setting that is germane to the conventional hybrid grain shape and that of a solid propellant motor with reactive headend. Here the headwall is made permeable to permit the imposition of an inlet profile that observes Berman's similarity equation [33].

Perhaps the first numerical study of hydrodynamic instability in an SRM model was carried out by Varapaev and Yagodkin [34]. Their analysis was purely numerical and

comparison with experimental data was not presented. An extended investigation that included laboratory measurements and full solutions of the Navier-Stokes equations was performed by Casalis and co-workers [24-29]; this helped to explain the effects of radial disturbances and the inconsistencies between the two available techniques, namely, those that relied on perturbing either the primitive variables or the streamfunction [35,36]. In similar context, the purpose of this work is to explore the hydrodynamic instability of the idealized solid and hybrid rockets. This will be accomplished by employing as our baseline the core flow of the cylindrical rocket with headwall injection presented recently by Majdalani and Vyas [37]. Therein, two flowfield solutions were proposed and these will be treated using spatial instability theory. The emphasis will be largely placed on the rotational model because of the minimal value gained from the irrotational solution.

The corresponding flowfield is often referred to as the extended Culick's [31] (or Taylor's [30]) and happens to be an important special case of the rotational hybrid model for which the headwall injection velocity is set to zero. After gaining confidence in the proposed methodology, results for the solid and hybrid models are presented and discussed.

The overall approach is based on the Local Non-Parallel (LNP) technique that involves solving the dispersion equations derived from the three dimensional incompressible Navier-Stokes equations using normal mode decomposition that retains non-parallel disturbances (i.e., both radial and tangential components of pressure and velocity). This approach has been refined by Casalis, Avalon and Pineau [24] who have applied it in investigating the instability of injection-driven flow configurations simulating solid propellant rockets. Chedevergne, Casalis and Féraille [38] have further

improved their approach by incorporating the so-called biglobal technique. In general, these studies have experimented with and compared three general approaches:

- the OSE or Local Parallel approach based on solving the Orr-Sommerfeld Equation (OSE); here, the tangential and radial disturbances are discounted, thus leading to potentially inaccurate results [34];
- the Local Non-Parallel (LNP) approach in which tangential and radial disturbances are kept;
- the Parabolized Stability Equations (PSE) described by Herbert [39] and Bertolotti [40]; and
- the biglobal technique according to which the disturbance amplitudes are written as function of two spatial coordinates (e.g. radial and axial). As explained by Chedevergne, Casalis and Féraille [38], spatial amplification (or decay) is not restricted to an exponential form.

Due to the relative simplicity and accuracy of the LNP approach, it will be applied to investigate spatial instability characteristics of solid rocket motors (SRMs) and hybrid rocket engines (HREs), giving particular attention to changes in the tangential wave number, the injection Reynolds number, and the swirl parameter. When helpful, results will be compared to the stability characteristics of the Majdalani-Vyas flow model [37]. Being an extended version of the Taylor-Culick profile [31], this baseline solution has been extensively validated and used in modeling solid and, recently, hybrid rockets.

1.4. Connection with Vortex Shedding

The mechanisms of sound production from flow in ducts have been known for many years and are commonly used in musical instruments. Flandro and Jacobs [41] were

perhaps the first to report the acoustic mode excitation by vortex shedding in a rocket motor. Flandro [42] later proposed a linearized approach that is based on the hydrodynamic instability analysis to evaluate the vortex shedding risk in a solid rocket motor. During his analysis, he observed that if a sheared layer is produced at the centerbore/slot transition and if the velocity gradient is sufficiently large then the shear layer becomes unstable and a large periodic vortex structure will be generated. The first results were obtained by Flandro and Jacobs [41] on oscillations due to vortex shedding formed in a simple grain geometry. Important characteristics which were observed during the analysis were reducing frequencies and dependence of those frequencies upon the fluid flow or gas flow velocities. In particular, the existence of a critical Strouhal number was recognized. Of great significance was the finding that the vortex shedding mechanism itself is characterized by a broadband frequency response and, hence, can come into resonance with acoustic oscillation frequencies when these are below the critical limit Strouhal number.

Efforts were made over a period of many years to understand the mechanism behind these oscillations. Several solid propellant boosters used for space application were tested for stability using classical codes but these motors during the time of real firing produced high magnitudes of pressure and thrust oscillation on their longitudinal or axial modes that were not predicted by the standard stability algorithms. The frequencies produced were low in magnitude and representative of coupled vertical/acoustic instability modes.

During the development phases of large French Ariane 5 booster rocket, researchers were worried about vortex shedding driven oscillation. This research

incorporated both experimental and theoretical developments [24-29]. As an illustration, unsteady pressure measurements are displayed through a water fall plot in Fig. 1-1.

The solid lines represent the natural frequencies of specific motors whereas bumps represent the pressure fluctuations which are shed by structural vortices. The frequency of these vortices matches the natural frequency of the motor, and whenever the natural frequency changes due to dimensional change with time, i.e. regression of the burning wall, the vortices frequency shift with it. This behavior leaves no room for doubt that the natural frequency is indeed the controlling frequency. Based on this fact, the first acoustic frequency may be considered as the driving frequency in the forthcoming analysis of hydrodynamic instability waves.

The cause of the vortex shedding is still unclear, but the existence of the instability waves has been proven and compared to experimental measurements in many studies [24-29,43,44]. Moreover, Dunlap and coworkers [24-29,43,44] have observed that the frequency of hydrodynamic waves matches the frequency of the acoustic waves. Based on the above observations, one may assume that for smooth channels where there are no obstacles or intrusions, the parietal pressure oscillations are generated due to acoustic pressure fluctuations. In fact, these fluctuations in the hydrodynamic/acoustic waves are the result of self-looping oscillations which are in turn produced by the receptivity process described quite elegantly by Griffond [45].

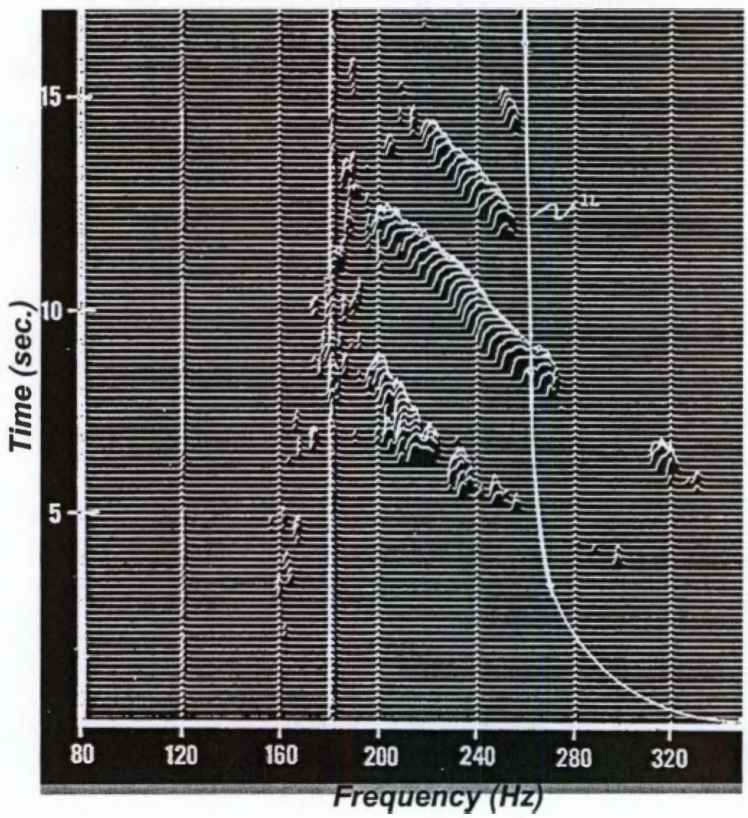

Figure 1-1. Displays the vortex shedding behavior and its relation to the fundamental frequency of the Minuteman III, Third Stage rocket motor (Flandro, Ref [42]).

2. Analysis of Idealized Solid and Hybrid Rockets

This investigation follows suit by applying the LNP approach to a similar geometric setting that is germane to the conventional hybrid grain shape and that of a solid propellant motor with reactive headend. Here the headwall is made permeable to permit the imposition of an inlet profile that observes Berman's similarity equation [33].

The purpose of this work is to explore the hydrodynamic instability of the idealized solid and hybrid rockets. This will be accomplished by employing as our baseline the core flow of the cylindrical rocket with headwall injection presented recently by Majdalani and Vyas [37]. The emphasis will be largely placed on the rotational model because of the minimal value gained from the irrotational solution.

In this section we will introduce the mean flowfield and its corresponding geometry. The corresponding flowfield is often referred to as Culick's [31] (or Taylor's [30]) and happens to be an important special case of the rotational hybrid model for which the headwall injection velocity is set to zero.

2.1. Geometry and Mean Flow Equations

The rotational hybrid core flow model is shown in Fig. 2-1. The motor is represented as a cylindrical chamber of length L and radius R. The headwall injection velocity is assumed to be Berman's cosine function with a maximum centerline velocity equal to U_0. This velocity can be adjusted to reproduce the rate of mass addition at the injector faceplate of a hybrid rocket. On the other hand, the independent sidewall

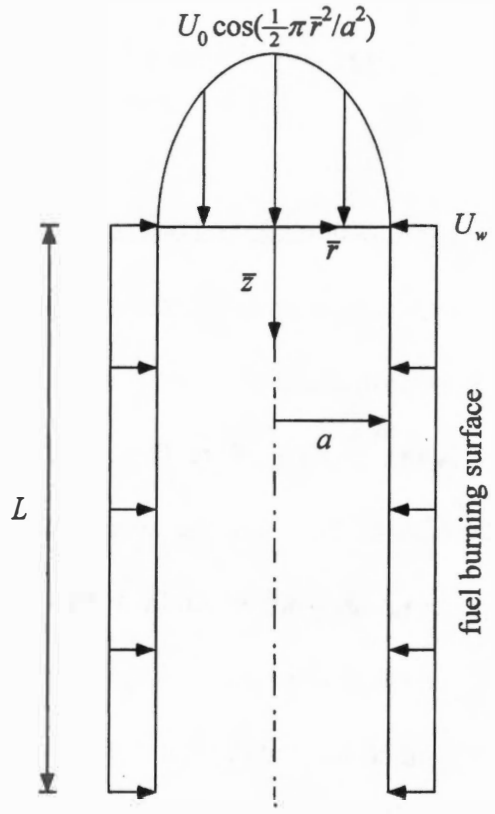

Figure 2-1. We sketch the rotational full-length rocket model permitting mass addition along both sidewall and headwall boundaries.

injection U_w is used to capture the regression rate of the solid fuel. As indicated in the Nomenclature, all coordinates are normalized by the chamber radius and velocities are normalized by U_w. In particular, the headwall injection constant is defined as $U_0/(\pi U_w)$. One should notice that $z=0$ stands for the upstream edge of the porous wall. The corresponding mean flow components are given by [37]

$$\begin{cases} U_r = -\sin(\frac{1}{2}\pi r^2)/r \\ U_z = \pi(z+u_h)\cos(\frac{1}{2}\pi r^2) \\ U_\theta = 0 \end{cases} \tag{2.1}$$

Before beginning the analysis, it may be useful to recall that the headwall injection constant germane to hybrid rockets falls in the range of $50 \le u_h \le 500$ [37]. At present, we start with $u_h = 0$ for the purpose of providing a benchmark that can be compared to existing solutions developed for SRMs with impervious headwalls [25]. Another rotational case that is worth considering is $u_h = \frac{1}{2}$; this ratio ensures that the headwall rate of mass addition is equal to $\rho\pi R^2 U_w$, hence consistent with that of a sufficiently long solid propellant grain burning equally uniformly along its headwall and sidewall.

2.2. Governing Equations

In this problem, three-dimensional incompressible flow is treated using cylindrical coordinates; the normalized Navier-Stokes and the continuity equations are written as:

continuity equation

$$\frac{\partial \tilde{U}_r}{\partial r} + \frac{\tilde{U}_r}{r} + \frac{1}{r}\frac{\partial \tilde{U}_\theta}{\partial \theta} + \frac{\partial \tilde{U}_z}{\partial z} = 0 \tag{2.2}$$

r-momentum equation

$$\frac{\partial \tilde{U}_r}{\partial t}+\tilde{U}_r\frac{\partial \tilde{U}_r}{\partial r}+\frac{\tilde{U}_\theta}{r}\frac{\partial \tilde{U}_r}{\partial \theta}-\frac{\tilde{U}_\theta^2}{r}+\tilde{U}_z\frac{\partial \tilde{U}_r}{\partial z}+\frac{\partial \tilde{P}}{\partial r}$$

$$=\frac{1}{Re}\left[\frac{\partial^2 \tilde{U}_r}{\partial r^2}+\frac{1}{r}\frac{\partial \tilde{U}_r}{\partial r}-\frac{\tilde{U}_r}{r^2}+\frac{1}{r^2}\frac{\partial^2 \tilde{U}_r}{\partial \theta^2}-\frac{2}{r^2}\frac{\partial \tilde{U}_\theta}{\partial \theta}+\frac{\partial^2 \tilde{U}_r}{\partial z^2}\right] \tag{2.3}$$

θ-momentum equation

$$\frac{\partial \tilde{U}_\theta}{\partial t}+\tilde{U}_r\frac{\partial \tilde{U}_\theta}{\partial r}+\frac{\tilde{U}_\theta}{r}\frac{\partial \tilde{U}_\theta}{\partial \theta}+\frac{\tilde{U}_r\tilde{U}_\theta}{r}+\tilde{U}_z\frac{\partial \tilde{U}_\theta}{\partial z}+\frac{1}{r}\frac{\partial \tilde{P}}{\partial \theta}$$

$$=\frac{1}{Re}\left[\frac{\partial^2 \tilde{U}_\theta}{\partial r^2}+\frac{1}{r}\frac{\partial \tilde{U}_\theta}{\partial r}-\frac{\tilde{U}_\theta}{r^2}+\frac{1}{r^2}\frac{\partial^2 \tilde{U}_\theta}{\partial \theta^2}+\frac{2}{r^2}\frac{\partial \tilde{U}_r}{\partial \theta}+\frac{\partial^2 \tilde{U}_\theta}{\partial z^2}\right] \tag{2.4}$$

z-momentum equation

$$\frac{\partial \tilde{U}_z}{\partial t}+\tilde{U}_r\frac{\partial \tilde{U}_z}{\partial r}+\frac{\tilde{U}_\theta}{r}\frac{\partial \tilde{U}_z}{\partial \theta}+\tilde{U}_z\frac{\partial \tilde{U}_z}{\partial z}+\frac{\partial \tilde{P}}{\partial z}=$$

$$\frac{1}{Re}\left[\frac{\partial^2 \tilde{U}_z}{\partial r^2}+\frac{1}{r}\frac{\partial \tilde{U}_z}{\partial r}+\frac{1}{r^2}\frac{\partial^2 \tilde{U}_z}{\partial \theta^2}+\frac{\partial^2 \tilde{U}_z}{\partial z^2}\right] \tag{2.5}$$

where r,θ,z are dimensionless coordinates.

In what follows, the equations will be subjected to small amplitude disturbances. The evolution of these disturbances is to be examined using linear instability theory.

3. Linear Instability Theory

It must be emphasized that the mean flow described by Eq. (2.1) is one possible solution. Its uniqueness is not demonstrated and its existence is not sufficient to ensure that the solution will be observed in practice. Our analysis investigates its stability. As with most dynamical systems, the mean flow which is continuously excited by the injection process may exhibit two types of responses with respect to this forcing. First, there is the so-called forced response, whose amplitude is of the same order as that of the forcing amplitude. Second, an eigenresponse may be rendered, the amplitude of which can grow significantly larger than the forcing amplitude. The amplitude of the eigenresponse may become unbounded. Such behavior is commensurate with micro events, such as small non-homogeneities in injection, generating a macro phenomenon that translates into appreciable growth in amplitude. The latter is characteristic of intrinsic instabilities. Obviously, determining the physical characteristics of the eigenresponse (including the attendant amplification rate, frequency, spatial dependency, etc.) is essential and constitutes the main goal of this study.

In analyzing stability, the instantaneous flow may be assumed to be a juxtaposition of the basic flow and the fluctuation whose growth must be determined. This is mathematically achieved by writing

$$\tilde{M} = M + \breve{m} \tag{3.1}$$

Here $\tilde{M}$ represents the instantaneous flow, M can be any component of the flowfield (e.g., velocity or pressure), and $\breve{m}$ is a physical quantity that represents possible fluctuations. All fluctuating quantities can be written as:

$$\breve{m} = m(r)\exp\left[i(q\theta + \sigma z - \omega t)\right] \tag{3.2}$$

where the function $m(r)$ is complex and represents the fluctuating amplitudes (u_r, u_θ, u_z, p), q is real and represents the tangential (i.e., azimuthal) wave number; σ and ω are complex quantities (dimensionless) which are suitably subdivided into real and imaginary parts:

$$\sigma = \sigma_r + i\sigma_i, \quad \omega = \omega_r + i\omega_i \tag{3.3}$$

Note that σ_r represents the longitudinal wave number and ω_r is the dimensionless circular frequency. The dimensional frequency is given by $f = \omega_r U_w/(2\pi R)$. The amplification of the amplitude with respect to time and distance z can be assessed from ω_i and $-\sigma_i$, respectively. According to the temporal theory for which $\sigma_i = 0$, fluctuations can only grow in time, and the growth is prescribed by the temporal rate ω_i. Conversely, spatial theory for which $\omega_i = 0$ permits fluctuations to grow only in z, and their local amplification is dependent on the spatial growth rate $-\sigma_i$.

3.1. Stability Equations

The Linearized Navier Stokes (LNS) equations can be obtained by substituting the instantaneous variables from Eq. (3.1) into Eqs. (2.2)–(2.5). One could then subtract the basic flow component from the resulting equations and follow by applying the normal mode decomposition of Eq. (3.2). The outcome is a set of LNS equations of the form:

$$\frac{\mathrm{d}u_r}{\mathrm{d}r} + \frac{u_r}{r} + iq\frac{u_\theta}{r} + i\sigma u_z = 0 \tag{3.4}$$

r-momentum equation

$$-i\omega u_r + U_r \frac{\mathrm{d}u_r}{\mathrm{d}r} + u_r \frac{\mathrm{d}U_r}{\mathrm{d}r} + iq\frac{U_\theta}{r}u_r - \frac{2U_\theta u_\theta}{r} + i\sigma U_z u_r + \frac{\mathrm{d}p}{\mathrm{d}r}$$

$$= \frac{1}{Re}\left[\frac{\mathrm{d}^2 u_r}{\mathrm{d}r^2} + \frac{1}{r}\frac{\mathrm{d}u_r}{\mathrm{d}r} - \frac{u_r}{r^2} - \frac{q^2}{r^2}u_r - \frac{2}{r^2}iqu_\theta - \sigma^2 u_r\right] \tag{3.5}$$

θ-momentum equation

$$-i\omega u_\theta + iqu_\theta U_r + u_r \frac{\mathrm{d}U_\theta}{\mathrm{d}r} + U_r \frac{\mathrm{d}u_\theta}{\mathrm{d}r} + iq\frac{U_\theta}{r}u_\theta + \frac{U_r u_\theta + U_\theta u_r}{r} + i\sigma U_z u_\theta + \frac{iq}{r}p$$

$$= \frac{1}{Re}\left[\frac{\mathrm{d}^2 u_\theta}{\mathrm{d}r^2} + \frac{1}{r}\frac{\mathrm{d}u_\theta}{\mathrm{d}r} - \frac{u_\theta}{r^2} - \frac{q^2}{r^2}u_\theta + \frac{2}{r^2}iqu_r - \sigma^2 u_\theta\right] \tag{3.6}$$

z-momentum equation

$$-i\omega u_z + U_r \frac{\mathrm{d}u_z}{\mathrm{d}r} + u_r \frac{\mathrm{d}U_z}{\mathrm{d}r} + iq\frac{U_\theta}{r}u_z + i\sigma U_z u_z + \frac{\mathrm{d}U_z}{\mathrm{d}z}u_z + i\sigma p =$$

$$\frac{1}{Re}\left[\frac{\mathrm{d}^2 u_z}{\mathrm{d}r^2} + \frac{1}{r}\frac{\mathrm{d}u_z}{\mathrm{d}r} - \frac{q^2}{r^2}u_z - \sigma^2 u_z\right] \tag{3.7}$$

This system encapsulates the interactions between mean components of velocity and the unsteady disturbances $\boldsymbol{u}(r)$ and $p(r)$. The implicit assumption is that while the steady (U_r, U_z) prescribe the motion and growth of unsteady waves, they themselves remain indifferent to the oscillations that they engender. In a recent study by Venugopal [46], it was shown that fluctuations are highly sensitive to the mean flow distribution, particularly, along the axis. This emphasizes the need to use the most suitable mean flow model for a given application. It also justifies the quest for refined mean flow models of rocket chambers. Examples include those by Majdalani and Van Moorhem [15,47], Majdalani, Vyas and Flandro [48,49], Majdalani and Zhou [50], Majdalani and Vyas [37], Majdalani [51], and others. In what follows, a careful set of boundary conditions is presented and discussed.

3.2. Vital Boundary Conditions

Equations (3.4)–(3.7) are second order in u_r, u_θ and u_z; upon close examination, it may be determined that the total order is equal to six when $q \neq 0$ and reduces to four when $q = 0$ (due to the elimination of u_θ and u_θ' from the original set). Of the required boundary conditions, three may be inferred from the velocity adherence condition at the sidewall. As no slip is observed at leading order by the mean flow ingredient, the fluctuations must vanish at the sidewall to avoid local interference. This implies

$$u_r = u_\theta = u_z = 0 \text{ at } r = 1 \tag{3.8}$$

Three conditions are missing still. To compensate, we expand the principal variables and substitute them into the linearised Navier-Stokes system. Suppression of singular terms is then used to extract the three desired constraints. Thus, using a polynomial expansion for the fluctuations,

$$u_r = \sum_{n=0}^{\infty} v_n r^n, \quad u_\theta = \sum_{n=0}^{\infty} w_n r^n, \quad u_z = \sum_{n=0}^{\infty} u_n r^n, \quad p = \sum_{n=0}^{\infty} p_n r^n \tag{3.9}$$

and, similarly, for the steady field,

$$U_z = f(z)\sum_{n=0}^{\infty} A_n r^n, \quad U_r = \sum_{n=0}^{\infty} B_n r^n, \quad U_\theta = 0 \tag{3.10}$$

These expansions are substituted back into Eqs. (3.4)–(3.7) and segregated: one is left with three systems, with four equations in each. These are

System 1
$$\begin{cases} v_0 + iqw_0 = 0 \\ (1+q^2)v_0 + 2iqw_0 = 0 \\ 2iqv_0 - w_0(1+q^2) = 0 \\ -q^2 u_0 = 0 \end{cases} \tag{3.11}$$

System 2

$$\begin{cases} 2v_1 + iqw_1 = -i\sigma u_0 \\ -q^2 v_1 - 2iqw_1 = 0 \\ 2iqv_1 - q^2 w_1 = Re\left[iqp_0 + w_0 B_0\right] \\ u_1(1-q^2) = 0 \end{cases} \tag{3.12}$$

At this juncture, the radial momentum equation is transformed into a gigantic system of equations that can be resolved to any order of accuracy depending on the summation integer n. This set is given by

System 3 (r^n members, $n \geq 0$)

$$(n+3)v_{(n+2)} + iqw_{(n+2)} + i\sigma u_{(n+1)} = 0 \tag{3.13}$$

$$\left[(n+2)^2 - (1+q^2)\right]v_{(n+2)} - 2iqw_{(n+2)} - Re(n+1)p_{(n+1)}$$

$$= Re\left\{\left(\frac{\sigma^2}{Re} - i\omega\right)v_n + \sum_{j=0}^{n}\left[(i\sigma fA_j + (j+1)B_{(j+1)})v_{(n-j)} + (n-j+1)B_j v_{(n-j+1)}\right]\right\} \tag{3.14}$$

$$2iqv_{(n+2)} + ((n+2)^2 - (1+q^2))w_{(n+2)} - B_0 w_{(n+1)} - iqRep_{(n+1)}$$

$$= Re\left\{\left(\frac{\sigma^2}{Re} - i\omega\right)w_n + \sum_{j=0}^{n}\left[\left(B_{(j+1)} + i\sigma fA_j\right)w_{(n-j)} + (n-j+1)w_{(n-j+1)}\right]\right\} \tag{3.15}$$

$$\left[(n+2)^2 - q^2\right]u_{(n+2)} - (\sigma^2 - iRe\omega)u_n - i\sigma Rep_n$$

$$= Re\sum_{i=1}^{n}\left\{\left[(f' + i\sigma f)A_j\right]u_{(n+1)} + (n-j+1)u_{(n-j+1)}B_{(j)} + f(j+1)A_{(j+1)}v_{(n-j)}\right\} \tag{3.16}$$

System 1 can be readily expressed in terms of velocity fluctuations. Depending on the tangential wave number, one can put, along the centerline,

$$\begin{cases} q=0 \rightarrow u_r(0)=u_\theta(0)=\dfrac{\mathrm{d}u_z}{\mathrm{d}r}(0)=0 \\ q=1 \rightarrow \dfrac{\mathrm{d}u_r}{\mathrm{d}r}(0)=\dfrac{\mathrm{d}u_\theta}{\mathrm{d}r}(0)=u_z(0)=0 \\ q\geq 2 \rightarrow u_r(0)=u_\theta(0)=u_z(0)=0 \end{cases} \tag{3.17}$$

The three original boundary conditions due to no slip may now be supplemented by Eq. (3.17) to provide a complete set of auxiliary conditions for the velocity. To secure the pressure at $q=0$, one can substitute the findings in Eq. (3.17) back into the $r-$momentum expression in Eq. (3.5) (or, equivalently, by utilizing the first three equations of System 2). This enables us to deduce that $p'(0)=0$. However, for $q\geq 1$, the first three equations of System 2 can be solved to obtain, along the centerline, the trivial set corresponding to $v_1=w_1=0$ and $p_0\equiv p(0)=0$. We are thus compelled to apply a normalization condition for the pressure at the sidewall that does not affect the solution. Without loss in generality, we therefore set $p(1)=1$. By so doing, the pressure magnitude becomes a normalizing factor for all remaining amplitudes. These will be later rescaled by the initial disturbance amplitude A_0.

3.3. Shooting Procedure and Discretization

Equations (3.4)–(3.7) can be rearranged and manipulated into six first-order ODEs. Our approach follows precisely that of Malik [52]. Thus u_r' is taken from mass conservation and inserted into the *r*-momentum equation. The latter is reduced to a first-order ODE with two boundary conditions. The extra condition is used to secure convergence at the opposing boundary (here, we choose the sidewall as our shooting target). The six ODEs that must be solved form a linear set that can be expressed as

$$\frac{dZ}{dr} = [\mathbf{C}]\, Z, i = 1,2,\ldots,6;\ [\mathbf{Z}] = \left\{ u_r, u_\theta, \frac{du_\theta}{dr}, u_z, \frac{du_z}{dr}, p \right\}^T \tag{3.18}$$

The coefficient matrix [C] is detailed in Appendix A.

This system admits a non-trivial solution by virtue of the pressure condition being non-homogeneous. In order to expedite convergence, we find it instructive to discretize all terms in Z' using Chebyshev's spectral collocation method [53] (see Appendix A). At present, 150 collocation points are used in conjunction with Müller's root solving algorithm; these are found to be sufficient to ensure the desired tolerance set at 10^{-9} in σ. This is further explained in a paper that addresses the stability of the bidirectional vortex [54]. In marching forward, our dispersion relation linking all primitive variables and parameters takes the form of $f(\sigma, \omega, q, z, Re, u_h) = 0$. Thus, in order to make headway, we choose for each tangential wave number q a certain frequency $\omega \equiv \omega_r$ at a fixed set of operating parameters (Reynolds number and headwall injection constant u_h). We then iterate at every spatial position of interest z on the complex σ until the target velocity amplitude u_r is made to vanish at the sidewall. This yields the amplitude vector [Z] in addition to the spatial growth rate $-\sigma_i$, and the wave number σ_r. From σ_r, one may calculate the spatial wavelength, $\lambda = 2\pi / \sigma_r$ and the axial speed of propagation (or phase velocity), $\dot{x} = \omega / \sigma_r$. After determining our first two σ_r values, we linearly extrapolate for the subsequent initial guess. Throughout this simulation, we fix the Reynolds number at 5,000 and u_h for the application at hand. At this high level of sidewall injection, it is universally accepted that inviscid conditions will prevail to the

extent that our steady-state model becomes an accurate representation of the incompressible core flow. We therefore assume that the physical model satisfies the fundamental criteria for which compressibility may be ignored. These are extensively described in a paper by Majdalani [55].

The second parameter that is left invariant for a given simulation is the tangential wave number q. Thus, for each frequency ω, we march in space up to the point prescribed by $z = 20$. The axial extent is covered in equal spatial increments of 0.1. After completing each sweep, we then increase the frequency by a variable amount: at low ω, we use a fine step size of 1 to capture the critical frequency at the nose-tip of the iso-n curves; these are defined and illustrated in the next section. The step size is then increased to 5 and 10 as we approach straight line behavior in the iso-n curves. The maximum frequency we explore depends on the headwall injection constant. For $u_h = 0.5$, our maximum frequency reaches 175 whereas for $u_h = 50$ we find it necessary to raise the bar to 800. The highest ω that we investigate is the one that enables us to capture the most amplified value of n at $z = 15$. This typically coincides with the iso-n curve reaching an amplification factor of $n = 11$. Based on existing experimental data with no headwall injection, transition to turbulence takes place between $n = 7$ and 9 according to stability theory [25] and experiments [56]. For $u_h = 0.5$, a similar behavior is expected. It can thus be argued that any evolution beyond $n = 9$ may no longer observe linear instability theory or help to delimit the unstable domain. More experimental work with headwall injection is therefore required to substantiate further refinement to this analysis.

In what follows, the energy associated with the hydrodynamic instability waves will be evaluated. It will then be carefully incorporated in the present framework used to asses the propensity of combustion instability.

4. Effects on Net CI System Amplitude

4.1. Motivation

Experiments have pointed out the existence of a new source of instability that was not incorporated in the existing acoustic stability theory. Several investigators have identified this deficiency including Lupoglazoff, Vuillot, Casalis, Dupays, Griffond, and many others [56-63]. As proposed by Vuillot [64,65], three kinds of vortex shedding can be identified. First, VSA (Angle Vortex Shedding), which may take place in the upper downstream angle of a block of a propellant. At this point the wall injection is not uniform and hence shear layer instability may be induced. The second type is the VSO (Obstacle Vortex Shedding) which relates to the presence of inhibitors between two blocks of propellant in segmented SRM design. This source was believed to be the main or the only source of vortex shedding instability and hence thrust oscillation. The third source which does not come from irregularities in the geometry is called VSP (Parietal Vortex Shedding). The latter source is believed to be caused by the instability of the flowfield itself. Our focus in this study will be mainly on the third kind of instability. The major problem of VSP is that it cannot be measured directly in experiments with combustion, but it can be identified in different computations [65] and in cold gas flow experiments. The idea here is to account for the parietal vortex shedding effect on the total wave amplitude as defined in the combustion instability (CI) framework. To achieve this goal, we will support our study by physical interpretation and experimental confirmation whenever possible.

4.2. Analysis

As indicated before, the hydrodynamic waves cannot be measured directly in experimental measurements with combustion. Consequently, we are compelled to account for these wave effects in a different way that makes it amenable for experimental measurements. To proceed, physical interpretation as well as experimental measurements will be used. Before going further, it is necessary to clarify the differences between the hydrodynamic waves and the acoustic waves. Without loss in generality, the fact that the acoustic waves have long wavelengths, they introduce short time scales, whereas the hydrodynamic waves introduce long time scales because of their short wavelengths. Another important fact is that the acoustic waves propagate at the speed of sound, whereas the hydrodynamic waves propagate over a fraction of the acoustic speed. These ideas are very well explained by Flandro [42] and Griffond [45]. The presence of short and long timescales enables us to superimpose the hydrodynamic solution on the acoustic solution and proceed in the analysis. The next step in the analysis is to use the full energy equation that has been proposed by Flandro, Majdalani and Sims [66,67]. However, while the latter investigations have focused on the nonlinear theory, we limit ourselves to the linear part. In either combustion or hydrodynamic instability, the linear theory can only describe the tendency of the waves to grow or decay. So, by combining both waves, there is a possibility to understand the effect of the hydrodynamic waves on the net wave amplitude ε. Also, information of the effect of the injection Mach number, and the initial amplitude of the hydrodynamic waves will be investigated.

Following the nonlinear analysis by Flandro, Majdalani and Sims [66,67], we utilize the following standard notation with stars (*) denoting dimensional quantities,

subscript 0 symbolizing quiescent initial chamber reference conditions, and L being the characteristic length. The variables then can be written as:

$$\begin{cases} p = p^*/p_0 \\ \rho = \rho^*/\rho_0 \\ T = T^*/T_0 \\ \boldsymbol{V} = \boldsymbol{V}^*/a_0 \\ \boldsymbol{r} = \boldsymbol{r}^*/L \end{cases} \qquad \begin{cases} \boldsymbol{F} = \boldsymbol{F}^*/\left(\rho_0 a_0^2/L\right) \\ t = t^*/\left(L/a_0\right) \\ \omega = \omega^*/\left(a_0/L\right) \\ e = e^*/a_0^2 \end{cases} \tag{4.1}$$

$\boldsymbol{F}$ represents the body force and e is the specific internal energy.

4.2.1. Governing Equations

In the aforementioned analysis, the governing equations are written in a form best suited for combustion instability analysis. In this formulation the full conservation of energy equation, rarely seen in textbooks, is employed in order to obtain variations in mean chamber properties. The primitive variable forms are used to clarify the effect of the vorticity. Here the same set of equations is resorted to. The governing equations are written in dimensionless form:

Continuity equation

$$\frac{\partial \rho}{\partial t} + \nabla \cdot \left(\rho \boldsymbol{V}\right) = 0 \tag{4.2}$$

Momentum balance

$$\rho\left(\frac{\partial \boldsymbol{V}}{\partial t} + \tfrac{1}{2}\nabla \boldsymbol{V} \cdot \boldsymbol{V} - \boldsymbol{V} \times \boldsymbol{\omega}\right) = -\frac{1}{\gamma}\nabla p - \delta^2 \nabla \times \left(\nabla \times \boldsymbol{V}\right) + \delta_d^2 \nabla\left(\nabla \cdot \boldsymbol{V}\right) \tag{4.3}$$

Energy balance

$$\frac{\partial}{\partial t}\left[\rho\left(e+\tfrac{1}{2}\boldsymbol{V}\cdot\boldsymbol{V}\right)\right]+\nabla\cdot\left[\rho\boldsymbol{V}\left(e+\tfrac{1}{2}\boldsymbol{V}\cdot\boldsymbol{V}\right)\right]=\left\{\begin{array}{l}\dfrac{\delta^2}{(\gamma-1)Pr}\nabla^2T-\dfrac{1}{\gamma}\nabla\cdot(p\boldsymbol{V})\\+p\boldsymbol{V}\cdot(\boldsymbol{V}\times\boldsymbol{\omega})\\+\delta^2\left[\boldsymbol{\omega}\cdot\boldsymbol{\omega}-\boldsymbol{V}\cdot(\nabla\times\boldsymbol{\omega})\right]\\+\delta_d^2\left[(\nabla\cdot\boldsymbol{V})^2+\boldsymbol{V}\cdot\nabla(\nabla\cdot\boldsymbol{V})\right]\end{array}\right\} \tag{4.4}$$

Equation of state

$$p=\rho T \tag{4.5}$$

In Eq. (4.4) we choose not to include the body force and the effect from combustion. The constant terms in Eq. (4.4) are defined as

$$\delta^2=\frac{\nu}{a_0L},\ \delta_d^2=\delta^2\left(\frac{\eta}{\mu}+\frac{4}{3}\right),\text{and } Pr=\frac{C_p\mu}{\kappa} \tag{4.6}$$

The Prandtl number has a value of unity in most cases since the heat transfer and viscous effects may be assumed to be of the same order. After the mechanical energy terms are removed by subtracting the momentum equation (multiplied by the velocity vector) from Eq. (4.4) the thermodynamic energy is then expressed in dimensionless form as follows:

$$\rho\left(\frac{\partial T}{\partial t}+\boldsymbol{V}\cdot\nabla T\right)=\frac{(\gamma-1)}{\gamma}\left(\frac{\partial p}{\partial t}+\boldsymbol{V}\cdot\nabla p\right)+(\gamma-1)\left\{\begin{array}{l}\dfrac{\delta^2}{(\gamma-1)Pr}\nabla^2T\\+\delta^2\boldsymbol{\omega}\cdot\boldsymbol{\omega}+\delta_d^2(\nabla\cdot\boldsymbol{V})^2\end{array}\right\} \tag{4.7}$$

4.2.2. Decomposition of the Variables

All variables can be separated into steady and unsteady components and they can be written as follows:

$$\begin{cases} \rho = \bar{\rho} + \rho^{(1)} \\ p = \bar{P} + p^{(1)} \\ T = \bar{T} + T^{(1)} \\ \boldsymbol{V} = \bar{M}_b \boldsymbol{U} + \boldsymbol{u}^{(1)} \\ \boldsymbol{\omega} = \bar{M}_b \nabla \times \boldsymbol{U} + \nabla \times \boldsymbol{u}^{(1)} = \bar{M}_b \boldsymbol{\Omega} + \boldsymbol{\omega}^{(1)} \end{cases} \tag{4.8}$$

As usual, the overbar quantities represent the steady parts which slowly change in time, and the superscript (1) the unsteady flowfield. The latter is assumed to be known to the first order in the amplitude of the wave. The unsteady solution for the internal burning cylinder is fully described by Majdalani and Flandro [16]. From a combustion instability perspective, its corresponding rotational flowfield and boundary layer structure are presented in [68,69]. In many analyses, one can define a small parameter ε that represents the size of the oscillatory components relative to the steady parts in an implied perturbation expansion of the equations of motion. As an example, pressure in Eq. (4.8) may be expressed as

$$p = \bar{P} + \varepsilon p' + O(\varepsilon^2) \tag{4.9}$$

Here, ε represents the amplitude of the oscillatory variable relative to the mean pressure; in effect it is the ratio of the oscillatory amplitude to the mean value. For linear behavior, the unsteady gas motion can be characterized by a set of uncoupled acoustic modes. As a result, the parameter ε has a fixed numerical value and can be used to describe the amplitude of any mode of oscillation at any instant of time. The acoustic velocity fluctuation, however, is related to the pressure fluctuation by $\hat{\boldsymbol{u}}_m = -\nabla p_m / (\gamma k_m)$. The relative modes of amplitude can be simplified by writing

$$p' = \varepsilon\left[A_1(t)\psi_1(\boldsymbol{r}) + A_2(t)\psi_2(\boldsymbol{r}) + A_3(t)\psi_3(\boldsymbol{r}) + \cdots\right] = \varepsilon\sum_{m=1}^{N} A_m(t)\psi_m(\boldsymbol{r}) \quad (4.10)$$

Here A_m is a complex oscillatory function of time, and ψ_m are the mode shapes. For longitudinal oscillations in a cylindrical chamber, A_m is a sinusoidal function of time corresponding to the wave number m of a particular mode. This simplification removes the need to solve large and complex sets of coupled partial differential equations. Now, the system of equations (4.8) can be written as

$$\begin{cases} \rho = \bar{\rho} + \varepsilon\rho' \\ p = \bar{P} + \varepsilon\left(\hat{p} + \tilde{p} + \breve{p}\right) \\ T = \bar{T} + T^{(1)} \\ \boldsymbol{V} = \bar{M}_b\boldsymbol{U} + \varepsilon\left(\hat{\boldsymbol{u}} + \tilde{\boldsymbol{u}} + \breve{\boldsymbol{u}}\right) \\ \boldsymbol{\omega} = \bar{M}_b\nabla\times\boldsymbol{U} + \nabla\times\boldsymbol{u}^{(1)} = \bar{M}_b\boldsymbol{\Omega} + \left(\tilde{\boldsymbol{\omega}} + \breve{\boldsymbol{\omega}}\right) \end{cases} \quad (4.11)$$

Here, the *caret* ^ denotes irrotational compressible disturbances and the incompressible rotational waves are represented by the *tilde* ~. Finally the hydrodynamic effect here is denoted by a breve (an inverted arc). The superposition of hydrodynamic waves as shown in Eq. (4.11) does not only affect spatial fluctuations of the wave, but it also affects the growth or the decay rate of the net system amplitude ε. Equation (4.11) will be used to derive an expression of the growth or decay rate of the net system amplitude caused by the hydrodynamic instability waves.

4.2.3. Evolution of the System Amplitude

In an attempt to evaluate the hydrodynamic effect, we will use the energy approach described in [66,67]. The only difference is the new component representing the hydrodynamic effect, which will be added. According to this methodology, time evolution of the system amplitude is derived from the energy equation (4.4). Therein, the

analysis encompasses both linear and nonlinear evolutions. In our case, the only available solution in hydrodynamic instability is the linear one. For that, we limit our derivation to the linear behavior.

Pursuant to this approach, the energy density per unit volume can be written as:

$$\mathscr{E}^* = \tfrac{1}{2}\rho^*\left(e^* + \boldsymbol{V}^* \cdot \boldsymbol{V}^*\right) \tag{4.12}$$

So, by normalizing, one gets

$$\mathscr{E} = \frac{\mathscr{E}^*}{\rho_0 a_0^2} = \frac{1}{2}\frac{\rho^*}{\rho_0}\left(\frac{e^*}{a_0^2} + \frac{\boldsymbol{V}^* \cdot \boldsymbol{V}^*}{a_0^2}\right) = \frac{1}{2}\rho\left(e + \boldsymbol{V} \cdot \boldsymbol{V}\right) \tag{4.13}$$

where the internal energy e is normalized by $a_0{}^2$. Since it is justifiable to assume a calorically perfect gas, the internal energy can be written in terms of the temperature using

$$e^* = C_v T^* = \frac{R_0}{\gamma - 1} T^* \tag{4.14}$$

where R_0 is the universal gas constant. Subsequently, one can put

$$e = \frac{e^*}{a_0^2} = \frac{R_0}{(\gamma-1)}\frac{T^*}{a_0^2} = \frac{R_0}{(\gamma-1)}\frac{T^*}{(\gamma R_0 T_0)} = \frac{T}{\gamma(\gamma-1)} \tag{4.15}$$

Thus, Eq. (4.4) can be written as

$$\frac{\partial \mathscr{E}}{\partial t} = -\nabla \cdot \left[\rho \boldsymbol{V}\left(\frac{T}{\gamma(\gamma-1)} + \tfrac{1}{2}\boldsymbol{V} \cdot \boldsymbol{V}\right)\right] + \left\{\begin{array}{l} -\dfrac{1}{\gamma}\nabla \cdot (p\boldsymbol{V}) + \rho \boldsymbol{V} \cdot (\boldsymbol{V} \times \boldsymbol{\omega}) \\ +\delta^2\left[\boldsymbol{\omega} \cdot \boldsymbol{\omega} - \boldsymbol{V} \cdot (\nabla \times \boldsymbol{\omega})\right] + \dfrac{\delta^2}{(\gamma-1)Pr}\nabla^2 T \\ +\delta_d^2\left[(\nabla \cdot \boldsymbol{V})^2 + \boldsymbol{V} \cdot \nabla(\nabla \cdot \boldsymbol{V})\right] + \dot{Q} + \boldsymbol{V} \cdot \boldsymbol{F} \end{array}\right\} \tag{4.16}$$

where $\mathscr{E}$ is the dimensionless total energy density. It can be written as

$$\mathscr{E} = \bar{\mathscr{E}} + \mathscr{E}' = \frac{\rho T}{\gamma(\gamma-1)} + \frac{1}{2}\rho \boldsymbol{V}\cdot\boldsymbol{V} \tag{4.17}$$

The detailed analysis of the derivation of the linear growth rate can be found in Appendix B. The final result of the linear growth rate derivation is given by

$$\alpha^{(1)} = \frac{1}{2E^2}\left\{\begin{aligned}
&-\frac{1}{\gamma}\iint_S \boldsymbol{n}\cdot\langle p'\boldsymbol{u}'\rangle \mathrm{d}S - \frac{M_b}{\gamma^3\bar{P}}\iint_S \boldsymbol{n}\cdot\boldsymbol{U}\left\langle (p')^2\right\rangle \mathrm{d}S \\
&-M_b\bar{P}\iint_S \boldsymbol{n}\cdot\left\langle \frac{1}{2}\boldsymbol{U}(\boldsymbol{u}'\cdot\boldsymbol{u}') + \boldsymbol{u}'(\boldsymbol{U}\cdot\boldsymbol{u}')\right\rangle \mathrm{d}S \\
&\underbrace{+M_b\bar{P}\iiint_V \boldsymbol{U}\cdot\langle \boldsymbol{u}'\times\boldsymbol{\omega}'\rangle \mathrm{d}V + M_b\bar{P}\iiint_V \langle \boldsymbol{u}'\cdot(\boldsymbol{U}\times\boldsymbol{\omega}'\rangle \mathrm{d}V}_{\text{vanishes via vector identity}} \\
&+\delta^2\iint_S \boldsymbol{n}\cdot\langle \boldsymbol{u}'\times\boldsymbol{\omega}'\rangle \mathrm{d}S + \delta_d^2\iiint_V \langle \boldsymbol{u}'\cdot\nabla(\nabla\cdot\boldsymbol{u}')\rangle \mathrm{d}V \\
&\underbrace{+M_b\bar{P}\iiint_V \langle \boldsymbol{u}'\cdot\boldsymbol{u}'\times\boldsymbol{\Omega}\rangle \mathrm{d}V}_{0}
\end{aligned}\right. \tag{4.18}$$

Using vector calculus, the fourth and fifth terms cancel each other and the last term goes to zero. This leads to

$$\alpha^{(1)} = \frac{1}{2E^2}\left\{\begin{aligned}
&-\frac{1}{\gamma}\iint_S \boldsymbol{n}\cdot\langle p'\boldsymbol{u}'\rangle \mathrm{d}S - \frac{M_b}{\gamma^3\bar{P}}\iint_S \boldsymbol{n}\cdot\boldsymbol{U}\left\langle (p')^2\right\rangle \mathrm{d}S \\
&-M_b\bar{P}\iint_S \boldsymbol{n}\cdot\left\langle \frac{1}{2}\boldsymbol{U}(\boldsymbol{u}'\cdot\boldsymbol{u}') + \boldsymbol{u}'(\boldsymbol{U}\cdot\boldsymbol{u}')\right\rangle \mathrm{d}S \\
&+\delta^2\iint_S \boldsymbol{n}\cdot\langle \boldsymbol{u}'\times\boldsymbol{\omega}'\rangle \mathrm{d}S + \delta_d^2\iiint_V \langle \boldsymbol{u}'\cdot\nabla(\nabla\cdot\boldsymbol{u}')\rangle \mathrm{d}V
\end{aligned}\right. \tag{4.19}$$

The primes here represent fluctuating quantities as per Eq. (4.11). To study the effect of the parietal vortex shedding on the net system amplitude, the parietal pressure, velocity and vorticity will be added to the acoustic one and put back in Eq. (4.19). Therefore, one can represent the fluctuating quantities as

$$\begin{cases} \boldsymbol{u}' = \hat{\boldsymbol{u}} + \tilde{\boldsymbol{u}} + \breve{\boldsymbol{u}} \\ p' = \hat{p} + \tilde{p} + \breve{p} \\ \boldsymbol{\omega}' = \tilde{\boldsymbol{\omega}} + \breve{\boldsymbol{\omega}} \end{cases} \tag{4.20}$$

where the breve represents the new hydrodynamic wave component.

One should point out that each wave has different specifications. For example, The $\hat{\boldsymbol{u}}$ represents compressible irrotational acoustic velocity; on the other hand $\tilde{\boldsymbol{u}}$ is the incompressible rotational acoustic velocity; and finally $\breve{\boldsymbol{u}}$ represents the incompressible rotational hydrodynamic wave. These disturbances exhibit the following properties:

$$\nabla \times \hat{\boldsymbol{u}} = 0, \quad \nabla \cdot \tilde{\boldsymbol{u}} = \nabla \cdot \breve{\boldsymbol{u}} = 0, \quad \nabla \times \tilde{\boldsymbol{u}} = \boldsymbol{\omega}_{vac}, \quad \nabla \times \breve{\boldsymbol{u}} = \boldsymbol{\omega}_{p} \tag{4.21}$$

To satisfy no slip, the first two acoustic components ($\hat{\boldsymbol{u}}, \tilde{\boldsymbol{u}}$) cancel each other on the surface; similarly, the hydrodynamic disturbance ($\breve{\boldsymbol{u}}$) must vanish on the surface. The physical reason for setting hydrodynamic waves to zero independently on the surface is due to the fact that these waves propagate at a fraction of the flowfield velocity (see Flandro [42] and Girffond [45]), in contrast, the acoustic waves propagate at the speed of sound. Moreover, hydrodynamic waves have shorter wavelengths compared to the acoustic waves [45]. Accordingly, one can write the boundary conditions on the surface as follows

$$\forall (t,z): \ (\hat{\boldsymbol{u}}_z + \tilde{\boldsymbol{u}}_z)\big|_{r=1} = 0, \quad \breve{\boldsymbol{u}}\big|_{r=1} = 0 \tag{4.22}$$

Substituting Eq. (4.20) into Eq. (4.19) and taking into account Eq. (4.21) will result in the total unsteady growth rate. As we discussed previously, our main concern is the effect of the hydrodynamic instability on the net wave amplitude. For that, we will separate $\alpha^{(1)}$ into two terms. The first term $\alpha^{(1)}_{vac}$ represents the vortical- acoustic growth

rate with no hydrodynamic contribution. The second term accounts for the effect of hydrodynamic waves $\alpha_{hyd}^{(1)}$. Consequently, we write

$$\alpha^{(1)} = \alpha_{vac}^{(1)} + \alpha_{hyd}^{(1)} \tag{4.23}$$

Results can be obtained from

$$\alpha_{vac}^{(1)} \simeq \frac{1}{2E^2}\begin{cases} -\dfrac{1}{\gamma}\displaystyle\iint_S \boldsymbol{n}\cdot\langle p'\boldsymbol{u}'\rangle \mathrm{d}S - \frac{M_b}{\gamma^3\overline{P}}\iint_S \boldsymbol{n}\cdot\boldsymbol{U}\left\langle (p')^2\right\rangle \mathrm{d}S \\ -M_b\overline{P}\displaystyle\iint_S \boldsymbol{n}\cdot\left\langle \frac{1}{2}\boldsymbol{U}(\boldsymbol{u}'\cdot\boldsymbol{u}') + \boldsymbol{u}'(\boldsymbol{U}\cdot\boldsymbol{u}')\right\rangle \mathrm{d}S \\ +\delta^2\displaystyle\iint_S \boldsymbol{n}\cdot\langle \boldsymbol{u}'\times\boldsymbol{\omega}'\rangle \mathrm{d}S + \delta_d^2\iiint_V \langle \boldsymbol{u}'\cdot\nabla(\nabla\cdot\boldsymbol{u}')\rangle \mathrm{d}V \end{cases} \tag{4.24}$$

where

$$\begin{cases} \boldsymbol{u}' = \hat{\boldsymbol{u}} + \tilde{\boldsymbol{u}} \\ p' = \hat{p} + \tilde{p} \text{ (vortical-acoustic representation)} \\ \boldsymbol{\omega}' = \tilde{\boldsymbol{\omega}} \end{cases} \tag{4.25}$$

or

$$\alpha_{vac}^{(1)} + \alpha_{hyd}^{(1)} \simeq \frac{1}{2E^2}\begin{cases} -\dfrac{1}{\gamma}\displaystyle\iint_S \boldsymbol{n}\cdot\langle p'\boldsymbol{u}'\rangle \mathrm{d}S - \frac{M_b}{\gamma^3\overline{P}}\iint_S \boldsymbol{n}\cdot\boldsymbol{U}\left\langle (p')^2\right\rangle \mathrm{d}S \\ -M_b\overline{P}\displaystyle\iint_S \boldsymbol{n}\cdot\left\langle \frac{1}{2}\boldsymbol{U}(\boldsymbol{u}'\cdot\boldsymbol{u}') + \boldsymbol{u}'(\boldsymbol{U}\cdot\boldsymbol{u}')\right\rangle \mathrm{d}S \\ +\delta^2\displaystyle\iint_S \boldsymbol{n}\cdot\langle \boldsymbol{u}'\times\boldsymbol{\omega}'\rangle \mathrm{d}S + \delta_d^2\iiint_V \langle \boldsymbol{u}'\cdot\nabla(\nabla\cdot\boldsymbol{u}')\rangle \mathrm{d}V \end{cases} \tag{4.26}$$

where in this case we use

$$\begin{cases} \boldsymbol{u}' = \hat{\boldsymbol{u}} + \tilde{\boldsymbol{u}} + \breve{\boldsymbol{u}} \\ p' = \hat{p} + \tilde{p} + \breve{p} \text{ (total representation)} \\ \boldsymbol{\omega}' = \tilde{\boldsymbol{\omega}} + \breve{\boldsymbol{\omega}} \end{cases} \tag{4.27}$$

Equation (4.24) has already been evaluated in many studies [3,20,66,67]. Our goal is to evaluate as much as possible Eq. (4.26) with Eq. (4.27). To do so, we first

separate $\alpha_{hyd}^{(1)}$ which represents all terms that have hydrodynamic wave effects from the vortical-acoustic terms. Then $\alpha_{hyd}^{(1)}$ can be written as

$$\alpha_{hyd}^{(1)} = \frac{1}{2E^2}\left\{\begin{array}{l} -\dfrac{1}{\gamma}\iint_S \boldsymbol{n}\cdot\left\langle \hat{p}\breve{\boldsymbol{u}} + \tilde{p}\breve{\boldsymbol{u}} + \breve{p}\breve{\boldsymbol{u}} + \breve{p}\hat{\boldsymbol{u}} + \breve{p}\tilde{\boldsymbol{u}}\right\rangle \mathrm{d}S \\ -\dfrac{M_b}{\gamma^3\bar{P}}\iint_S \boldsymbol{n}\cdot\boldsymbol{U}\left\langle \breve{p}^2 + 2\hat{p}\breve{p} + 2\tilde{p}\breve{p}\right\rangle \mathrm{d}S \\ -M_b\bar{P}\iint_S \boldsymbol{n}\cdot\left\langle \begin{array}{l} \dfrac{1}{2}\boldsymbol{U}(\hat{\boldsymbol{u}}\cdot\breve{\boldsymbol{u}} + \tilde{\boldsymbol{u}}\cdot\breve{\boldsymbol{u}} + \breve{\boldsymbol{u}}\cdot\hat{\boldsymbol{u}} + \breve{\boldsymbol{u}}\cdot\tilde{\boldsymbol{u}} + \breve{\boldsymbol{u}}\cdot\breve{\boldsymbol{u}}) \\ +(\hat{\boldsymbol{u}} + \tilde{\boldsymbol{u}} + \breve{\boldsymbol{u}})(\boldsymbol{U}\cdot\breve{\boldsymbol{u}}) \end{array}\right\rangle \mathrm{d}S \\ +\delta^2\iint_S \boldsymbol{n}\cdot\left\langle(\hat{\boldsymbol{u}} + \tilde{\boldsymbol{u}} + \breve{\boldsymbol{u}})\times\breve{\boldsymbol{\omega}} + \breve{\boldsymbol{u}}\times\tilde{\boldsymbol{\omega}}\right\rangle \mathrm{d}S \\ +\delta_d^2\iiint_V \left\langle\breve{\boldsymbol{u}}\cdot\nabla(\nabla\cdot\hat{\boldsymbol{u}})\right\rangle \mathrm{d}V \end{array}\right. \tag{4.28}$$

In order to put Eq. (4.28) in a more consistent form, there is a need to write the last term in surface form. To do so, the divergence theorem can be utilized. Therefore, the last term in Eq. (4.28) can be written as

$$\iiint_V \left\langle\breve{\boldsymbol{u}}\cdot\nabla(\nabla\cdot\hat{\boldsymbol{u}})\right\rangle \mathrm{d}V = \iiint_V \left\langle\nabla\cdot(\breve{\boldsymbol{u}}(\nabla\cdot\hat{\boldsymbol{u}}))\right\rangle \mathrm{d}V - \iiint_V \left\langle(\nabla\cdot\breve{\boldsymbol{u}})(\nabla\cdot\hat{\boldsymbol{u}}))\right\rangle \mathrm{d}V \tag{4.29}$$

Being incompressible, $\nabla\cdot\breve{\boldsymbol{u}} = 0$; this yields

$$\iiint_V \left\langle\breve{\boldsymbol{u}}\cdot\nabla(\nabla\cdot\hat{\boldsymbol{u}})\right\rangle \mathrm{d}V = \iiint_V \left\langle\nabla\cdot(\breve{\boldsymbol{u}}(\nabla\cdot\hat{\boldsymbol{u}}))\right\rangle \mathrm{d}V \tag{4.30}$$

The divergence theorem may now be applied. One gets

$$\iiint_V \left\langle\nabla\cdot(\breve{\boldsymbol{u}}(\nabla\cdot\hat{\boldsymbol{u}}))\right\rangle \mathrm{d}V = \iint_S \boldsymbol{n}\cdot\left\langle\breve{\boldsymbol{u}}(\nabla\cdot\hat{\boldsymbol{u}})\right\rangle \mathrm{d}S \tag{4.31}$$

By substituting back in Eq. (4.28), we collect

$$\alpha_{hyd}^{(1)}=\frac{1}{2E^2}\begin{cases}-\dfrac{1}{\gamma}\displaystyle\iint_S \boldsymbol{n}\cdot\left\langle\breve{\boldsymbol{u}}(\hat{p}+\tilde{p})+\breve{p}(\breve{\boldsymbol{u}}+\hat{\boldsymbol{u}}+\tilde{\boldsymbol{u}})\right\rangle \mathrm{d}S\\ -\dfrac{M_b}{\gamma^3\bar{\bar{P}}}\displaystyle\iint_S \boldsymbol{n}\cdot\boldsymbol{U}\left\langle\breve{p}^2+2\hat{p}\breve{p}+2\tilde{p}\breve{p}\right\rangle \mathrm{d}S\\ -M_b\bar{P}\displaystyle\iint_S \boldsymbol{n}\cdot\left\langle\begin{matrix}\dfrac{1}{2}\boldsymbol{U}(\hat{\boldsymbol{u}}\cdot\breve{\boldsymbol{u}}+\tilde{\boldsymbol{u}}\cdot\breve{\boldsymbol{u}}+\breve{\boldsymbol{u}}\cdot\hat{\boldsymbol{u}}+\breve{\boldsymbol{u}}\cdot\tilde{\boldsymbol{u}}+\breve{\boldsymbol{u}}\cdot\breve{\boldsymbol{u}})\\ +(\hat{\boldsymbol{u}}+\tilde{\boldsymbol{u}}+\breve{\boldsymbol{u}})(\boldsymbol{U}\cdot\breve{\boldsymbol{u}})+\breve{\boldsymbol{u}}\left(\boldsymbol{U}\cdot\hat{\boldsymbol{u}}+\boldsymbol{U}\cdot\tilde{\boldsymbol{u}}\right)\end{matrix}\right\rangle \mathrm{d}S\\ +\delta^2\displaystyle\iint_S \boldsymbol{n}\cdot\left\langle(\hat{\boldsymbol{u}}+\tilde{\boldsymbol{u}}+\breve{\boldsymbol{u}})\times\tilde{\boldsymbol{\omega}}+\breve{\boldsymbol{u}}\times\tilde{\boldsymbol{\omega}}\right\rangle \mathrm{d}S\\ +\delta_d^2\displaystyle\iint_S \boldsymbol{n}\cdot\left\langle\breve{\boldsymbol{u}}(\nabla\cdot\hat{\boldsymbol{u}})\right\rangle \mathrm{d}S\end{cases} \tag{4.32}$$

Hydrodynamic terms in Eq. (4.32) are normalized differently than those used to described the vortical-acoustic terms. This is caused by the two communities (i.e. combustion instability and hydrodynamic instability) using slightly different nomenclatures. In what follows, we shall attempt to reconcile between the two. We hence renormalize one set to fit the other. To do so, first we define the dimensionless parameter for each group. Second, we pick one of the groups and renormalize it to fit the other group. This is illustrated next.

4.3. Normalization

In combustion instability, we use the following normalization:

$$\begin{cases}\boldsymbol{U}=\dfrac{\boldsymbol{U}^*}{U_w}, \quad l=\dfrac{L}{R}, \quad r=\dfrac{\bar{r}}{R}\\ t=t^*\dfrac{a_0}{R}, \quad \delta^2=\dfrac{\nu}{a_0R}, \quad M_b=\dfrac{U_w}{a_0}\\ \hat{\boldsymbol{u}}=\dfrac{\hat{\boldsymbol{u}}^*}{a_0}, \quad \tilde{\boldsymbol{u}}=\dfrac{\tilde{\boldsymbol{u}}^*}{a_0}, \quad p=\dfrac{p}{p_0}\\ \tilde{\boldsymbol{\omega}}=\tilde{\boldsymbol{\omega}}^*\dfrac{R}{a_0}, \quad E=\dfrac{E^*}{\rho_0a_0^2R^3}, \quad \mathscr{E}=\dfrac{\mathscr{E}^*}{\rho_0a_0^2}\end{cases} \tag{4.33}$$

However, in hydrodynamic instability analysis, it is more convenient to use

$$\begin{cases} \boldsymbol{U} = \dfrac{\boldsymbol{U}}{U_w}, \quad l = \dfrac{L}{R}, \quad r = \dfrac{\bar{r}}{R} \\ t = t^* \dfrac{U_w}{R}, \quad \breve{\boldsymbol{u}} = \dfrac{\breve{\boldsymbol{u}}^*}{U_w} \\ p = \dfrac{p_0}{\rho_0 U_w^2}, \quad \omega_p = \omega_p^* \dfrac{R}{U_w}, \quad Re = \dfrac{U_w R}{\nu} \end{cases} \tag{4.34}$$

The only differences between the two groups are the reference velocity and pressure. While it is the speed of sound and the stagnation pressure in the combustion terms, wall injection and the dynamic pressure are used in the hydrodynamic terms. A close look at the problem of hydrodynamic instability shows that the eigenmodes of the spatial amplification, pressure, velocity, and vorticity amplitudes are independent of the normalization. In other words, the amplitudes do not change by changing reference values. To illustrate this point, the eigenvalue problem based on the hydrodynamic normalization can be written as

$$\begin{cases} \nabla \cdot \breve{\boldsymbol{u}} = 0 \\ \dfrac{\partial \breve{\boldsymbol{u}}}{\partial t} + (\nabla \boldsymbol{U}) \cdot \breve{\boldsymbol{u}} + (\nabla \breve{\boldsymbol{u}}) \cdot \boldsymbol{U} + \nabla \breve{p} = \dfrac{1}{Re} \Delta \breve{\boldsymbol{u}} \end{cases} \text{(hydrodynamic representation)} \tag{4.35}$$

This form is based on the injection velocity and dynamic pressure normalization. To renormalize the problem based on the speed of sound and the stagnation pressure, one must put

$$\begin{cases} \nabla \cdot \breve{\boldsymbol{u}} = 0 \\ \dfrac{\partial \breve{\boldsymbol{u}}}{\partial t} + M_b[(\nabla \boldsymbol{U}) \cdot \breve{\boldsymbol{u}} + (\nabla \breve{\boldsymbol{u}}) \cdot \boldsymbol{U}] + \nabla \breve{p} = \dfrac{M_b}{Re} \Delta \breve{\boldsymbol{u}} \end{cases} \text{(CI representation)} \tag{4.36}$$

Both forms yield the same eigenmodes, pressure, velocity, and vorticity amplitudes, if the normalized pressure at the surface is used for both cases. The only

difference is that the real frequency definition will be based on the speed of sound instead of the injection velocity. The corresponding frequencies will be defined as $f = k_m a_0 / (2\pi R)$ (CI representation) in lieu of $f = \omega U_w / (2\pi R)$ (hydrodynamic representation).

4.4. Energy Density

The energy density term, E^2 has both acoustic and vortical quantities as referenced in the literature. A recent study on the subject by Majdalani, Fischbach and Flandro [70] provides the complete steps in evaluating this term for both cylindrical and slab motor configurations. For the sake of completeness we will also include the energy that results from the hydrodynamic terms despite the fact it is expected to be much smaller than the vortical-acoustic energy. The idea here is to establish a solid linear model that has all details to make the transition to the nonlinear work much easier in the future.

The model established more recently by Flandro in [3,20,66,67] provides two methods for calculating the energy density. The first one is based on.

1. Relaxing the isentropic assumption.
2. A quiescent initial state is not assumed.
3. The unsteady gas motion is superimposed upon the quasi- steady gas flow.

Under these conditions, the energy density in terms of fluctuating velocity and pressure becomes (see Appendix B):

$$E^2 = \frac{1}{\gamma^3 \bar{P}} \left[p^{(1)} \right]^2 + \frac{1}{2} \rho \boldsymbol{u}^{(1)} \cdot \boldsymbol{u}^{(1)} \tag{4.37}$$

Note that this result compares favorably with the classical Kirchoff acoustic energy density, specifically

$$E^2 = \frac{1}{2\gamma^2}\left[p^{(1)}\right]^2 + \frac{1}{2}\rho \boldsymbol{u}^{(1)} \cdot \boldsymbol{u}^{(1)} \tag{4.38}$$

For consistency, the Kirchoff energy density will be used here. Although the hydrodynamic energy is suspected to be small compared to the vortical-acoustic energy, it will be developed and evaluated. After substituting Eq. (4.27) into Eq. (4.38) and separating the vortical-acoustic from the hydrodynamic terms, the new energy representation can be expressed as

$$E^2 = E^2_{vac} + E^2_{hyd} \tag{4.39}$$

where

$$E^2_{vac} = \frac{1}{2}\iiint_{\forall}\left\langle \hat{p}^2 + \hat{\boldsymbol{u}}\cdot\hat{\boldsymbol{u}} + 2\hat{\boldsymbol{u}}\cdot\tilde{\boldsymbol{u}}^i + \tilde{\boldsymbol{u}}^r\cdot\tilde{\boldsymbol{u}}^r + \tilde{\boldsymbol{u}}^i\cdot\tilde{\boldsymbol{u}}^i \right\rangle \mathrm{d}V \tag{4.40}$$

and

$$E^2_{hyd} = \frac{1}{2}\iiint_{\forall}\left\langle \underbrace{\breve{p}^2 + \breve{\boldsymbol{u}}\cdot\breve{\boldsymbol{u}}}_{\text{pure hydrodynamic}} \underbrace{+2\hat{p}\breve{p} + 2\breve{\boldsymbol{u}}\cdot\left(\tilde{\boldsymbol{u}}^r + \tilde{\boldsymbol{u}}^i + \hat{\boldsymbol{u}}\right)}_{\text{coupled terms}} \right\rangle \mathrm{d}V \tag{4.41}$$

We later evaluate and find E^2_{hyd} to be indeed negligible compared to E^2_{vac}.

4.5. Sidewall Analysis

To satisfy the no-slip condition on the surface, Eq. (4.32) can be written as

$$\alpha_{hyd}^{(1)} = \frac{1}{2E^2}\begin{cases} -\frac{1}{\gamma}\iint_S \boldsymbol{n}\cdot\left\langle \breve{p}(\hat{\boldsymbol{u}}+\tilde{\boldsymbol{u}})\right\rangle \mathrm{d}S \\ -\frac{M_b}{\gamma^3\overline{P}}\iint_S \boldsymbol{n}\cdot\boldsymbol{U}\left\langle \breve{p}^2+2\hat{p}\breve{p}+2\tilde{p}\breve{p}\right\rangle \mathrm{d}S \\ +\delta^2\iint_S \boldsymbol{n}\cdot\left\langle(\hat{\boldsymbol{u}}+\tilde{\boldsymbol{u}})\times\breve{\boldsymbol{\omega}}\right\rangle \mathrm{d}S \end{cases} \tag{4.42}$$

The latter expression represents the growth or decay rates from the surface caused by the presence of hydrodynamic instability terms. None of the terms in Eq. (4.42) can be neglected yet since all hydrodynamic terms are calculated numerically.

To evaluate the latter expression, a detailed analysis and physical interpretation should address all of the terms, one-by-one. The first term can be modified to include the admittance function which represents the sensitivity of the combustion process to the pressure fluctuation. The analogy behind the admittance function has been described in detail in the combustion instability framework [71,72]. As a result, the first term in Eq. (4.42) can be rewritten in the admittance function notation.

$$\boldsymbol{n}\cdot\hat{\boldsymbol{u}} = -M_b A_b^r \frac{\hat{p}}{\gamma}, \quad \boldsymbol{n}\cdot\tilde{\boldsymbol{u}} = -M_b \frac{\hat{p}}{\gamma} \tag{4.43}$$

Where A_b^r is the real part of the admittance function and only the normal velocity component is preserved. One should point out that, the unit normal vector $\boldsymbol{n}$ is positive outward from the control surface. Accordingly, the second term in Eq. (4.42) can be rewritten as:

$$\boldsymbol{n}\cdot\boldsymbol{U} = U_r\big|_{r=1} = -\left.\frac{\sin\left(\frac{1}{2}\pi r^2\right)}{r}\right|_{r=1} = -1 \tag{4.44}$$

The third component needs to be treated carefully realizing that a large amount of algebra is involved. We first expand the parietal vortices into three components $\breve{\omega} = \breve{\omega}_r \boldsymbol{e}_r + \breve{\omega}_\theta \boldsymbol{e}_\theta + \breve{\omega}_z \boldsymbol{e}_z$; each part is given by:

$$\omega_r = \Re\left(\frac{iqu_z}{r} - iku_z\right), \quad \omega_\theta = \Re\left(iku_r - \frac{\mathrm{d}u_z}{\mathrm{d}r}\right), \quad \omega_z = \Re\left[\frac{1}{r}\frac{\mathrm{d}(ru_\theta)}{\mathrm{d}r} - \frac{iqu_r}{r}\right] \tag{4.45}$$

Second, the vector term $(\hat{u} + \tilde{u})$ is also expanded into $(\hat{u}_r + \tilde{u}_r)\boldsymbol{e}_r + (\hat{u}_z + \tilde{u}_z)\boldsymbol{e}_z$. To satisfy the no slip condition at the burning surface we set $(\hat{u}_z + \tilde{u}_z)\big|_{r=1} = 0$; thus the product of the last term does not contribute to the energy. Consequently, the total growth rate that results from combustion and hydrodynamic instability coupling on the surface becomes

$$\alpha^{(1)}_{hyd,w} = \frac{1}{2E^2}\begin{cases} \dfrac{M_b(1+A_b^r)}{\gamma}\displaystyle\iint_S \langle \breve{p}\hat{p}\rangle \,\mathrm{d}S \\ + \dfrac{M_b}{\gamma^3 \bar{P}}\displaystyle\iint_S \left\langle \breve{p}^2 + 2\left(\hat{p}\breve{p} + \tilde{p}\breve{p}\right)\right\rangle \mathrm{d}S \end{cases} \tag{4.46}$$

Since an analytic solution is provided for all vortical-acoustic components, it is reasonable to ignore terms of smaller order. As it was described in the literature (see Flandro and Majdalani [18]) $\tilde{p}$ is of order $O(M_b^2)$ where $\hat{p}$ is of order $O(M_b)$. This makes the term $\tilde{p}\breve{p} \ll \hat{p}\breve{p}$ and justifies ignoring it in Eq. (4.46). For that, Eq. (4.46) becomes:

$$\alpha^{(1)}_{hyd,w} = \frac{1}{2E^2}\begin{cases} \dfrac{M_b(1+A_b^r)}{\gamma}\displaystyle\iint_S \langle \breve{p}\hat{p}\rangle \,\mathrm{d}S \\ + \dfrac{M_b}{\gamma^3 \bar{P}}\displaystyle\iint_S \left\langle \breve{p}^2 + 2\hat{p}\breve{p}\right\rangle \mathrm{d}S \end{cases} \tag{4.47}$$

4.6. Nozzle Exit Analysis

Equation (4.32) can also be applied to the nozzle exit plane where it is expected to have a damping effect. It may also have a driving effect but that behavior has not been fully investigated. To simplify the problem, the nozzle exit is assumed to be an open channel where the compressibility is ignored. Also, no geometrical effects are considered, such as corner collisions, angle-corner interactions, turbulence and recirculation that tend to drastically alter the flow. In addition, all terms in the order of $O(M_b^2)$ will be ignored. For the hydrodynamic components, all terms will be kept until being evaluated. The normal unit vector $\boldsymbol{n} = \hat{\boldsymbol{k}}$ and $\mathrm{d}S = r\mathrm{d}r\mathrm{d}\theta$ are used. In general, Eq. (4.32) can be expressed at the nozzle exit, without considering any of the previous assumptions:

$$\alpha_{hyd,N}^{(1)} = -\frac{1}{2E^2}\left\{\begin{array}{l} \dfrac{1}{\gamma}\iint_S \left\langle \breve{u}_z(\hat{p}+\tilde{p}) + \breve{p}(\breve{u}_z+\hat{u}_z+\tilde{u}_z)\right\rangle \mathrm{d}S + \dfrac{M_b}{\gamma^3\overline{P}}\iint_S U_z\left\langle \breve{p}^2 + 2\hat{p}\breve{p} + 2\tilde{p}\breve{p}\right\rangle \mathrm{d}S \\ +M_b\overline{P}\iint_S \left\langle \begin{array}{l} \dfrac{1}{2}U_z\left[2\left(\hat{u}_r\breve{u}_r+\hat{u}_z\breve{u}_z\right)+2\left(\tilde{u}_r\breve{u}_r+\tilde{u}_z\breve{u}_z\right)+\left(\breve{u}_r^2+\breve{u}_\theta^2+\breve{u}_z^2\right)\right] \\ +(\hat{u}_z+\tilde{u}_z+\breve{u}_z)\left(U_r\tilde{u}_r+U_z\tilde{u}_z\right)+\breve{u}_z\left[\begin{array}{l}\left(U_r\hat{u}_r+U_z\hat{u}_z\right)\\ +\left(U_r\tilde{u}_r+U_z\tilde{u}_z\right)\end{array}\right] \end{array}\right\rangle \mathrm{d}S \\ -\delta^2\iint_S\left\langle(\hat{u}_r+\tilde{u}_r+\breve{u}_r)\tilde{\omega}_\theta+\breve{u}_r\tilde{\omega}\right\rangle \mathrm{d}S - \delta_d^2\iint_S\left\langle\left[\dfrac{1}{r}\dfrac{\partial}{\partial r}(r\hat{u}_r)+\dfrac{\partial\hat{u}_z}{\partial z}\right]\breve{u}_z\right\rangle \mathrm{d}S \end{array}\right. \tag{4.48}$$

By introducing appropriate assumptions for the nozzle, Eq. (4.48) reduces to

$$\alpha_{hyd,N}^{(1)} = \frac{1}{2E^2}\left\{\begin{array}{l} -\dfrac{1}{\gamma}\iint_S\left\langle\breve{u}_z\hat{p}+\breve{p}(\breve{u}_z+\hat{u}_z)\right\rangle \mathrm{d}S - \dfrac{M_b}{\gamma^3\overline{P}}\iint_S U_z\left\langle\breve{p}^2+2\hat{p}\breve{p}\right\rangle \mathrm{d}S \\ -M_b\overline{P}\iint_S\left\langle\dfrac{1}{2}U_z\left[\begin{array}{l}2\left(\hat{u}_r\breve{u}_r+\hat{u}_z\breve{u}_z\right)\\ +\left(\breve{u}_r^2+\breve{u}_\theta^2+\breve{u}_z^2\right)\end{array}\right]+\breve{u}_z\left[\left(U_r\hat{u}_r+U_z\hat{u}_z\right)\right]\right\rangle \mathrm{d}S \end{array}\right. \tag{4.49}$$

Further reduction in the system above can be pursued knowing that the acoustic radial component is smaller in order of magnitude than the axial one. This results in

$$\alpha_{hyd,N}^{(1)} = \frac{1}{2E^2}\begin{cases} -\frac{1}{\gamma}\iint_S \left\langle \breve{u}_z\hat{p} + \breve{p}(\breve{u}_z + \hat{u}_z)\right\rangle \mathrm{d}S - \frac{M_b}{\gamma^3\overline{P}}\iint_S U_z\left\langle \breve{p}^2 + 2\hat{p}\breve{p}\right\rangle \mathrm{d}S \\ -M_b\overline{P}\iint_S \left\langle \frac{1}{2}U_z\left[2\hat{u}_z\breve{u}_z + \left(\breve{u}_r^2 + \breve{u}_\theta^2 + \breve{u}_z^2\right)\right] + \breve{u}_z U_z\hat{u}_z\right\rangle \mathrm{d}S \end{cases} \tag{4.50}$$

Again, no assumption on the hydrodynamic part has been made because these terms have to be numerically calculated before their order is extracted.

4.7. Time Averaging

By definition the time average over a time T of a time dependent quantity $f(t)$ is given by

$$\langle f(t)\rangle = \lim_{T\to\infty}\frac{1}{T}\int_0^T f(t)dt \tag{4.51}$$

where T can be a cycle or many cycles of oscillation.

The hydrodynamic and combustion waves can be expressed as follows. First, for the hydrodynamic pressure, one can put

$$\breve{p} = A_0 p e^{i\left[\int_{z_0}^{z}(\sigma_r + i\sigma_i)\mathrm{d}z + q\theta - \omega t\right]} \tag{4.52}$$

Here p is a complex number which can be split into $p = p^r + ip^i$; one may also use the Euler notation. In this case p can be represented as

$$p = |p|e^{i\beta_p}\ ; \quad \begin{cases} |p| = \sqrt{\left(p^r\right)^2 + \left(p^i\right)^2} \\ \beta_p = \tan^{-1}\left(\dfrac{p^i}{p^r}\right) \end{cases} \tag{4.53}$$

In what follows, Eq. (4.52) can be rewritten as:

$$\breve{p} = A_0 |p| e^{i\left[\int_{z_0}^{l} (\sigma_r + i\sigma_i) dz + q\theta + \beta_p - \omega t\right]} \tag{4.54}$$

By taking the real part from Eq. (4.54) and using trigonometric identities to separate the time dependence from the space dependence one can write Eq. (4.54) in the following form:

$$\breve{p} = A_0 |p| \left[\cos\left(n_r + q\theta + \beta_p\right)\cos\left(\omega t\right) + \sin\left(n_r + q\theta + \beta_p\right)\sin\left(\omega t\right)\right] e^{n_i} \tag{4.55}$$

Following the same procedure, the velocity fluctuation can be written as:

$$\breve{u} = A_0 |u| \left[\cos\left(n_r + q\theta + \beta_u\right)\cos\left(\omega t\right) + \sin\left(n_r + q\theta + \beta_u\right)\sin\left(\omega t\right)\right] e^{n_i} \tag{4.56}$$

Here n_r and n_i represent the integral wave number and the space amplification, respectively; these are given by

$$n_r = \int_{z_0}^{z} \sigma_r dz, \cdots n_i = -\int_{z_0}^{z} \sigma_i dz \tag{4.57}$$

In Eq. (4.57), z_0 represents the axial location where the flow initially breaks down (i.e. the first axial station where the disturbances begin to amplify). Moreover, from hydrodynamic theory, it is assumed that $z_0 = z_0(\omega)$. Another important quantity is A_0, which represents the initial wave amplitude at z_0. This value cannot be calculated in the linear theory, but it can be inferred if experimental measurements are available. In the present study, we will show, based on some experimental facts, that the initial amplitude is not only frequency dependent, but may also depend on the aspect ratio l. As such, we write $A_0 = A_0(\omega, l)$.

Since complex notation is used in our calculation, a definition of the amplitude as well as the phase angle should be introduced. The solution of the vortical-acoustic part cannot directly be used in the calculation because it does not provide a quantification of

the wave number or frequency. The acoustic part is normalized in such a way that either the wave number or frequency can be directly deduced from k_m. However, the latter description can be written in terms of the dimensionless hydrodynamic frequency. As it has been demonstrated through experimental measurements [44], the acoustic frequency is the controlling frequency. Any frequency for the parietal vortex shedding will die out except for the one that matches the acoustic frequency. This fact makes the analysis much simpler and the effect of vortex shedding much easier to pursue. Now for the acoustic part, the axial and vortical components can be described as follows:

A. Acoustic part

$$\begin{cases} \hat{u} = -i\hat{u}_m e^{ik_m t} \\ \hat{p} = \hat{p}_m e^{ik_m t} \end{cases} \quad \text{or} \quad \begin{cases} \hat{u}_z = \sin(k_m z)\sin(k_m t) \\ \hat{p} = \cos(k_m z)\cos(k_m t) \end{cases} \text{(real part)} \tag{4.58}$$

B. Vortical part:

$$\begin{cases} \tilde{u} = (\tilde{u}_m^r + i\tilde{u}_m^i)e^{ik_m t} \\ \tilde{p} = (\tilde{p}_m^r + i\tilde{p}_m^i)e^{ik_m t} \end{cases} \quad \text{or} \quad \begin{cases} \tilde{u} = \tilde{u}_m^r \cos(k_m t) + \tilde{u}_m^i \sin(k_m t) \\ \tilde{p} = \tilde{p}_m^r \cos(k_m t) + \tilde{p}_m^i \sin(k_m t) \end{cases} \tag{4.59}$$

The real wave number and frequency can be extracted directly from k_m based on:

$$f_{vac} = k_m a_0 / (2\pi R) \text{ (Hz)} \tag{4.60}$$

The value of k_m can be deduced directly in terms of the hydrodynamic frequency by setting the dimensional hydrodynamic frequency equal to the acoustic one. It should be noted that either representation of hydrodynamic instability (via Eq. (4.35) or (4.36)) is valid. For convenience, the first representation is used since all hydrodynamic results so far have been based on it. As a result, the relation between k_m and ω becomes

$$k_m = M_b \omega \tag{4.61}$$

Another term needs to be corrected before proceeding in the analysis. The acoustic time is normalized by the speed of sound a_0; in contrast, the hydrodynamic time is normalized by the injection velocity U_w. It should be clear that the dimensional time should be the same for both waves. Having said that, the dimensionless acoustic time in term of dimensionless hydrodynamic time is given by:

$$t_{vac} = t_{hyd} / M_b \tag{4.62}$$

From this point forward, the hydrodynamic time will be used without subscript. Substituting Eqs. (4.61) and (4.62) back into Eqs. (4.58) and (4.59) and using real parts leads to

C. Acoustic part

$$\begin{cases} \hat{u}_z = \sin\left(M_b \omega z\right) \sin\left(\omega t\right) \\ \hat{p} = \cos\left(M_b \omega z\right) \cos\left(\omega t\right) \end{cases} \tag{4.63}$$

D. Vortical part

$$\begin{cases} \tilde{\boldsymbol{u}} = \tilde{\boldsymbol{u}}_m^r \cos(\omega t) + \tilde{\boldsymbol{u}}_m^i \sin(\omega t) \\ \tilde{p} = \tilde{p}_m^r \cos(\omega t) + \tilde{p}_m^i \sin(\omega t) \end{cases} \tag{4.64}$$

Now, time averaging can be done (see Appendix C) and Eqs. (4.47) and (4.50) become:

First, for $q = 0$, one has

$$\alpha_{hyd,w}^{(1)} = \frac{\pi}{E^2} \begin{cases} \dfrac{M_b (1 + A_b^r)}{2\gamma} \int_{z_0}^{l} \left[A_0 |p| \hat{p}_m \cos\left(n_r + \beta_p\right) \right] e^{n_i} \mathrm{d}z \\ + \dfrac{M_b}{\gamma^3 \overline{P}} \int_{z_0}^{l} \left\{ \dfrac{A_0^2}{2} |p|^2 e^{n_i} + A_0 |p| \hat{p}_m \left[\cos\left(n_r + \beta_p\right) \right] \right\} e^{n_i} \mathrm{d}z \end{cases} \quad \text{(surface)} \tag{4.65}$$

$$\alpha^{(1)}_{hyd,N} = \frac{\pi}{E^2}\begin{cases} -\dfrac{1}{2\gamma}\displaystyle\int_0^1 \left\{ \begin{array}{l} A_0 |u_z| \hat{p}_m \cos\left(n_r + \beta_p\right) \\ + A_0 \breve{p}_m \left[A_0 |u_z| \cos\left(\beta_p - \beta_{u_z}\right) e^{n_i} + \hat{u}_{m_z} \sin\left(n_r + \beta_p\right) \right] \end{array} \right\} e^{n_i} r\,\mathrm{d}r \\ -\dfrac{M_b}{\gamma^3 \overline{P}} \displaystyle\int_0^1 U_z \left\{ \tfrac{1}{2} A_0^2 |p|^2 e^{n_i} + A_o |p| \hat{p}_m \left[\cos\left(n_r + \beta_p\right) \right] \right\} e^{n_i} r\,\mathrm{d}r \\ -M_b \overline{P} \displaystyle\int_0^1 \tfrac{1}{2} U_z \left\{ \begin{array}{l} \left[A_0 \hat{u}_{m_z} |u_z| \left[\sin\left(n_r + \beta_p\right) \right] + \tfrac{1}{2} A_0^2 \left(|u_r|^2 + |u_z|^2 \right) e^{n_i} \right] \\ + A_0 \hat{u}_{m_z} |u_z| \left[\sin\left(n_r + \beta_p\right) \right] \end{array} \right\} e^{n_i} r\,\mathrm{d}r \end{cases}$$

(nozzle) (4.66)

Second, for $q \geq 1$,

$$\alpha^{(1)}_{hyd,w} = \frac{M_b A_0^2 \pi}{2\gamma^3 \overline{P} E^2} \int_0^1 |p|^2 e^{2n_i} \mathrm{d}z \text{ (surface)} \tag{4.67}$$

$$\alpha^{(1)}_{hyd,N} = -\frac{A_o^2 \pi e^{2n_i}}{E^2} \begin{cases} \dfrac{M_b}{2\gamma^3 \overline{P}} U_z \displaystyle\int_0^1 |p|^2 r\,\mathrm{d}r \\ \dfrac{M_b \overline{P}}{4} U_z \displaystyle\int_0^1 \left(|u_r|^2 + |u_\theta|^2 + |u_z|^2 \right) r\,\mathrm{d}r \end{cases} \text{ (nozzle)} \tag{4.68}$$

Also, the time averaging of the energy density is carried out in the same way. For that Eq. (4.40) becomes

$$E^2_{vac} = \frac{1}{2} \iiint_V \left(\hat{p}_m^2 + \hat{\boldsymbol{u}}_m \cdot \hat{\boldsymbol{u}}_m + 2\hat{\boldsymbol{u}}_m \cdot \tilde{\boldsymbol{u}}^i_m + \tilde{\boldsymbol{u}}^r_m \cdot \tilde{\boldsymbol{u}}^r_m + \tilde{\boldsymbol{u}}^i_m \cdot \tilde{\boldsymbol{u}}^i_m \right) \mathrm{d}V \tag{4.69}$$

and not to forget the hydrodynamic contribution in Eq. (4.41) which has two cases depending on the tangential wave number.

First, for $q = 0$

$$E_{hyd}^2 = \frac{1}{2}\iiint_V \left(\begin{array}{l} \underbrace{\frac{1}{2}A_0^2\left(|p|^2+|u_r|^2+|u_z|^2\right)e^{2n_i}}_{\text{pure hydrodynamic}} + \underbrace{\hat{p}_m|p|\cos\left(n_r+\beta_p\right)e^{n_i}}_{\text{coupled terms}} \\ \underbrace{+A_0|u_z|\left\{\left[\begin{array}{l}\tilde{u}_{m_z}^r\cos\left(n_r+\beta_{u_z}\right) \\ +\left(\tilde{u}_{m_z}^i+\hat{u}_{m_z}\right)\sin\left(n_r+\beta_{u_z}\right)\end{array}\right]\right\}e^{n_i}}_{\text{coupled terms}} \end{array} \right) \mathrm{d}V \qquad (4.70)$$

Second, for $q \geq 1$

$$E_{hyd}^2 = \frac{1}{2}\iiint_V \left\{ \underbrace{\frac{1}{2}A_0^2\left(|p|^2+|u_r|^2+|u_\theta|^2+|u_z|^2\right)e^{2n_i}}_{\text{pure hydrodynamic}} \right\} \mathrm{d}V \qquad (4.71)$$

The value of A_0 affects most equations. In order to pursue with the calculation, this value has to be defined or at least approximated to the right order. To do so, some facts need to be introduced to facilitate the calculation of A_0. First, Ugurtas [73] has suggested that the acoustic waves are created by vortices crossing the exit plane. Also Howe [74,75] has shown that the coupling between acoustic and aerodynamic waves can occur in the vicinity of the exit section. Finally, the exit pressure must be constant as reported by Griffond [45], which means there cannot be any pressure fluctuation at the exit section. Since the pressure fluctuations are associated with the downstream propagating parietal instability, their contribution at the exit section must be compensated by opposite incoming pressure. This assumption is consistent with the three latter facts. Accordingly, one can write

$$\int_{r=0}^{r=1} \hat{p}\left(z_{exit},t\right) r \mathrm{d}r = -\int_{r=0}^{r=1} \breve{p}\left(r,z_{exit},t\right) r \,\mathrm{d}r \qquad (4.72)$$

But since the acoustic pressure is independent of the radial direction, the relation can be simplified as:

$$\hat{p}(z_{exit},t) = -2\int_0^a p(r,z_{exit},t)\,r\,\mathrm{d}r \tag{4.73}$$

And, by using the definition of $\breve{p}$, one can put

$$\breve{p}(r,z,t) = A_0 p(r) e^{i\left(\int_{z_0}^{z}\sigma\,\mathrm{d}z + q\theta - \omega t\right)} \tag{4.74}$$

Using Eq. (4.52) to replace $\breve{p}$, the value of A_0 can be extracted and written as:

$$A_0 = -\frac{\hat{p}_m e^{-n_i}}{2\int_0^a |p|\cos(n_r + q\theta)\,r\,\mathrm{d}r} \tag{4.75}$$

The value of A_0 has been calculated for the first acoustic mode, and its range is found to be between $\left(3\times10^{-4} - 6\times10^{-4}\right)$. Griffond and Casalis [25] use a value of A_0 equal to $1/2000$ in their analysis to compare their theoretical results with experimental results by [76]. This value agrees to a certain limit with the calculated one.

4.8. Numerical Procedure

The numerical integrals of Eqs. (4.65) – (4.71) and (4.75) are carried out by using the Gaussian quadrature technique [77]. In this method, a single numerical integral can be written in the form of

$$I = \int_a^b f(x)\,\mathrm{d}x = \sum_i^n C_i f(x_i) \tag{4.76}$$

where the values of C_i and x_i are chosen so that the integral of a polynomial $2n-1$ is exact. Equation (4.76) can be rearranged so that the range of integration is bounded

between $t=-1$ and $t=+1$. This transformation will simplify the integral. The integral is now written as

$$I=\frac{b-a}{2}\int_{t=-1}^{t=1}F(x)\,\mathrm{d}x=\frac{b-a}{2}\sum_{i=1}^{n}C_iF(t_i) \tag{4.77}$$

The only problem in the previous equation is to solve for C_i and t_i which depend on the number of data points required for the integral. The mapping from interval $[a,b]$ to interval $[-1,+1]$ requires the linear transformation

$$x=mt+c \tag{4.78}$$

where $m=(b-a)/2$ and $c=(b+a)/2$. To proceed with the integral in the axial direction, we use $a=z_0$ and $b=l$; the values of m and c become $(l-z_0)/2$ and $(l+z_0)/2$, respectively. Here l represents the aspect ratio, and z_0 is the point taken at the neutral curve where the flow first begins to breakdown at a certain frequency. In the same way, to obtain the integral in the radial direction, we use $a=0$ and $b=1$, thus the values of m and c become $1/2$ since the integral is bounded on [0,1].

Equations (4.65)−(4.71) require either single or double integral operations because they are independent of the tangential direction. The double integral can be simply extracted in the same way as in the single integral. As an example, let us consider the double integral:

$$I=\int_c^d\int_a^b f(x,y)\,\mathrm{d}x\,\mathrm{d}y \tag{4.79}$$

Equation (4.79) can be written now in the form:

$$I=\int_c^d\left(\int_a^b f(x,y)\,\mathrm{d}x\right)\mathrm{d}y=\int_c^d F(y)\,\mathrm{d}y \tag{4.80}$$

where $F(y)=\int_a^b f(x,y)\,dx\cdots$, $y=$ constant. The double integral is evaluated in two steps.

First, we evaluate $F(y)$ at a selected y value then I is evaluated. At the outset, I can be written as

$$I = m_x m_y \sum_{j=1}^{n} C_j \sum_{i=1}^{n} C_i F(t_i, t_j) \tag{4.81}$$

Note that $x = m_x t_i + c_x$ and $y = m_y t_j + c_y$, where $m_x = (b-a)/2$, $c_x = (b+a)/2$, $m_y = (d-c)/2$, and $c_y = (d+c)/2$.

In order to capture the oscillation in the radial direction, we take the same number of points n in the integral code as in the eigensolver code (i.e. 150 points). The same number of points is used in the axial direction to simplify the analysis. The only problem that we must overcome is the difference in discretization between the hydrodynamic code (eigensolver) and the integral code in the axial direction. While a fixed step size is used in the hydrodynamic code for any frequency, a variable step size is used at different frequencies in the integral code to maintain the 150 points. For that, to use the information from the hydrodynamic code in the integral code, the eigenmodes and amplitudes are redistributed to fit the 150 points. Equations (4.65)–(4.68) and (4.70)–(4.71) are written in Appendix C as a summation to be implemented in coding.

5. Results and Discussion

The hydrodynamic instability results can be introduced without taking into effect the coupling with the acoustic waves. While the acoustic waves are temporally amplified, the hydrodynamic waves are spatially and temporally amplified. But because the spatial theory is more relevant in hydrodynamic instability [24,25,64], the hydrodynamic waves introduce a lengthscale rather than a timescale as in the case of an acoustic wave. Another fact to justify the superposition is that the acoustic waves are characterized by large wavelengths and a propagation velocity equal to the speed of sound, whereas the hydrodynamic waves have much shorter wavelengths, and a propagation velocity equal to a fraction of the flowfield velocity [42,45].

A verification of the numerical procedure used to solve Eq. (3.18) subject to Eq. (3.17) can be carried out by applying our algorithm to the special case of $u_h = 0$. Results are illustrated in Table 5-1 and these are compared to published data [27]. They are also summarized in a recent paper by Abu-Irshaid, Majdalani and Casalis [78]. Note the favorable agreement between the present code and that used by Griffond and Casalis [25]. Solutions are matching in five-to-ten significant digits.

From a practical standpoint, we recognize that the effect of the headwall injection constant u_h must be carefully investigated alongside the effect of varying the tangential wave number. The graph for the iso-n factor is first computed for four cases involving $u_h = 0.5$, $Re = 5,000$, and $q = 0,1,2,3$; these cases represent the first four tangential fluctuation modes of an SRM with headwall burning. The iso-n factors represent the spatial amplification of the flow and can be computed from fixed values of Re, q, z, and

Table 5-1. Eigenvalues of the Culick profile at $\omega = 90$, $z = 10$, $q = 0$, and $Re = 4{,}500$

	Griffond, Casalis and Pineau [25]		Current code	
Mode	σ_r	σ_i	σ_r	σ_i
1	6.0952945656	−1.0787998140	6.0952945724	−1.0787998101
2	3.3264285366	−0.1095525589	3.3264285380	−0.1095525581
3	2.6013223310	0.1322870315	2.6013223554	0.1322830025

ω. The amplitude of the wave A is calculated by integrating the local amplification growth rate ($-\sigma_i$) as described in Eq. (5.1) (see Gaster [79]): the value of $z_0(\omega)$, the first axial position where marginal stability is reached, depends on these fixed values via

$$A(z,\omega) = A_0 e^n \quad \text{with } n(z,\omega) = -\int_{z_0(\omega)}^{z} \sigma_i(\xi,\omega)\,\mathrm{d}\xi \tag{5.1}$$

Here A_0 represents the last stable amplitude along the neutral curve prescribed by $n = 0$. The iso-n graph in Fig. 5-1 provides the necessary information to determine the spatial position at which the flow starts to amplify. However, other useful features can be identified based on this graph.

First, one may recognize the unstable region to be enclosed within the classic L-shaped boundary. The vertical range of unstable frequencies increases in the streamwise direction.By the same token, for each specific frequency above the horizontal branch of the curve, the n-factor increases as the flow approaches the downstream end of the chamber. Second, the axial position of the most amplified frequency seems to change very gradually with successive increases in q. Only a minor shift in the neutral curve is detected. Third, flow stability at a spatial position seems to increase at higher wave numbers as a result of the curves shifting in the positive z direction. This point can be seen more clearly by comparing the neutral curves at several tangential wave numbers.

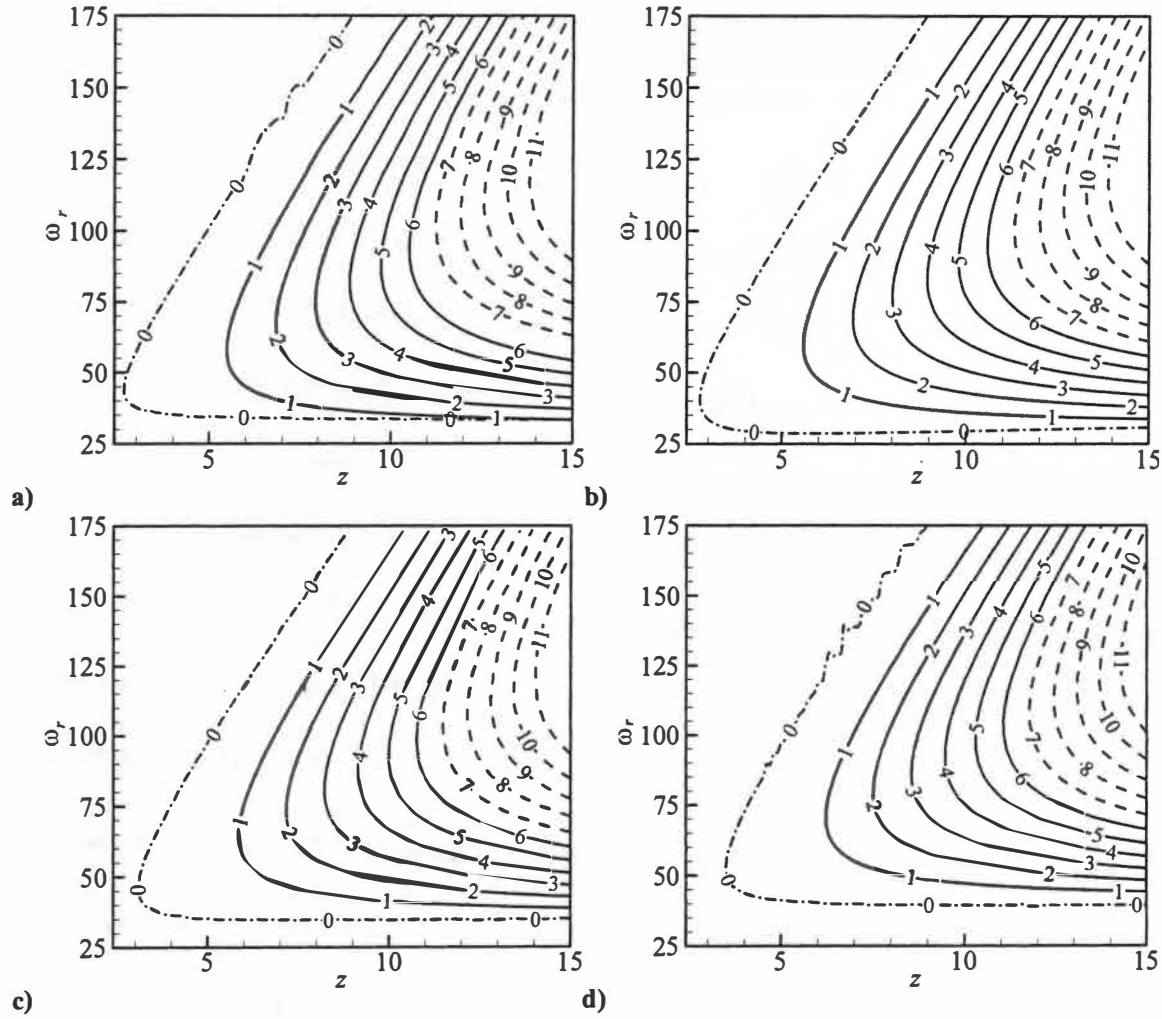

Figure 5-1. Iso-*n* factors for Re = 5,000 and u_h = 0.5. Results are shown in a) through d) for q = 0, 1, 2 and 3.

Figure 5-2 displays the neutral curves of Fig. 5-1 for $q = 0,1,2$ and 3. These represent the lines along which the flow begins to destabilize. It can be seen that the largest unstable frequency at a given z is nearly the same at all tangential wave modes. This can be attributed to the overlapping of the upper branch of the neutral curves past $z = 6$. For a sufficiently high frequency, the neutral curves at different wave numbers begin to overlap to the extent of becoming nearly imperceptible; this duplicitous behavior is confounding to the extent of making it difficult to isolate modes at a given frequency during experimental measurements [25,56]. On the other hand, due the continual spatial shifting of the lower branch in the streamwise direction (as the wave number is increased), the $q = 0$ case appears to be the most amplified. In fact, the two lowest modes, $q = 0,1$, are nearly indiscernible; this trend can make them difficult to decipher from experimental measurements. Note that a double shooting technique has been developed to specifically calculate the lines along which both σ_i and ω_i vanish simultaneously. This approach serves a dual purpose. First, it enables us to directly and

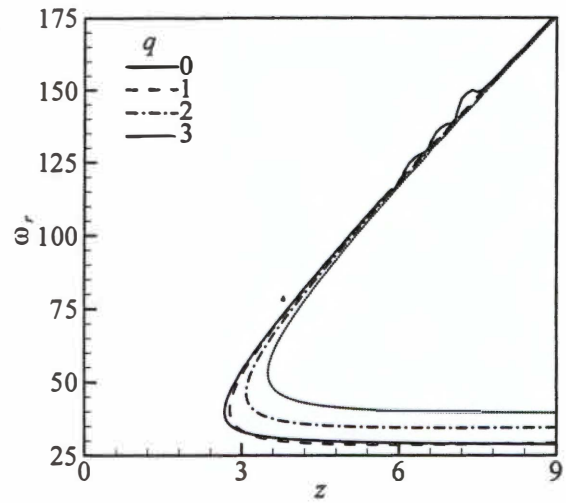

Figure 5-2. Neutral curves for different values of q at Re = 5,000 and u_h = 0.5.

expeditiously locate the neutral points, thus obviating the need to sweep horizontally across the domain to tag each of the neutral points individually. Second, as a consequence to the first, a larger number of points can be collected in a shorter period of time. This improves our resolution by permitting the use of finer increments and, thereby, deduce smoother curves.

Another observation that can be made based on Fig. 5-2 is that the flow is always stable below a certain frequency; in that respect, each neutral curve shows a tip that depends on the fixed parameters, Re, q, and u_h. For example, in the most dominant cases of $q = 0$ and 1, the flow is always stable below a threshold frequency of $\omega_r = 28.5$; the critical values (i.e., the tips of the neutral curves) are captured at $z \simeq 2.6$ and 2.7 with a common $\omega_r = 43$ and $\sigma_r \simeq 6.40$ and 6.23, respectively. For $q = 2$, the frequency above which instability starts increases to $\omega_r = 34$; this occurs at $\omega_r = 47$, $z \simeq 3$ and $\sigma_r \simeq 6.67$. Similar trends depicting an upward shift in frequency is reported with further increases in the wave number. This behavior confirms the $q = 0$ case as being the most critical.

To examine the effect of the injection headwall constant, neutral curves for different values of u_h are processed and plotted in Fig. 5-3. Clearly, as u_h increases, the flow becomes gradually more unstable; the corresponding neutral curves steadily shift upstream. The critical value, in this case, starts at the headwall injection point when the injection constant reaches $u_h \simeq 3.168$.

When $u_h > 3.168$, there will exist a range of frequencies for which the flow becomes unstable starting at the injection point itself, $z = 0$; the spectrum of frequencies widens with further departures from $u_h = 3.168$. One should point out that the critical

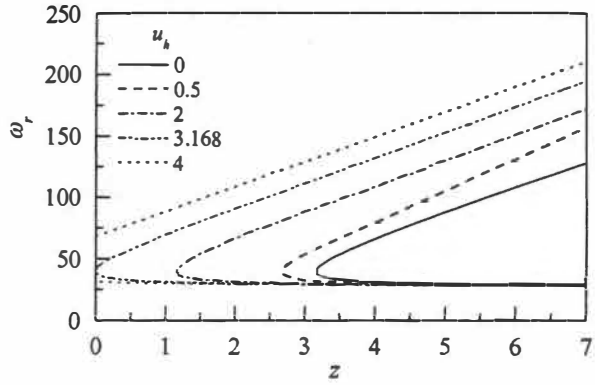

Figure 5-3. Using Re = 5,000 and q =0, we present the neutral curves for simulated SRM and SRM with headwall burning.

value of u_h varies with the tangential wave number. However, the $q = 0$ case shown here remains the most critical.

As the headwall-to-sidewall injection ratio becomes large (see Fig. 5-4), the flow streamlines start to resemble those of a circular-port hybrid rocket chamber [37]. By way of illustration, two values of u_h, $(10, 50)$, are selected. Here too, the range of unstable frequencies is seen to expand significantly at higher headend injection rates. It may be helpful to mention that the lowest frequency, where the flow starts to amplify (i.e., the frequency where the lower, horizontal segment of the neutral curve starts to swerve) is weakly sensitive to u_h (see Fig. 5-3). In contrast, the tip location and the highest unstable frequency are strongly affected by u_h. The tip moves upstream and the highest frequency increases as u_h is augmented. Additionally, as illustrated previously in Fig. 5-2, these features are dependent on the tangential wave number q. The impact of u_h on controlling the tip and the upper branch of the neutral curve is clearly seen in Fig. 5-4; accordingly, the flow regains stability at $\omega_r \geq (185, 770)$ for $u_h = (10, 50)$, respectively.

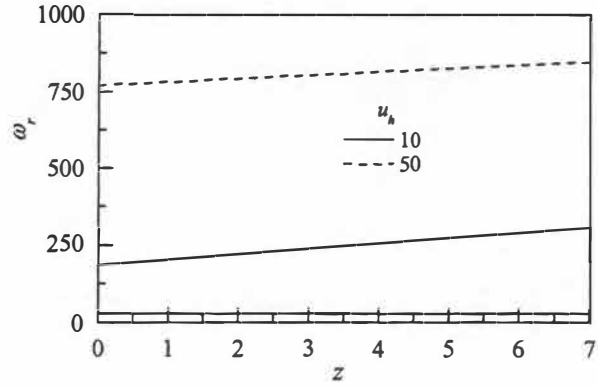

Figure 5-4. Using Re = 5,000 and q =0, we present the neutral curves for simulated solid or hybrid rocket engines with headwall injection.

Another interesting behavior that can be captured is the effect of Reynolds number on motor stability. To that end, Fig. 5-5 is used to illustrate the effect of Re on the position and size of the neutral curve. These determine the first abscissas at which instability can be experienced and the range of amplified frequencies, respectively. For $Re \geq 2,000$, a clustering in the neutral curves can be seen; this weak sensitivity to the Reynolds number marks the beginning of inviscid behavior. The reason for keeping the viscous terms in our model is to overcome the deficiency caused by the singularity at the centerline $(r = 0)$. This is, of course, characteristic of the choice of the cylindrical coordinate system.

As shown in Fig. 5-6, the longitudinal wave number and the amplification rate $(\sigma_r, -\sigma_i)$ become independent of Re above a certain threshold value, namely, one that is often termed the critical Reynolds number, Re_c. Essentially, both σ_r and $-\sigma_i$ reach their asymptotic values when the Reynolds number exceeds Re_c. This value represents the starting point for which inviscid behavior will prevail.

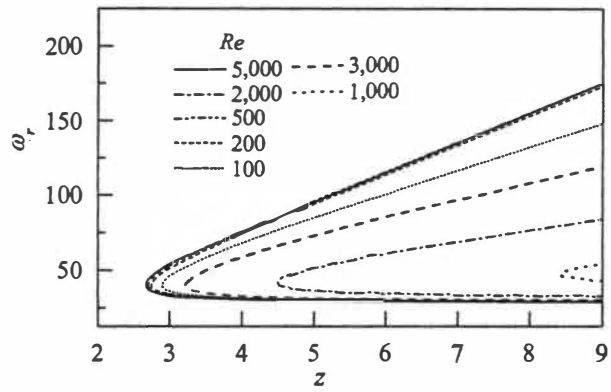

Figure 5-5. Using Re = 5,000 and q =0, we present the neutral curves for the effect of Reynolds number on the spatial shift in stability for a simulated SRM with headwall burning (q = 0 and u_h = 0.5).

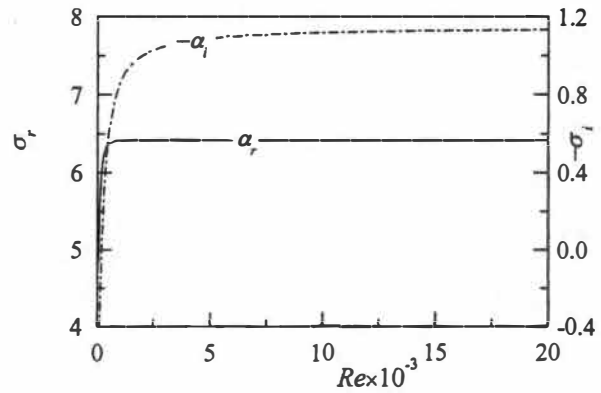

Figure 5-6. Using Re = 5,000 and q =0, we present the behavior of the streamwise wave number and the amplification rate over a wide range of Reynolds numbers and fixed values of ω = 80 and z = 9.

For the special case shown in Fig. 5-6, the critical value of Reynolds number is found to be $Re_c \simeq 2,225$. Note that the wave number tends to the inviscid limit faster than the growth rate and that the deviation in σ_i is quite minute (cf. right-hand-scale). For $Re \geq 5,000$, no change may be observed and this justifies its adoption in the present analysis.

It is important to show how the fluctuating velocities or pressures amplify with distance z. For this purpose we choose to plot the fluctuating velocities and pressure in the form of $A_0 \boldsymbol{u}(r) e^{n_i}$ and $A_0 p(r) e^{n_i}$ instead of just the amplitude $\boldsymbol{u}$ or p. The first form shows at what radial distance the wave has a maximum amplification; it allows us to track the amplification of the wave while it propagates in the axial direction. It should be noted that our linear model cannot be reasonably utilized for $n_i > 7$. Based on experimental measurements, the amplitudes cannot continue to grow exponentially but will rather taper off to a limit cycle value. To mimic this behavior, we use the traditional cut-off value of $n_i = 7$ to suppress unphysical growth.

Figure 5-7 shows this behavior at a tangential wave number of $q = 0$ and $\omega = 70$. In this case there is no tangential fluctuation. In other words, $u_\theta = 0$. Some additional observations may be noted from this graph:

First, the maximum amplitude occurs near the wall. This velocity overshoot near the boundary is known as the Richardson overshoot and is a fundamental characteristic of all oscillatory flows [80,81]. Second, all velocities and pressures have the same shape at a fixed value of q and ω, but their amplification rate changes as they propagate with z. Finally, because of the lack of non-linearity in the existing model, the wave exhibits an

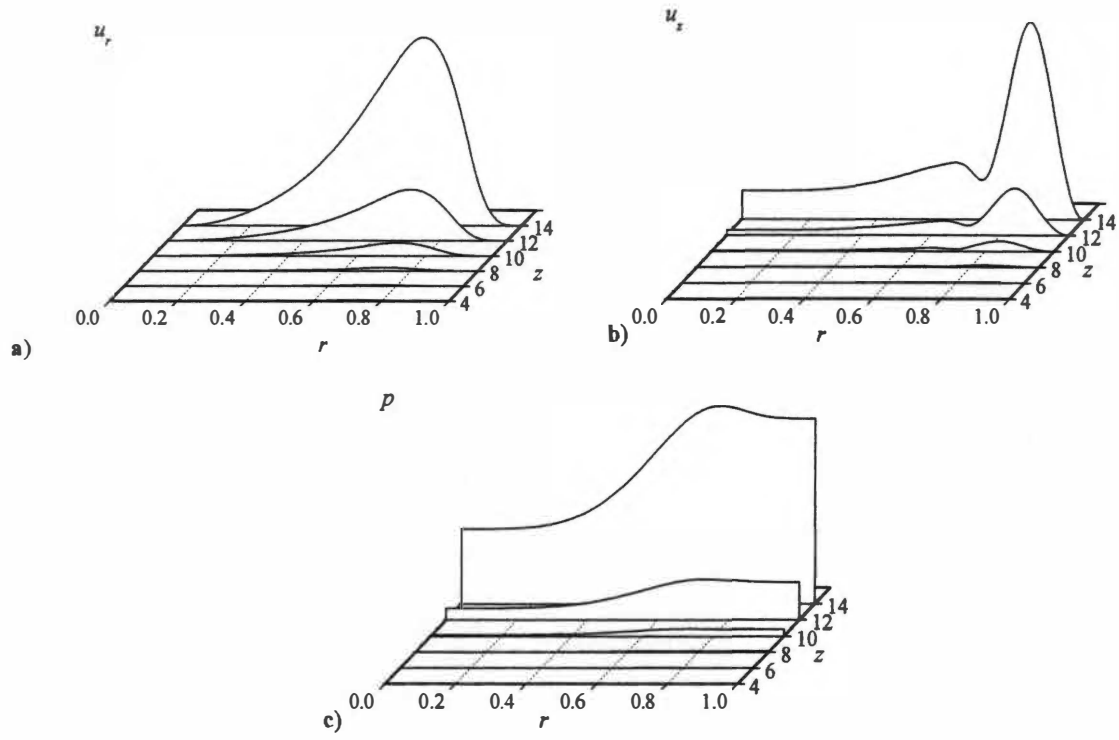

Figure 5-7. Amplification of waves propagating in the axial direction for Re = 5,000, q =0, and ω = 70.

infinite growth rate when z goes to infinity. This problem can only be overcome by adding non-linearity to the model or by suppressing, as we do here, any growth beyond $n_i = 7$.

The same graph is repeated for the first tangential wave number $q = 1$ as shown in Fig. 5-8. Here, a fluctuation in the tangential direction is observed. Generally, the same behavior is detected as in the zeroth tangential mode except for a few differences. First, the amplification rate is higher for the zeroth tangential mode, as confirmed from Fig. 5-2. In addition, the behavior at the centerline is different for this mode. For example, the axial velocity fluctuation u_z at the centerline goes to zero for $q = 1$ as shown in Fig. 5-8c compared to the axial velocity fluctuation in Fig. 5-7b. The same behavior is seen for u_r

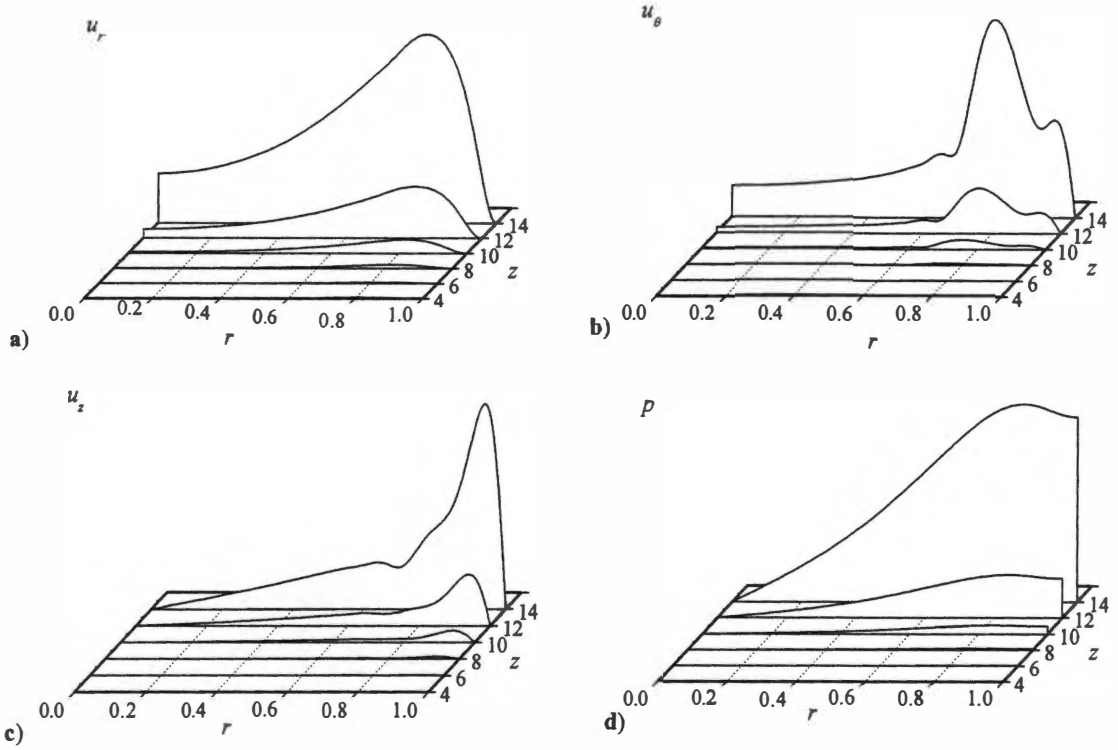

Figure 5-8. Amplification of waves propagating in the axial direction for Re = 5,000 and q =1, and ω = 70.

and p. In fact, this behavior is well explained by Eq. (3.17) which proscribes the boundary conditions of the fluctuating velocities at the centerline. To assess the influence of the headwall injection velocity on the amplitude of the fluctuating quantities, the fluctuating velocities and pressure are plotted for different headwall injection velocities (u_h) in Fig. 5-9. Here, we start with $u_h = 0$ and compare it with different injection values. The graph shows that increasing u_h results in larger amplitudes and reduced motor stability.

It should be noted that, further increases in u_h bring the model to closer agreement with the fundamental assumption of parallel flow under which the normal

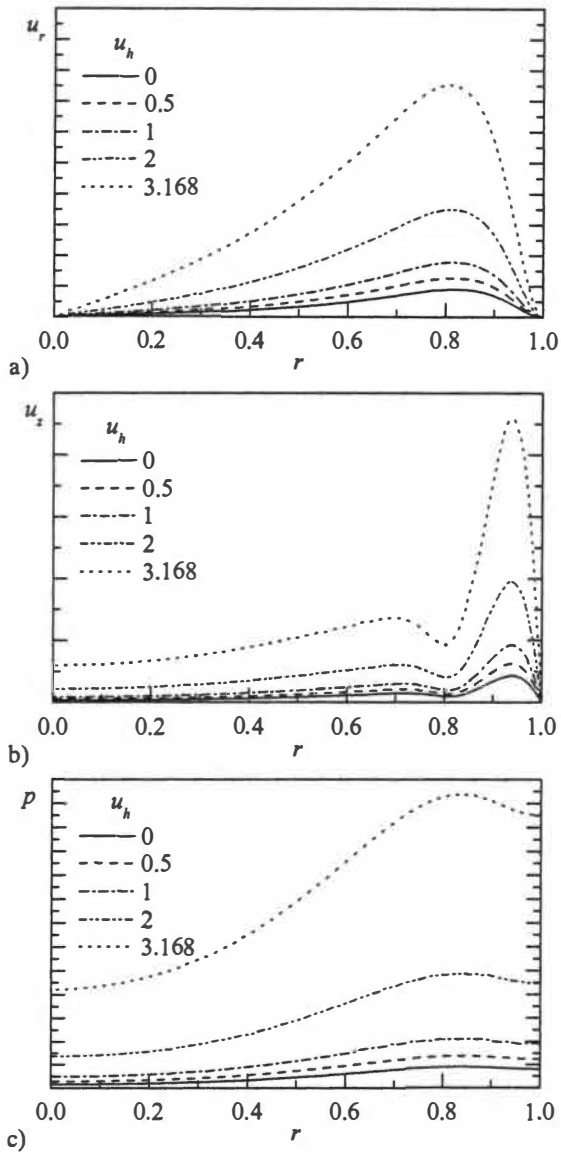

Figure 5-9. Effect of increasing the headwall injection velocity on wave amplitude for Re = 5,000 and q =0, z =8 and ω = 70.

mode paradigm is justified. Another feature in the hybrid model can be inferred from Fig. 5-4. Since the neutral curve is constantly shifted upstream as the injection velocity increases, there comes a point when the neutral curve crosses the vertical line; once this condition is established, the n-factor cannot be calculated because a stable point is needed to start with. A solution to this problem can be sought by implementing a 2-D model that has been presented by Chedevergne, Casalis and Féraille [38] despite the fact that this model was designed to eliminate the inconsistency near the headwall.

To shift our attention to energy considerations, we recall that one essential goal of this project has been to investigate the effect of hydrodynamic instability on the net system amplitude ε used in the combustion instability framework. For a long time, hydrodynamic waves were considered a major source of instability in rockets [18,42,64]. Much research has been conducted in the hydrodynamic field, mainly dealing with parietal vortex shedding. Most of these studies have treated the hydrodynamic waves independently from any other waves. Recently, a connection between hydrodynamic waves and acoustic waves has been developed. This connection is based on scenarios that explain the interaction between two kinds of waves: vortical-acoustic and hydrodynamic. To the best of our knowledge, the only mathematical quantification of the initial triggering of the hydrodynamic instability began with the excellent study by Griffond [45]. In his analysis, he explained the evolution of the hydrodynamic waves as a result of acoustic waves passing over a defect injected area. It should be noted that earlier studies focused on the production of acoustic waves when vortices crossed the exit plane. These studies gave us the idea that there exists a self-loop oscillation between acoustic and hydrodynamic waves. Equation (4.47) represents the contribution of the hydrodynamic

instability from the sidewall on the total net system amplitude. This term can be simplified for different tangential wave numbers as shown in Eqs. (4.65) and (4.67).

As explained before, the effect of vortical-acoustics (see Eq. (4.65)) appears only in the zeroth tangential wave number; this coupling between the two waves vanishes as we move to higher tangential modes. In this work, the influence of hydrodynamic waves will be calculated for four motors: tactical, small, cold flow, and RSRM. The specification of each motor is provided in Table 5-2. The comparison will be based on the first acoustic mode which is the most likely to occur. The first variable that will be discussed is M_b. A first look at Eqs. (4.65) and (4.67) suggests that M_b has an explicit effect on the surface growth rate, which means increasing M_b will increase the instability. In reality, the value of M_b is found to affect the growth rate implicitly and in an unpredictable, nonlinear fashion. This means that the logarithmic wave amplitude n_i, wave number n_r, and the amplitudes are all found to be a function of M_b. The latter variables have a maximum value at a certain M_b. The effect of M_b for the four motor cases are presented in Fig. 5-10 for different initial amplitudes. The maximum growth rates with the associated M_b values are different for each motor. Although each motor in Table 5-2 operates at a prescribed M_b value, we choose to work with wider ranges of

Table 5-2. Physical parameters for the routinely cited cardinal cases [18]

Motor	L (m)	R (m)	$l = L/R$	M_b	δ	k_m	S	ξ	f (Hz)	A_b^r	(m/s)
Small Motor	0.60	0.025	24	1.7^{-3}	5.49^{-4}	1.31^{-1}	77.00	1.0512	1227	2.5	1472
Tactical Rocket	2.03	0.102	~ 20	3.1^{-3}	2.74^{-4}	1.58^{-1}	50.92	0.0628	360	1.2	1462
Cold Flow	1.73	0.051	~ 34	3.3^{-3}	6.07^{-4}	9.26^{-2}	28.07	0.0879	84.0	-2.0[a]	291
RSRM	35.1	0.700	~ 50	2.3^{-3}	1.04^{-4}	6.27^{-2}	27.24	0.0035	19.5	1.0	1369

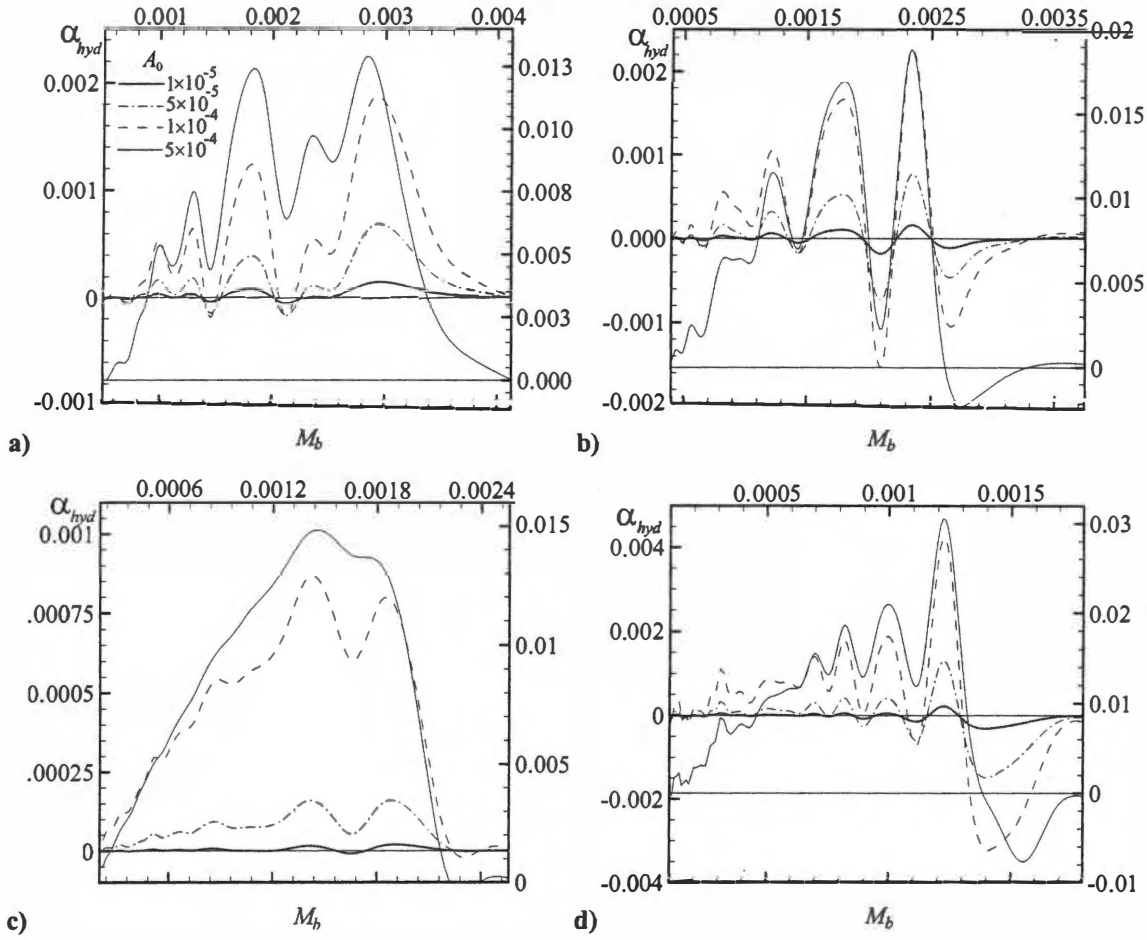

Figure 5-10. Sensitivity of the hydrodynamic instability on the Mach number for different initial amplitudes. In each of these graphs, the solid line corresponds to the initial amplitude obtained using the exit pressure cancellation paradigm.

M_b. It should be noted that the designated M_b values that are used in Table 5-2 for tactical and small motors are close to those that are responsible for triggering the maximum growth rate shown in Figs. 5-10a and 5-10b. Moreover, for the tactical motor, one may detect two critical M_b values that can produce a large hydrodynamic effect. In fact, the first peak in Fig. 5-10a occurs near $M_b \simeq 0.0015$. The second peak arises near 0.00281; however this worst case Mach number is considerably higher than the actual value characteristic of the tactical motor. For the small motor, a worrisome M_b is found at 0.0025. For the other two cases, cold flow and RSRM the peaks are reached at different values than the one posted in Table 5-2. In fact, the M_b values in these two cases are out of the range in which α_{hyd} is damped. The growth rate also increases by increasing the initial amplitude A_0. However, increasing the Mach number does not always induce further increases in instability. For the zeroth tangential mode, the Mach number can have a damping effect. This can be attributed to the nonlinear, unpredictable effect of the Mach number on stability.

For example, one may consider the small motor in Fig. 5-10b with very high initial amplitude; it is hydrodynamically damped at $M_b \cong 0.019$; the same may be said for the RSRM in Fig 5-10d. A damping effect is seen near 0.0013. The other two motors do not depict this behavior. The coupling between vortical-acoustic and hydrodynamic waves has been noted to take place at the zeroth tangential mode. Based on our numerical calculations and available experimental measurements [25], the approximate initial amplitude of $A_0 = 5\times10^{-4}$ is most likely to exist and therefore the four motors are compared in one graph at this particular value. Figure 5-11 describes the difference in

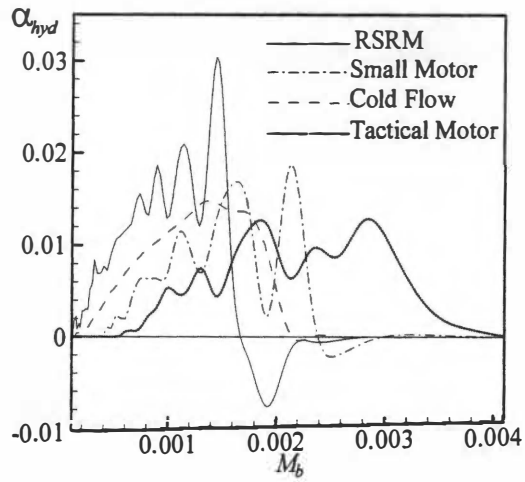

Figure 5-11. Sensitivity of the hydrodynamic instability to the Mach number for the four cases considered in this study. Here $q = 0$ and $A_0 = 5 \times 10^{-4}$.

hydrodynamic stability dependence on the Mach number for each of these four motors. One can see that there is no particular trend or predictable behavior linking the four cases. This observation may be attributed to the fact that each motor has a different aspect ratio and admittance function. Evidently, each of these parameters plays a major role in this investigation. The maximum hydrodynamic effect is for the RSRM, albeit at a different injection Mach number than the one used in reality. For the surface injection used in the RSRM, damping instead of driving is observed. This damping suggests that the RSRM is not susceptible to vortex shedding and/or hydrodynamic instability. Its instability may be linked to other factors that are outside the scope of this investigation. Similarly, the Tactical motor appears to be susceptible to hydrodynamic wave amplification over the broadest range of Mach numbers.

To study the effect of different tangential modes, a small motor with aspect ratio $l = 24$ is picked, and the growth rate for the first three tangential wave numbers is plotted in Fig. 5-12. The three parts in Fig. 5-12 correspond to three increasing initial amplitudes

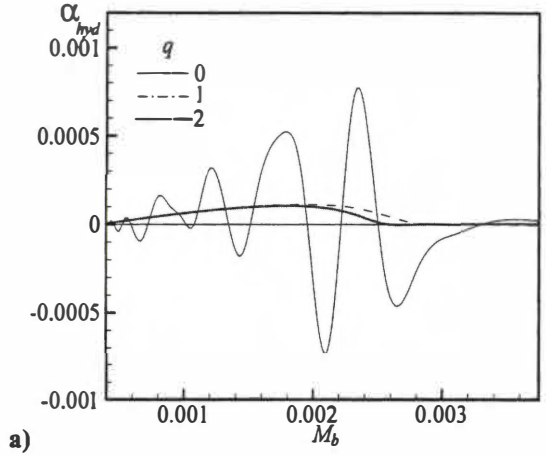

a)

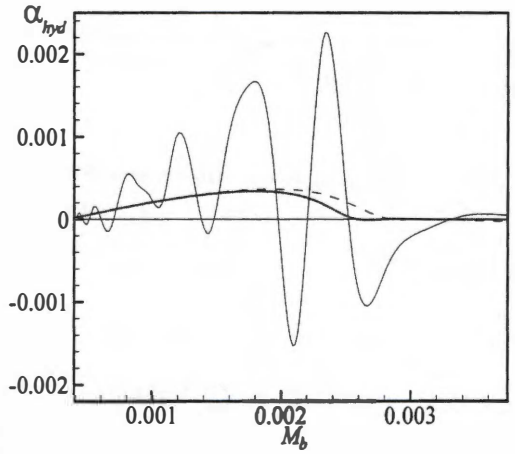

b)

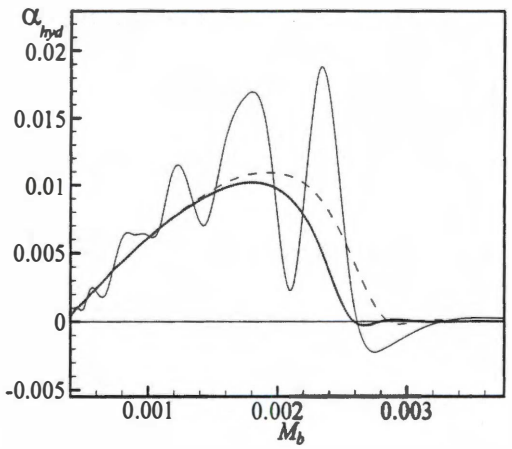

c)

Figure 5-12. Sensitivity of the hydrodynamic instability to the Mach number at the first three tangential wave numbers. Results are shown for a) $A_0 = 5\times10^{-5}$, b) $A_0 = 1\times10^{-4}$, and c) $A_0 = 5\times10^{-4}$.

taken in the practical range observed experimentally and estimated numerically from Eq. (4.75). Clearly, the highest growth rate and oscillations are observed at the zeroth tangential mode. This can be attributed to the strong coupling between the vortical-acoustic waves (described by Majdalani and Flandro [16]) and the hydrodynamic waves (first described by Griffond, Casalis and Pineau [25]). This coupling can be inferred from Eq. (4.65). Departing from $q = 0$ to higher modes eliminates the effect of vortical-acoustic wave coupling. This is clearly seen in Eq. (4.67). By departing further one can notice that the value of M_b where a maximum amplification occurs drifts downstream. For example, the maximum amplification shown in Fig. 5-12 for any initial amplitude at the zeroth tangential mode is at $M_b = 0.0024$. This value becomes 0.002 for $q = 1$, and 0.0018 for $q = 2$. It is also noticed that for the first and second tangential modes and for any initial amplitude, there is a value of M_b after which no effect of hydrodynamic instability may be observed. For this case, $M_b = 0.0026$ at $q = 1$ and 0.0028 at $q = 2$. We suspect similar behavior for all motors at higher tangential modes, $q > 0$. The fact that maximum hydrodynamic amplification occurs at the zeroth tangential wave number is, in summary, attributed to two factors. First, the zeroth tangential eigensolutions by themselves are the most amplified in a purely hydrodynamic instability study. Second, the coupling and energy feedback from the acoustic waves only occur at the zeroth tangential mode. These exacerbating factors lead to the maximum growth rates at $q = 0$.

Another key aspect in this study is the effect of the admittance function A_b^r. This represents the sensitivity of the combustion process to the pressure fluctuation. In fact, A_b^r appears in the surface growth rate expression such as Eq. (4.47). Each motor has a

unique admittance value that can be supplemented experimentally. To study the effect of the admittance function, we allow this value to change in the small motor. This assumption may not be realistic, since the admittance value is a property of the propellant. So, by changing the admittance value, the propellant physical properties are changed. Unlike the injection Mach number, A_b^r seems to have a linear and explicit effect on α_{hyd} as shown in Fig. 5-13. Also confirmed through Eq. (4.65), increasing or decreasing the admittance value will scale up or scale down the growth rate. The effect of admittance disappears at higher tangential modes. This can be explained by realizing that the admittance is an acoustic property and all acoustic effects cancel for $q \geq 1$.

The remaining quantity to be addressed is the energy density given by Eqs. (4.70) and (4.71) for all tangential wave numbers. In the next graph, the energy density as a result of hydrodynamic disturbances is plotted against the Mach number M_b. As in the

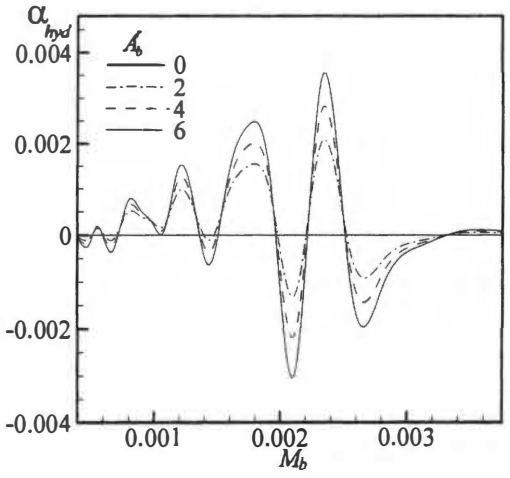

Figure 5-13. Sensitivity of the hydrodynamic instability to the Mach number at several values of the admittance function. Here $q = 0$ and $A_0 = 1\times10^{-4}$.

surface growth rate, the hydrodynamic energy density is found to be sensitive to the injection Mach number for the four cases under consideration. Each motor shown in the graph exhibits its own particular behavior. The energy densities for both the tactical motor in Fig. 5-14a, and the small motor in Fig. 5-14b, reach their peak values near the designated (operational) Mach numbers given in Table 5-2. As for the cold flow experiment and the RSRM, the Mach number where the energy density is maximum is lower than the tabulated value.

The hydrodynamic energy density is much less that the acoustic one, and its maximum contribution is about 4% of the total energy for the tactical motor, 6% for the small motor, 8% for the cold flow experiment, and, finally, 10% for the RSRM. These percentages strictly show that the energy density is a strong function of the aspect ratio l such that, the higher the aspect ratio, the higher the energy density contribution will be.

Figure 5-15 shows the effect of the injection headwall velocity u_h on the instability calculation. In a purely hydrodynamic study, the headwall velocity is found to have an adverse effect on motor stability. The effect of headwall injection velocity on the total net system amplitude ε is more complex to evaluate. The reason is that the headwall injection not only affects the hydrodynamic growth rate σ_i, but also modifies the wave number σ_r; this in turn impacts the net system amplitude calculations due to hydrodynamic disturbances. To show the aftermath, two injection velocities are taken.

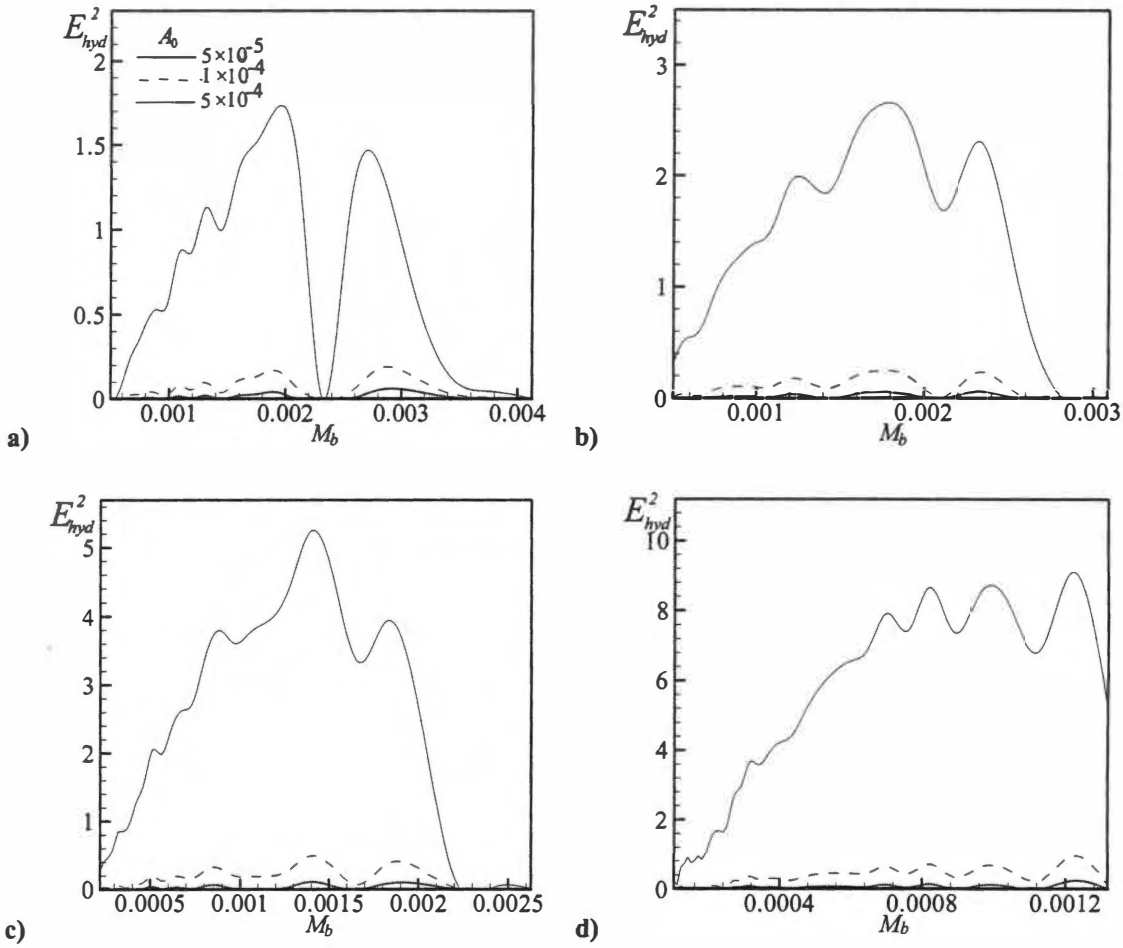

Figure 5-14. Hydrodynamic energy density function versus the Mach number for a) tactical, b) small, c) cold flow experiment, and d) RSRM motors. Results are shown for q = 0 and three different initial disturbance amplitudes.

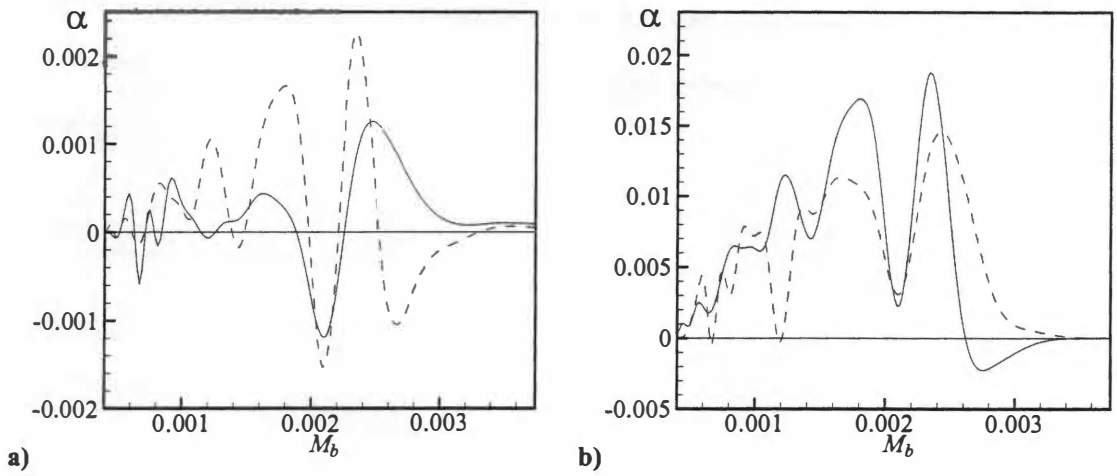

Figure 5-15. Hydrodynamic growth rate effect as function of the Mach number for the solid rocket motor (broken line) and solid rocket motor with headwall injection velocity, $u_h = 0.5$ (solid line). Results are shown for $q = 0$ and a) $A_0 = 1\times10^{-4}$ and b) $A_0 = 5\times10^{-4}$.

First, we use $u_h = 0$ for an SRM with inert headwall, and second, $u_h = 0.5$ for an SRM with reactive headwall. In pure hydrodynamic calculations, it is found that further increases in the headwall velocity results in further instability in the motor. This instability shown in Figs. 5-4 and 5-9 exhibits a nearly linear response to increasing u_h. The case is not the same for the net system amplitude calculations shown in Fig. 5-15. For the first initial amplitude of 10^{-4}, the injection velocity seems to have a damping effect on the total net system amplitude ε. But for a higher initial amplitude, $A_0 = 5\times10^{-4}$, the injection velocity has a driving effect. For the lack of experimental measurements in hybrid rocket motors (or SRMs with headwall injection), further investigations are required to better understand these trends.

To summarize, the growth rate due to hydrodynamic instability is evaluated and compared to the vortical-acoustic growth rate in Table 5-3. For the first two motors (small and tactical) the effect is about 8%, and 7.6% of the total disturbance; these are the

Table 5-3. Hydrodynamic instability contribution versus vortical-acoustic growth rates (sec^{-1}) [82]

Motor	α^*_{hyd}	%	α^*_{vac}	α^*_1	α^*_5	α^*_7
Small Motor	11.870	8.0	148.14	96.1	80.1	-28.06
Tactical Rocket	2.3800	7.6	31.210	-3.55	35.5	-0.744
Cold Flow Experiment	0.6425[a]	0 (4.6)	-35.04(-12.589)	-49.7(-19.4)	15.1(5.7)	-0.442(-0.174)
Space Shuttle RSRM	0.3180[b]	0 (22.4)	2.516(1.417)	-1.08(-0.6102)	3.60(2.03)	-0.00419(-0.0024)

cases where the Mach numbers that produce the largest hydrodynamic amplification are found to be near the designated Mach numbers. For the cold flow experiment and RSRM motor there is no hydrodynamic growth at the designated (operational) Mach numbers. However, if the Mach number is taken at the particular value that triggers maximum hydrodynamic growth, the hydrodynamic amplification in the total growth rate becomes about 4.6% for the cold flow experiment and 22.4% for the RSRM. This reaffirms the importance of retaining these effects in a full combustion instability study.

6. Conclusions and Recommendations

In this investigation we have applied linear spatial theory to characterize the hydrodynamic instability of solid and hybrid rockets with headwall injection. We have determined that headwall injection plays a destabilizing role considering that the range of unstable frequencies is broadened with successive increases in u_h. This is also accompanied by an upstream translation of the critical abscissas and attendant shifting of the neutral curves.

By using the extended Taylor-Culick profile proposed by Majdalani and Vyas [37], we are able to study the effect of headwall injection on stability. By using $u_h = 0.5$, our model is capable of mimicking the core flow in long solid rocket motors with reactive forward closure. Such motors are only slightly more unstable than SRMs with inert headwalls. When u_h is increased to 3.168, the most critical point along the neutral curve (i.e., the tip) is shifted upstream to the extent of reaching the headwall (by contacting the frequency axis). Thus at $z = 0$ and $\omega = 40$ the flow becomes unstable at the injection point. Further increases in u_h cause the concave portion of the neutral curve to fall behind the frequency axis, namely, in the negative z domain. Under such conditions, the flow becomes unstable even at $z = 0$ over an increasing range of frequencies. This range is bracketed by the intersection of the neutral curve and the frequency axis. The forward truncation of the neutral curve prevents us from calculating the amplification n-factor at that frequency; at that point the e^n model becomes incapable of predicting the wave amplification because it requires an initial stable point.

Another goal of this investigation has been to study the effect of hydrodynamic waves on the net system amplitude ε defined in the combustion instability work. As explained in the literature, the measuring of the hydrodynamic effect in real firing is nearly impossible. The other way to account for the hydrodynamic effect is to investigate its impact on the net system amplitude.

Experimental measurements suggest that the controlling lock-in frequency is the acoustic frequency. This means that, if an acoustic frequency exists, all other frequencies die out except for the one that matches the acoustic frequency. Based on this assumption, the first acoustic mode is considered as the dominant one. In the present framework, the hydrodynamic part is recast in harmony with the combustion instability formulation with the first acoustic mode as the driving frequency. The superposition of hydrodynamic waves on vortical-acoustic waves is made possible due to their dissimilar propagation speeds and wavelengths. The formulation of the problem shows that the hydrodynamic effect depends on several variables: tangential wave number q, injection Mach number M_b, admittance function A_b^r and, finally, headwall injection velocity u_h.

First, we find that the coupling between hydrodynamic waves and vortical-acoustic waves happens only at the zeroth tangential wave number $q = 0$. Following that, the acoustic waves give rise to new terms which have adverse or favorable effects on the net system amplitude ε based on the injection Mach number M_b. The acoustic effect no longer exists as we move up to $q \geq 1$.

The second factor is the injection Mach number M_b. This factor, perhaps, has the most influence on the net system amplitude. A pure hydrodynamic study does not show

the effect of the Mach number on the instability calculation. This can be attributed to the previous lack of understanding of the connection between hydrodynamic instability and combustion instability. In hydrodynamic analysis, the fluctuating velocities are normalized by the wall injection speed U_w and the pressure disturbance is normalized by the hydrodynamic pressure $\rho_0 U_w^2$ as shown in Eq. (4.35). According to this normalization, the physical frequency is defined as $\omega_r U_w/(2\pi R)$. Here the hydrodynamic amplification is based on the dimensionless frequency ω_r (Figs. 5.1-5.5). As a result, the effect of M_b cannot be seen. Analysis of this form can be confusing because it deals with an infinite number of dimensionless frequencies that have no physical meaning. On the other hand, if Eq. (4.36) is used (which is based on the speed of sound normalization), the physical frequency becomes $k_m a_0/(2\pi R)$. In this case, k_m can represent any of the fundamental or harmonic acoustic modes. By assuming oscillations at the first fundamental acoustic mode, Figs. 5.1-5.5 can be based now on M_b instead of ω_r and therefore the effect of M_b can be seen more clearly. In actuality, this relation supports experimental measurements which appear to indicate that M_b plays a major role [43,44] and thereby suggest the need to combine hydrodynamic and combustion instability interactions in one model. In our investigation, we demonstrate that M_b not only has an explicit effect, but also an implicit one. This probably is one of the most profound conclusions that we achieved in this investigation. To study the effect of M_b, four different motors are used with different M_b, and different aspect ratios l (as shown in Table 5-2) where the first acoustic mode is implemented in all four cases. Accordingly, a

wide range of M_b is used and the hydrodynamic growth rate is plotted. For tactical and small motors, the designated M_b in Table 5-2 happens to be very close to the one that causes maximum amplification. On the other hand, for RSRM (Redesigned Shuttle Rocket Motor) and cold flow experiments, the value of M_b where the effect of hydrodynamic growth reaches its maximum value is less than the designated Mach number. The actual M_b for these two cases has a damping effect. For a moment, if we assume that the RSRM case operates at $M_b = 0.0013$ instead of 0.0037, the acoustic instability contribution decreases but the hydrodynamic amplification increases to 22.4% of the total amplification. This proves that hydrodynamic instability is stronger in long motors when they operate in the range of Mach numbers that triggers hydrodynamic amplification.

The admittance function A_b^r also plays a role in the hydrodynamic calculation. In this analysis we find that the effect of A_b^r is just an explicit one. This implies that A_b^r cannot control the amplification of the hydrodynamic wave as in the case of M_b. Its effect is not as strong as the injection Mach number's. As for the nozzle exit damping, it has not been calculated in this study. This is partly due to the lack of a compressible model near the nozzle and partly due to the possibility for the nozzle to play a driving role in sustaining and promoting hydrodynamic wave amplification.

As far as the headwall injection velocity effect u_h is concerned, we could not characterize it fully. This can be attributed to the following reasons. First, there are no experimental results that verify our findings for any headwall injection velocity. This limits us to work most of the energy calculations in solid rocket motors. Second, by

exceeding a certain headwall injection velocity $(u_h > 3.168)$, the e^n model becomes invalid at one frequency or alternatively at one Mach number in the combustion instability framework.

Finally, it is found that the injection velocity in the range of $0 < u_h < 3.168$ does not just affect the amplification rate σ_i, but also modifies the wave number σ_r. This, in turn, alters the behavior of the α_{hyd} at different M_b compared to a solid rocket motor.

To complete our investigation, the hydrodynamic energy density is calculated for four cases, and its contribution to the total acoustic energy is found to vary between 4 and 10%. This contribution increases by increasing the aspect ratio.

For future work, it is clear that, first and foremost, a full nonlinear hydrodynamic instability model is needed to replace the crude nonlinear model used here (specifically, the one that consists of clipping the logarithmic growth rate at the threshold of nonlinear behavior). Such a nonlinear model could allow us to precisely predict the limit cycle and maximum amplitude that the wave can reach; it could also provide a better estimate of the initial wave amplitude A_0. Second, experimental measurements [43,44] have suggested that the second or the third acoustic modes can be triggered when changing the injection Mach number. A model to predict the relation between the injection Mach number and the excited mode could be very useful. Third, although the self-loop oscillation scenario between hydrodynamic instability and acoustic instability by Griffond [45] fits the experimental results to a certain extent, a need for a model that can accurately predict the initiation of the hydrodynamic wave amplitude is required. Finally,

adding compressibility effects, especially near the nozzle, could make it possible to predict the effect of nozzle flow on the total system amplitude.

References

References

[1] Brownlee, W. G., "An Experimental Investigation of Unstable Combustion in Solid Propellant Rocket Motors," Ph.D. Dissertation, California Institute of Technology, 1959.

[2] Flandro, G. A., "Rotating Flows in Acoustically Unstable Rocket Motors," Dissertation, California Institute of Technology, 1967.

[3] Flandro, G. A., Fischbach, S. R., Majdalani, J., and French, J. C., "Nonlinear Rocket Motor Stability Prediction: Limit Amplitude, Triggering, and Mean Pressure Shift," AIAA Paper 2004-4054, July 2004.

[4] Crocco, L., and Cheng, S. I., "High Frequency Combustion Instability in Rocket Motors with Concentrated Combustion," *Journal of the American Rocket Society,* Vol. 23, No. September-October, 1953, pp. 301-313.

[5] Crocco, L., and Cheng, S. I., "Theory of Combustion Instability in Liquid Propellant Rocket Motors," *AGARD*, Vol. 8, Butterworths Sci. Pub. Ltd, London, UK, 1956.

[6] Hart, R. W., and McClure, F. T., "Theory of Acoustic Instability in Solid Propellant Rocket Combustion," *Tenth Symposium (International) on Combustion*, 1964, pp. 1047-1066.

[7] Culick, F. E. C., "Acoustic Oscillations in Solid Propellant Rocket Chambers," *Acta Astronautica,* Vol. 12, No. 2, 1966, pp. 113-126.

[8] Culick, F. E. C., "Interactions between the Flow Field, Combustion and Wave Motions in Rocket Motors," 1972.

[9] Culick, F. E. C., "The Stability of One-Dimensional Motions in a Rocket Motor," *Combustion Science and Technology,* Vol. 7, No. 4, 1973, pp. 165-175.

[10] Culick, F. E. C., "Stability of Three-Dimensional Motions in a Rocket Motor," *Combustion Science and Technology,* Vol. 10, No. 3, 1974, pp. 109-124.

[11] Flandro, G. A., "Effects of Vorticity on Rocket Combustion Stability," *Journal of Propulsion and Power,* Vol. 11, No. 4, 1995, pp. 607-625.

[12] Flandro, G. A., "On Flow Turning," AIAA Paper 95-2530, July 1995.

[13] Majdalani, J., and Van Moorhem, W. K., "A Multiple-Scales Solution to the Acoustic Boundary Layer in Solid Rocket Motors," *Journal of Propulsion and Power,* Vol. 13, No. 2, 1997, pp. 186-193.

[14] Majdalani, J., and Van Moorhem, W. K., "Improved Time-Dependent Flowfield Solution for Solid Rocket Motors," AIAA Paper 97-2717, July 1997.

[15] Majdalani, J., and Van Moorhem, W. K., "Improved Time-Dependent Flowfield Solution for Solid Rocket Motors," *AIAA Journal,* Vol. 36, No. 2, 1998, pp. 241-248.

[16] Majdalani, J., and Flandro, G. A., "The Oscillatory Pipe Flow with Arbitrary Wall Injection," *Proceedings of the Royal Society, Series A,* Vol. 458, No. 2022, 2002, pp. 1621-1651.

[17] Flandro, G. A., and Majdalani, J., "Aeroacoustic Instability in Rockets," AIAA Paper 2001-3868, July 2001.

[18] Flandro, G. A., and Majdalani, J., "Aeroacoustic Instability in Rockets," *AIAA Journal,* Vol. 41, No. 3, 2003, pp. 485-497.

[19] Culick, F. E. C., "Stability of Longitudinal Oscillations with Pressure and Velocity Coupling in a Solid Propellant Rocket," *Combustion Science and Technology,* Vol. 2, No. 4, 1970, pp. 179-201.

[20] Flandro, G. A., Majdalani, J., and French, J. C., "Incorporation of Nonlinear Capabilities in the Standard Stability Prediction Program," AIAA Paper 2004-4182, July 2004.

[21] Fischbach, S. R., Flandro, G. A., and Majdalani, J., "Volume-to-Surface Transformations of Rocket Stability Integrals," AIAA Paper 2004-4053, July 2004.

[22] Fischbach, S. R., Majdalani, J., and Flandro, G. A., "Acoustic Instability of the Slab Rocket Motor," AIAA Paper 2004-4061, July 2004.

[23] Fischbach, S. R., Majdalani, J., and Flandro, G. A., "Verification and Validation of Rocket Stability Integral Transformations," AIAA Paper 2005-4001, July 2005.

[24] Casalis, G., Avalon, G., and Pineau, J.-P., "Spatial Instability of Planar Channel Flow with Fluid Injection through Porous Walls," *Physics of Fluids,* Vol. 10, No. 10, 1998, pp. 2558-2568.

[25] Griffond, J., Casalis, G., and Pineau, J.-P., "Spatial Instability of Flow in a Semiinfinite Cylinder with Fluid Injection through Its Porous Walls," *European Journal of Mechanics B/Fluids,* Vol. 19, No. 1, 2000, pp. 69-87.

[26] Griffond, J., and Casalis, G., "On the Nonparallel Stability of the Injection Induced Two-Dimensional Taylor Flow," *Physics of Fluids,* Vol. 13, No. 6, 2001, pp. 1635-1644.

[27] Griffond, J., and Casalis, G., "On the Dependence on the Formulation of Some Nonparallel Stability Approaches Applied to the Taylor Flow," *Physics of Fluids,* Vol. 12, No. 2, 2000, pp. 466-468.

[28] Ugurtas, B., Avalon, G., Lupoglazoff, N., Vuillot, F., and Casalis, G., "Stability and Acoustic Resonance of Internal Flows Generated by Side Injection," *Solid Propellant Chemistry, Combustion, and Motor Interior Ballistics*, Vol. 185, edited by V. Yang, T. B. Brill, and W.-Z. Ren, AIAA Progress in Astronautics and Aeronautics, Washington, DC, 2000, pp. 823-836.

[29] Ugurtas, B., Avalon, G., Lupoglazoff, N., and Vuillot, F., "Numerical Computations of Hydrodynamic Instabilities inside Channels with Wall Injection," AIAA Paper 99-2505, June 1999.

[30] Taylor, G. I., "Fluid Flow in Regions Bounded by Porous Surfaces," *Proceedings of the Royal Society, London, Series A,* Vol. 234, No. 1199, 1956, pp. 456-475.

[31] Culick, F. E. C., "Rotational Axisymmetric Mean Flow and Damping of Acoustic Waves in a Solid Propellant Rocket," *AIAA Journal,* Vol. 4, No. 8, 1966, pp. 1462-1464.

[32] Avalon, G., Casalis, G., and Griffond, J., "Flow Instabilities and Acoustic Resonance of Channels with Wall Injection," AIAA Paper 98-3218, July 1998.

[33] Berman, A. S., "Laminar Flow in Channels with Porous Walls," *Journal of Applied Physics,* Vol. 24, No. 9, 1953, pp. 1232-1235.

[34] Varapaev, V. N., and Yagodkin, V. I., "Flow Stability in a Channel with Porous Walls," *Fluid Dynamics (Izvestiya Akademii Nauk SSSR, Meckanika Zhidkosti i Gaza),* Vol. 4, No. 5, 1969, pp. 91-95.

[35] Beddini, R. A., and Roberts, T. A., "Turbularization of an Acoustic Boundary Layer on a Transpiring Surface," *AIAA Journal,* Vol. 26, No. 8, 1988, pp. 917-923.

[36] Beddini, R. A., "Injection-Induced Flows in Porous-Walled Ducts," *AIAA Journal,* Vol. 24, No. 11, 1986, pp. 1766-1773.

[37] Majdalani, J., and Vyas, A. B., "Inviscid Models of the Classic Hybrid Rocket," AIAA Paper 2004-3474, July 2004.

[38] Chedevergne, F., Casalis, G., and Féraille, T., "Biglobal Linear Stability Analysis of the Flow Induced by Wall Injection," *Physics of Fluids,* Vol. 18, No. 1, 2006, pp. 014103-14.

[39] Herbert, T., "Parabolized Stability Equations," *Annual Review of Fluid Mechanics,* Vol. 29, 1997, pp. 245-283.

[40] Bertolotti, F. P., "Nonlinear Analysis of Boundary Layers with Streamwise Varying Properties," NASA Glenn, Annual Rept. NASA Training Grant NGT 50259, Columbus, OH, August 1989.

[41] Flandro, G. A., "Vortex Generated Sound in Cavities," AIAA Paper 1973-1014, October 1973.

[42] Flandro, G. A., "Vortex Driving Mechanisms in Oscillatory Rocket Flows," *Journal of Propulsion and Power,* Vol. 2, No. 3, 1986, pp. 206-214.

[43] Dunlap, R., Sabnis, J. S., Beddini, R. A., Flandro, G. A., Brown, R. S., Gibeling, H. J., Blackner, A. M., Waugh, R. C., and McDonald, H., "Internal Flow Field Investigation," U. S. Air Force Rocket Propulsion Laboratory, TR-85-079, August 1985.

[44] Dunlap, R., Willoughby, P. G., and Hermsen, R. W., "Flowfield in the Combustion Chamber of a Solid Propellant Rocket Motor," *AIAA Journal,* Vol. 12, No. 10, 1974, pp. 1440-1445.

[45] Griffond, J., "Receptivity and Aeroacoustic Resonance in Channels with Blowing Walls," *The Physics of Fluids,* Vol. 14, No. 11, 2002, pp. 3946-3962.

[46] Venugopal, P., "Direct Numerical Simulation of Turbulence in a Model Solid Rocket Motor," Ph.D. Dissertation, University of Illinois at Urbana-Champaign, 2003.

[47] Majdalani, J., and Van Moorhem, W. K., "Laminar Cold-Flow Model for the Internal Gas Dynamics of a Slab Rocket Motor," *Journal of Aerospace Science and Technology,* Vol. 5, No. 3, 2001, pp. 193-207.

[48] Majdalani, J., Vyas, A. B., and Flandro, G. A., "Higher Mean-Flow Approximation for a Solid Rocket Motor with Radially Regressing Walls," AIAA Paper 2001-3870, July 2001.

[49] Majdalani, J., Vyas, A. B., and Flandro, G. A., "Higher Mean-Flow Approximation for a Solid Rocket Motor with Radially Regressing Walls," *AIAA Journal,* Vol. 40, No. 9, 2002, pp. 1780-1788.

[50] Majdalani, J., and Zhou, C., "Moderate-to-Large Injection and Suction Driven Channel Flows with Expanding or Contracting Walls," *Journal of Applied Mathematics and Mechanics,* Vol. 83, No. 3, 2003, pp. 181-196.

[51] Majdalani, J., "The Taylor-Culick Profile with Uniform Headwall Injection," AIAA Paper 2005-4534, July 2005.

[52] Malik, M. R., "Numerical Methods for Hypersonic Boundary Layer Stability," *Journal of Computational Physics,* Vol. 86, No. 2, 1990, pp. 376-413.

[53] Don, W. S., and Solomonoff, A., "A Boundary Value Problem with Multiple Solutions from the Theory of Laminar Flow," *SIAM Journal on Scientific Computing,* Vol. 16, No. 6, 1995, pp. 1253-1268.

[54] Abu-Irshaid, E. M., Majdalani, J., and Casalis, G., "Hydrodynamic Instability of the Bidirectional Vortex," AIAA Paper 2005-4531, July 2005.

[55] Majdalani, J., "The Compressible Taylor-Culick Flow," AIAA Paper 2005-3542, July 2005.

[56] Brown, R. S., Dunlap, R., Young, S. W., and Waugh, R. C., "Vortex Shedding as a Source of Acoustic Energy in Segmented Solid Rockets," *Journal of Spacecraft and Rockets,* Vol. 18, No. 4, 1981, pp. 312-319.

[57] Lupoglazoff, N., and Vuillot, F., "Parietal Vortex Shedding as a Cause of Instability for Long Solid Propellant Motors. Numerical Simulations and Comparisons with Firing Tests," AIAA Paper 96-0761, January 1996.

[58] Lupoglazoff, N., and Vuillot, F., "Numerical Simulation of Vortex Shedding Phenomenon in Two-Dimensional Test Case Solid Rocket Motors," AIAA Paper 92-0776, January 1992.

[59] Dupays, J., Prévost, M., Tarrin, P., and Vuillot, F., "Effects of Particulate Phase on Vortex Shedding Driven Oscillations in Solid Rocket Motors," AIAA Paper 96-3248, July 1996.

[60] Traineau, J. C., Prévost, M., and Lupoglazoff, N., "A Subscale Test Program to Assess the Vortex Shedding Driven Instabilities in Segmented Solid Rocket Motors," AIAA Paper 97-3247, July 1997.

[61] Dotson, K. W., Koshigoe, S., and Pace, K. K., "Vortex Shedding in a Large Solid Rocket Motor without Inhibitors at the Segment Interfaces," *Journal of Propulsion and Power,* Vol. 13, No. 2, 1997, pp. 197-206.

[62] Tissier, P. Y., Godfroy, F., and Jacquemin, P., "CFD Analysis of Vortex Shedding inside a Subscale Segmented Motor," AIAA Paper 94-2781, June 1994.

[63] Morfouace, V., and Tissier, P. Y., "Two-Phase Flow Analysis of Instabilities Driven by Vortex Shedding in Solid Rocket Motors," AIAA Paper 95-2733, July 1995.

[64] Vuillot, F., "Vortex-Shedding Phenomena in Solid Rocket Motors," *Journal of Propulsion and Power,* Vol. 11, No. 4, 1995, pp. 626-639.

[65] Vuillot, F., and Lupoglazoff, N., "Parietal Vortex Shedding as a Source of Instability for Long Solid Propellan Motors. Numerical Simulation and Comparisons with Firing Tests," 34th Aerospace Siences Meeting and Exhibit AIAA 1996.

[66] Flandro, G. A., Majdalani, J., and Sims, J. D., "Nonlinear Longitudinal Mode Instability in Liquid Propellant Rocket Engine Preburners," AIAA Paper 2004-4162, July 2004.

[67] Flandro, G. A., Majdalani, J., and Sims, J. D., "On Nonlinear Combustion Instability in Liquid Propellant Rocket Engines," AIAA Paper 2004-3516, July 2004.

[68] Majdalani, J., "Characterization of the Laminar Boundary Layer in Solid Rocket Motors," AIAA Paper 98-3699, July 1998.

[69] Majdalani, J., "The Boundary Layer Structure in Cylindrical Rocket Motors," *AIAA Journal,* Vol. 37, No. 4, 1999, pp. 505-508.

[70] Majdalani, J., Fischbach, S. R., and Flandro, G. A., "Improved Energy Normalization Function in Rocket Motor Stability Calculations," *Journal of Aerospace Science and Technology,* Vol. 10, No. 6, 2006, pp. 495-500.

[71] Culick, F. E. C., "Calculation of the Admittance Function for a Burning Surface," *Astronautica Acta,* Vol. 13, 1967, pp. 221-237.

[72] Culick, F. E. C., "A Review of Calculations for Unsteady Burning of a Solid Propellant.," *AIAA Journal,* Vol. 6, No. 12, 1968, pp. 2241-2254.

[73] Ugurtas, B., "Etudes Numérique Et Expérimentale Des Instabilités Hydrodynamiques Et Du Couplage Aéro-Acoustique Dans Un Ecoulement De Taylor," Ph.D. Dissertation, University of Paris, 6, 2000.

[74] Howe, M. S., "The Dissipation of Sound at Sharp Edges," AIAA Paper 1980-972 June 4-6 1980.

[75] Howe, M. S., "The Dissipation of Sound at an Edge," *Journal of Sound and Vibration,* Vol. 70, No. 6, 1980, pp. 407-411.

[76] Dunlap, R., Blackner, A. M., Waugh, R. C., Brown, R. S., and Willoughby, P. G., "Internal Flow Field Studies in a Simulated Cylindrical Port Rocket Chamber," *Journal of Propulsion and Power,* Vol. 6, No. 6, 1990, pp. 690-704.

[77] Hoffman, J. D., *Numerical Methods for Engineers and Scientists*, 2nd ed., Marcel Dekker, New York, 1992.

[78] Abu-Irshaid, E. M., Majdalani, J., and Casalis, G., "Stability of Rockets with Headwall Injection," AIAA Paper 2005-3543, July 2005.

[79] Gaster, M., "On the Effects of Boundary-Layer Growth on Flow Stability," *Journal of Fluid Mechanics,* Vol. 66, No. 3, 1974, pp. 465-480.

[80] Richardson, E. G., "The Amplitude of Sound Waves in Resonators," *Proceedings of the Physical Society, London,* Vol. 40, No. 27, 1928, pp. 206-220.

[81] Richardson, E. G., and Tyler, E., "The Transverse Velocity Gradient near the Mouths of Pipes in Which an Alternating or Continuous Flow of Air Is Established," *Proceedings of the Royal Society, London, Series A,* Vol. 42, No. 1, 1929, pp. 1-15.

[82] Majdalani, J., Flandro, G. A., and Fischbach, S. R., "Some Rotational Corrections to the Acoustic Energy Equation in Injection-Driven Enclosures," *Physics of Fluids,* Vol. 17, No. 7, 2005, pp. 07410201-20.

Appendix

A. Dispersion Relation

The coefficient matrix in the dispersion relation in given by:

$$[\mathbf{C}]=\begin{pmatrix} C_{11} & C_{12} & 0 & C_{14} & 0 & 0 \\ 0 & C_{21} & 0 & 0 & 0 & 0 \\ C_{31} & C_{32} & C_{33} & 0 & 0 & C_{36} \\ 0 & 0 & 0 & C_{45} & 0 & 0 \\ C_{51} & 0 & 0 & C_{54} & C_{55} & C_{56} \\ C_{61} & C_{62} & C_{63} & C_{64} & C_{65} & 0 \end{pmatrix} \tag{A.1}$$

where

$$\begin{cases} C_{11}=-\dfrac{1}{r}\ ,\ C_{12}=-\dfrac{iq}{r}\ ,\ C_{14}=-i\sigma, C_{21}=1 \\ C_{31}=-\dfrac{2iq}{r^2},\ C_{32}=Re\left(-i\omega+\dfrac{U_r}{r}+i\sigma U_z\right)+\dfrac{1}{r^2}\left(q^2+1\right)+\sigma^2, \\ C_{33}=ReU_r-\dfrac{1}{r}, C_{36}=Re\dfrac{iq}{r} C_{45}=1, \\ C_{51}=ReU_z',\ C_{54}=Re\left(-i\omega+i\sigma U_z+\dfrac{\partial U_z}{\partial z}\right)+\dfrac{q^2}{r^2}+\sigma^2, \\ C_{55}=ReU_r-\dfrac{1}{r},\ C_{56}=Re\dfrac{iq}{r} \\ C_{61}=\dfrac{1}{Re}\left(-\dfrac{q^2}{r^2}-\sigma^2\right)+i\omega+\dfrac{U_r}{r}-U_r'-i\sigma U_z, \\ C_{62}=\dfrac{1}{Re}\left(-\dfrac{iq}{r^2}\right)+U_r\dfrac{iq}{r},\ C_{63}=\dfrac{1}{Re}\left(-\dfrac{iq}{r}\right), C_{64}=i\sigma U_r,\ C_{65}=\dfrac{1}{Re}(-i\sigma) \end{cases} \tag{A.2}$$

Discretization of the disturbed system is based on a spectral collocation method [53]. Accordingly, we define $\xi=2r-1\in[-1,1]$ and choose T_N to be the Nth-order Chebyshev polynomial. The $N+1$ collocation points are:

$$\xi_i=\cos\left(\frac{\pi i}{N}\right)\quad i=0,...,N \tag{A.3}$$

Equation (A.3) enables us to calculate the so-called Gauss-Lobatto points. Subsequently, the amplitude function ψ can be interpolated using the polynomial form $\psi(\xi)=\sum \lambda_i \psi(\xi_i)$, where λ_i denotes a Lagrangian multiplier

$$\lambda_i(\xi)=\left(\frac{1-\xi_i^2}{\xi-\xi_i}\right)(-1)^{i+1}\frac{T_N'}{N^2 c_i} \tag{A.4}$$

Here T_N' is the derivative of Nth Chebyshev polynomial. The $N+1$ discrete values of $\psi_i=\psi(\xi_i)$ are originally unknown. Their accuracy depends on the size of N. As ψ is a solution of a differential problem, a tacit relation can be obtained between the derivative ψ' and ψ itself. After some algebra, one finds

$$\begin{cases} D_{ik}=\dfrac{c_i}{c_k}\dfrac{(-1)^{k+i}}{(\xi_i-\xi_k)}; & i\neq k \\ D_{ii}=-\dfrac{\xi_i}{2(1-\xi_i^2)}; & i=1,\ldots,N-1 \\ D_{00}=-D_{NN}=\dfrac{2N^2+1}{6} \end{cases} \tag{A.5}$$

where $c_0=c_N=2$, $c_i=1$, $i=1,\ldots,N-1$ and the discretized equations can be written as

$$\frac{\mathrm{d}\psi}{\mathrm{d}\xi}(\xi_i)=\sum_{k=0}^{N} D_{ik}\psi_k \tag{A.6}$$

where ψ represents the amplitude components, namely, $\psi=(u_r,u_\theta,u_z,p)$.

B. Energy Formulation

In what follows the steps leading to the linear growth rate expression in the combustion instability framework are presented. The analysis begins by considering the temporal rate of change of the energy density defined in the Dissertation as Eq. (4.16).

$$\frac{\partial \mathscr{E}}{\partial t} = -\nabla\cdot\left\{\rho V\left[\frac{T}{\gamma(\gamma-1)}+\tfrac{1}{2}V\cdot V\right]\right\}+\left\{\begin{array}{l} -\dfrac{1}{\gamma}\nabla\cdot(pV)+\rho V\cdot(V\times\omega) \\ +\delta^2\left[\omega\cdot\omega-V\cdot(\nabla\times\omega)\right]+\dfrac{\delta^2}{(\gamma-1)Pr}\nabla^2 T \\ +\delta_d^2\left[(\nabla\cdot V)^2+V\cdot\nabla(\nabla\cdot V)\right]+\dot{Q}+V\cdot F \end{array}\right\} \quad \text{(B.1)}$$

where $\mathscr{E}$ represents the total energy density, that can be separated into steady and unsteady parts

$$\mathscr{E} = \bar{\mathscr{E}} + \mathscr{E}' = \frac{\rho T}{\gamma(\gamma-1)}+\tfrac{1}{2}\rho V\cdot V \quad \text{(B.2)}$$

Expanding the second term of Eq. (B.2) and collecting like terms gives:

$$\tfrac{1}{2}\rho V\cdot V = \tfrac{1}{2}\bar{\rho}\bar{M}_b^2 U\cdot U$$

$$+\tfrac{1}{2}\left(2\bar{M}_b\bar{\rho}U\cdot u^{(1)}+\bar{\rho}u^{(1)}\cdot u^{(1)}+\bar{M}_b^2\rho^{(1)}U\cdot U+2\bar{M}_b\rho^{(1)}U\cdot u^{(1)}+\rho^{(1)}u^{(1)}\cdot u^{(1)}\right) \quad \text{(B.3)}$$

The equation of state and Eq. (4.8) can be used to produce

$$\left(\bar{P}+p^{(1)}\right)=\left(\bar{\rho}+\rho^{(1)}\right)\left(\bar{T}+T^{(1)}\right)=\bar{\rho}\bar{T}+\left(\bar{T}\rho^{(1)}+\bar{\rho}T^{(1)}\right)+\left(\rho^{(1)}T^{(1)}\right) \quad \text{(B.4)}$$

$$\begin{cases}\bar{P}=\bar{\rho}\bar{T} \\ p^{(1)}=\left(\bar{T}\rho^{(1)}+\bar{\rho}T^{(1)}\right)+\left(\rho^{(1)}T^{(1)}\right)\end{cases} \quad \text{(B.5)}$$

This result can be substituted into Eq. (B.4) and Eq. (B.2) to yield

$$\mathscr{E}=\frac{1}{\gamma(\gamma-1)}\left[\bar{\rho}\bar{T}+\left(\bar{T}\rho^{(1)}+\bar{\rho}T^{(1)}\right)+\left(\rho^{(1)}T^{(1)}\right)\right]+\tfrac{1}{2}\bar{\rho}\bar{M}_b^2\boldsymbol{U}\cdot\boldsymbol{U}$$

$$+\tfrac{1}{2}\left(2\bar{M}_b\bar{\rho}\boldsymbol{U}\cdot\boldsymbol{u}^{(1)}+\bar{\rho}\boldsymbol{u}^{(1)}\cdot\boldsymbol{u}^{(1)}+\bar{M}_b^2\rho^{(1)}\boldsymbol{U}\cdot\boldsymbol{U}+2\bar{M}_b\rho^{(1)}\boldsymbol{U}\cdot\boldsymbol{u}^{(1)}+\rho^{(1)}\boldsymbol{u}^{(1)}\cdot\boldsymbol{u}^{(1)}\right) \quad \text{(B.6)}$$

The unsteady part of the energy density can be represented as:

$$\mathscr{E}'=\left[\frac{\left(\bar{T}\rho^{(1)}+\bar{\rho}T^{(1)}\right)}{\gamma(\gamma-1)}+\bar{\rho}\bar{M}_b\boldsymbol{U}\cdot\boldsymbol{u}^{(1)}+\tfrac{1}{2}\bar{M}_b^2\rho^{(1)}\boldsymbol{U}\cdot\boldsymbol{U}\right]_1$$

$$+\left[\frac{\rho^{(1)}T^{(1)}}{\gamma(\gamma-1)}+\rho^{(1)}\bar{M}_b\boldsymbol{U}\cdot\boldsymbol{u}^{(1)}+\tfrac{1}{2}\bar{\rho}\boldsymbol{u}^{(1)}\cdot\boldsymbol{u}^{(1)}\right]_2+\left[\tfrac{1}{2}\rho^{(1)}\boldsymbol{u}^{(1)}\cdot\boldsymbol{u}^{(1)}\right]_3 \quad \text{(B.7)}$$

The energy density can be subdivided into

$$\mathscr{E}=\bar{\mathscr{E}}+\mathscr{E}'=\mathscr{E}_0+\mathscr{E}_1+\mathscr{E}_2+\mathscr{E}_3 \quad \text{(B.8)}$$

where

$$\begin{cases}\mathscr{E}_0=\dfrac{\bar{P}}{\gamma(\gamma-1)}+O\left(M_b^2\right)\\ \mathscr{E}_1=\dfrac{\left(\bar{\rho}T^{(1)}+\bar{T}\rho^{(1)}\right)}{\gamma(\gamma-1)}+\bar{\rho}\bar{M}_b\boldsymbol{U}\cdot\boldsymbol{u}^{(1)}+O\left(M_b^2\right)\\ \mathscr{E}_2=\dfrac{\rho^{(1)}T^{(1)}}{\gamma(\gamma-1)}+\rho^{(1)}\bar{M}_b\boldsymbol{U}\cdot\boldsymbol{u}^{(1)}+\tfrac{1}{2}\bar{\rho}\boldsymbol{u}^{(1)}\cdot\boldsymbol{u}^{(1)}+O\left(M_b^2\right)\\ \mathscr{E}_3=\tfrac{1}{2}\rho^{(1)}\boldsymbol{u}^{(1)}\cdot\boldsymbol{u}^{(1)}+O\left(M_b^2\right)\end{cases} \quad \text{(B.9)}$$

The time averaging of the second and fourth terms goes to zero. The only term that stands is the third term which involves quadratic combinations of the oscillating variables

$$\mathscr{E}_2=\frac{\rho^{(1)}T^{(1)}}{\gamma(\gamma-1)}+\rho^{(1)}\bar{M}_b\boldsymbol{U}\cdot\boldsymbol{u}^{(1)}+\tfrac{1}{2}\bar{\rho}\boldsymbol{u}^{(1)}\cdot\boldsymbol{u}^{(1)} \quad \text{(B.10)}$$

To write Eq. (B.10) in terms of the pressure, some algebra is needed. To start we split Eq. (4.2) – (4.5) into steady and unsteady parts. The unsteady parts can be written as:

Continuity

$$\frac{\partial \rho^{(1)}}{\partial t} = -\bar{M}_b \nabla \cdot \left(\rho^{(1)} \boldsymbol{U} \right) - \nabla \cdot \left(\bar{\rho} \boldsymbol{u}^{(1)} \right) \tag{B.11}$$

Momentum

$$\frac{\partial \boldsymbol{u}^{(1)}}{\partial t} = \left\{ -\bar{M}_b \nabla \left(\boldsymbol{U} \cdot \boldsymbol{u}^{(1)} \right) + \bar{M}_b \left(\boldsymbol{U} \times \boldsymbol{\omega}^{(1)} + \boldsymbol{u}^{(1)} \times \boldsymbol{\Omega} \right) - \tfrac{1}{2} \nabla \left(\boldsymbol{u}^{(1)} \cdot \boldsymbol{u}^{(1)} \right) \right.$$

$$\left. + \boldsymbol{u}^{(1)} \times \boldsymbol{\omega}^{(1)} + \frac{1}{\bar{\rho}} \left[-\nabla p^{(1)} / \gamma - \delta^2 \nabla \times \boldsymbol{\omega}^{(1)} + \delta_d^2 \nabla \left(\nabla \cdot \boldsymbol{u}^{(1)} \right) + \boldsymbol{F}^{(1)} \right] \right\} \tag{B.12}$$

Energy

$$\frac{\partial p^{(1)}}{\partial t} = \left\{ -\bar{M}_b \nabla \cdot \left(p^{(1)} \boldsymbol{U} \right) - \bar{M}_b (\gamma - 1) p^{(1)} \nabla \cdot \boldsymbol{U} - \nabla \cdot \left(\bar{P} \boldsymbol{u}^{(1)} \right) - (\gamma - 1) \bar{P} \nabla \cdot \boldsymbol{u}^{(1)} \right\} \tag{B.13}$$

Equation of state

$$p^{(1)} = \left(\bar{T} \rho^{(1)} + \bar{\rho} T^{(1)} \right) + \left(\rho^{(1)} T^{(1)} \right) \tag{B.14}$$

From these equations, it can be show that

$$\rho^{(1)} = p^{(1)} / \gamma + O\left(\varepsilon^2 \right) \tag{B.15}$$

$$T^{(1)} = \frac{(\gamma - \bar{T})}{\gamma \bar{\rho}} p^{(1)} + O\left(\varepsilon^2 \right) \tag{B.16}$$

By inserting Eq. (B.15) and (B.16) into Eq. (B.10), one gets

$$\mathscr{E}_2 = \frac{1}{\gamma^3 \bar{P}} \left[p^{(1)} \right]^2 + \rho^{(1)} \bar{M}_b \boldsymbol{U} \cdot \boldsymbol{u}^{(1)} + \tfrac{1}{2} \bar{\rho} \boldsymbol{u}^{(1)} \cdot \boldsymbol{u}^{(1)} \tag{B.17}$$

Based on the representation of Eq. (4.11), Eq. (B.9) can be rewritten as

$$\begin{cases} \mathscr{E}_1 = \varepsilon E_1 = \varepsilon\left[\dfrac{\left(\bar{\rho}T' + \bar{T}\rho'\right)}{\gamma(\gamma-1)} + \bar{\rho}\bar{M}_b U\cdot\boldsymbol{u}'\right] \\ \mathscr{E}_2 = \varepsilon^2 E_2 = \varepsilon^2\left[\dfrac{1}{\gamma^3\bar{P}}\left(p'\right)^2 + \rho'\bar{M}_b U\cdot\boldsymbol{u}' + \tfrac{1}{2}\bar{\rho}\boldsymbol{u}'\cdot\boldsymbol{u}'\right] \\ \mathscr{E}_3 = \varepsilon^3 E_3 = \varepsilon^3\left(\tfrac{1}{2}\rho'\boldsymbol{u}'\cdot\boldsymbol{u}'\right) \end{cases} \tag{B.18}$$

Notice that the steady part $\mathscr{E}_0$ is ignored. The only energy term that stands is the second term since time averaging for the first and the third is zero. Inserting Eq. (B.18) into (B.1) results in

$$2\varepsilon\frac{\mathrm{d}\varepsilon}{\mathrm{d}t}\langle E_2\rangle = \left\langle \begin{array}{l} -\nabla\cdot\left\{\rho\boldsymbol{u}\left[\dfrac{T}{\gamma(\gamma-1)} + \tfrac{1}{2}\boldsymbol{u}\cdot\boldsymbol{u}\right]\right\} - \\ -\dfrac{1}{\gamma}\nabla\cdot(p\boldsymbol{u}) + \rho\boldsymbol{u}\cdot(\boldsymbol{u}\times\boldsymbol{\omega}) + \boldsymbol{u}\cdot\boldsymbol{F} + \dot{Q} \\ +\delta^2\left[\boldsymbol{\omega}\cdot\boldsymbol{\omega} - \boldsymbol{u}\cdot\nabla\times\boldsymbol{\omega}\right] + \delta_d^2\boldsymbol{u}\cdot\nabla(\nabla\cdot\boldsymbol{u}) \\ +\left[\dfrac{\delta^2}{(\gamma-1)Pr}\nabla^2 T + \delta_d^2(\nabla\cdot\boldsymbol{u})^2\right] \end{array} \right\rangle - \frac{1}{\gamma(\gamma-1)}\left\langle\frac{\mathrm{d}\bar{P}}{\mathrm{d}t}\right\rangle \tag{B.19}$$

where

$$\frac{\partial\mathscr{E}}{\partial t} = \frac{\partial\mathscr{E}_0}{\partial t} + \frac{\mathrm{d}\varepsilon}{\mathrm{d}t}E_1 + 2\varepsilon\frac{\mathrm{d}\varepsilon}{\mathrm{d}t}E_2 + 3\varepsilon^2\frac{\mathrm{d}\varepsilon}{\mathrm{d}t}E_3 \tag{B.20}$$

Giving

$$\frac{\partial\mathscr{E}_0}{\partial t} = \frac{1}{\gamma(\gamma-1)}\left\langle\frac{\mathrm{d}\bar{P}}{\mathrm{d}t}\right\rangle \tag{B.21}$$

Recall from before that

$$\langle\mathscr{E}_2\rangle = \frac{1}{\gamma^3\bar{P}}\left\langle\left(p'\right)^2\right\rangle + \tfrac{1}{2}\bar{\rho}\langle\boldsymbol{u}'\cdot\boldsymbol{u}'\rangle \tag{B.22}$$

Then noting that

$$\langle \mathscr{E}_1 \rangle = \left\langle \frac{(\bar{\rho}T' + \bar{T}\rho')}{\gamma(\gamma-1)} + \bar{\rho}\bar{M}_b U \cdot \boldsymbol{u}' \right\rangle = 0 \text{ and } \langle \mathscr{E}_3 \rangle = \left\langle \tfrac{1}{2}\rho' \boldsymbol{u}' \cdot \boldsymbol{u}' \right\rangle = 0 \qquad \text{(B.23)}$$

Expanding the terms on the RHS of Eq. (B.19), one obtains

$$\rho \boldsymbol{V} T = (\bar{\rho} + \varepsilon\rho')(\bar{M}_b U + \varepsilon \boldsymbol{u}')(\bar{T} + \varepsilon T') = (\bar{M}_b U + \varepsilon \boldsymbol{u}')(\bar{\rho}\bar{T} + \varepsilon\bar{\rho}T' + \varepsilon\rho'\bar{T} + \varepsilon^2 \rho' T')$$

$$= \bar{M}_b U \bar{\rho}\bar{T} + \varepsilon\left(\bar{M}_b U \bar{\rho} T' + \bar{M}_b U \rho' \bar{T} + \boldsymbol{u}' \bar{\rho}\bar{T}\right)$$

$$+ \varepsilon^2\left(\bar{M}_b U \rho' T' + \boldsymbol{u}' \bar{\rho} T' + \boldsymbol{u}' \rho' \bar{T}\right) + \varepsilon^3 \boldsymbol{u}' \rho' T' \qquad \text{(B.24)}$$

And so, implementing time averaging, one is left with

$$\langle \rho \boldsymbol{V} T \rangle = \bar{M}_b U \bar{\rho}\bar{T} + \varepsilon^2 \langle \bar{M}_b U \rho' T' + \boldsymbol{u}' \bar{\rho} T' + \boldsymbol{u}' \rho' \bar{T} \rangle \qquad \text{(B.25)}$$

The first term can be written as

$$-\left\langle \nabla \cdot \frac{\rho \boldsymbol{V} T}{\gamma(\gamma-1)} \right\rangle = -\nabla \cdot \left(\frac{\bar{M}_b U \bar{P}}{\gamma(\gamma-1)} \right) - \varepsilon^2 \frac{1}{\gamma(\gamma-1)} \begin{bmatrix} \bar{M}_b \nabla \cdot \left(U \langle \rho' T' \rangle \right) \\ + \nabla \cdot \left\langle \boldsymbol{u}' \left(\bar{\rho} T' + \bar{T} \rho' \right) \right\rangle \end{bmatrix} \qquad \text{(B.26)}$$

After expanding the second term and dropping the order of $\bar{M}_b^2$ we get:

$$\rho \boldsymbol{V}(\boldsymbol{V} \cdot \boldsymbol{V}) = \varepsilon^2 \bar{M}_b \bar{\rho}\left[2\boldsymbol{u}'(U \cdot \boldsymbol{u}') + U(\boldsymbol{u}' \cdot \boldsymbol{u}') \right] + \varepsilon^3 \left[2\bar{M}_b \boldsymbol{u}' \rho' (U \cdot \boldsymbol{u}') + \left(\bar{M}_b U \rho' + \boldsymbol{u}' \bar{\rho} \right)(\boldsymbol{u}' \cdot \boldsymbol{u}') \right]$$

$$+ \varepsilon^4 \boldsymbol{u}' \rho' (\boldsymbol{u}' \cdot \boldsymbol{u}') + O\left(\bar{M}_b^2 \right) \qquad \text{(B.27)}$$

Time averaging of the second term leads to

$$\left\langle \tfrac{1}{2} \nabla \cdot \rho \boldsymbol{V}(\boldsymbol{V} \cdot \boldsymbol{V}) \right\rangle = \tfrac{1}{2} \nabla \cdot \left\{ \varepsilon^2 \bar{M}_b \bar{\rho} \begin{bmatrix} 2\langle \boldsymbol{u}'(U \cdot \boldsymbol{u}') \rangle \\ + U \langle \boldsymbol{u}' \cdot \boldsymbol{u}' \rangle \end{bmatrix} + \varepsilon^4 \langle \rho' \boldsymbol{u}' (\boldsymbol{u}' \cdot \boldsymbol{u}') \rangle \right\} + O\left(\bar{M}_b^2 \right) \qquad \text{(B.28)}$$

In like manner, third term expansion gives

$$\left\langle \frac{1}{\gamma} \nabla \cdot P \boldsymbol{U} \right\rangle = \frac{1}{\gamma} \nabla \cdot \left\langle \bar{P} \bar{M}_b U + \varepsilon\left(\bar{P} \boldsymbol{u} + p' \bar{M}_b U \right) + \varepsilon^2 p' \boldsymbol{u}' \right\rangle$$

$$= \frac{1}{\gamma}\nabla\cdot\bar{P}\bar{M}_b\boldsymbol{U} + \varepsilon^2\frac{1}{\gamma}\nabla\cdot\langle p'\boldsymbol{u}'\rangle \tag{B.29}$$

After expanding and dropping orders of $\bar{M}_b^2$ and higher, the fourth term becomes:

$$\langle\rho\boldsymbol{V}\cdot\boldsymbol{V}\times\boldsymbol{\omega}\rangle = \varepsilon^2\bar{\rho}\begin{bmatrix}\boldsymbol{U}\cdot\langle\boldsymbol{u}'\times\boldsymbol{\omega}'\rangle + \langle\boldsymbol{u}'\cdot\boldsymbol{U}\times\boldsymbol{\omega}'\rangle \\ +\langle\boldsymbol{u}'\cdot\boldsymbol{u}'\times\boldsymbol{\Omega}\rangle\end{bmatrix} + \langle\rho'\boldsymbol{u}'\cdot\boldsymbol{u}'\times\boldsymbol{\omega}'\rangle + O\left(\bar{M}_b^2\right) \tag{B.30}$$

The same procedure applied to the next term gives

$$\left\langle\delta_d^2\boldsymbol{V}\cdot\nabla\left(\nabla\cdot\boldsymbol{V}\right)\right\rangle = \varepsilon^2\delta_d^2\left\langle\boldsymbol{u}'\cdot\nabla\left(\nabla\cdot\boldsymbol{u}'\right)\right\rangle = O\left(\bar{M}_b^2\right) \tag{B.31}$$

Thus we have

$$\frac{1}{\gamma(\gamma-1)}\left\langle\frac{\mathrm{d}P}{\mathrm{d}t}\right\rangle = \frac{1}{\gamma(\gamma-1)}\begin{bmatrix}-\bar{M}_b\nabla\cdot\left(\bar{P}\boldsymbol{U}\right) \\ +(\gamma-1)\bar{P}\nabla\cdot\boldsymbol{U}\end{bmatrix} + \varepsilon^2\frac{1}{\gamma(\gamma-1)}\nabla\cdot\langle p'\boldsymbol{u}'\rangle \tag{B.32}$$

Combining all of the above terms results in:

$$\begin{aligned}
2\varepsilon\frac{\mathrm{d}\varepsilon}{\mathrm{d}t}\langle E_2\rangle = &-\frac{1}{\gamma(\gamma-1)}\left\langle-\bar{M}_b\nabla\cdot\left(\bar{P}\boldsymbol{U}\right)-\bar{M}_b(\gamma-1)\bar{P}\nabla\cdot\boldsymbol{U}\right\rangle-\nabla\cdot\left(\frac{\bar{M}_b\boldsymbol{U}\bar{P}}{\gamma(\gamma-1)}\right)-\frac{\bar{M}_b}{\gamma}\nabla\cdot\bar{P}\boldsymbol{U} \\
&+\varepsilon^2\left\{\frac{1}{\gamma(\gamma-1)}\left[\left\langle\nabla\cdot\left(p'\boldsymbol{u}'\right)\right\rangle-\nabla\cdot\left\langle\boldsymbol{u}'\left(\bar{\rho}T'+\bar{T}\rho'\right)\right\rangle\right]-\frac{1}{\gamma}\nabla\cdot\langle p'\boldsymbol{u}'\rangle\right. \\
&\quad-\begin{bmatrix}\frac{1}{\gamma(\gamma-1)}\bar{M}_b\nabla\cdot\left(\boldsymbol{U}\langle\rho'T'\rangle\right)+\frac{1}{2}\bar{M}_b\nabla\cdot\left(\boldsymbol{U}\bar{\rho}\langle\boldsymbol{u}'\cdot\boldsymbol{u}'\rangle\right) \\ +\bar{M}_b\bar{\rho}\nabla\cdot\left\langle\boldsymbol{u}'\left(\boldsymbol{U}\cdot\boldsymbol{u}'\right)\right\rangle\end{bmatrix} \\
&\quad+\bar{M}_b\left[\bar{\rho}\boldsymbol{U}\cdot\langle\boldsymbol{u}'\times\boldsymbol{\omega}'\rangle+\bar{\rho}\boldsymbol{u}'\cdot\langle\boldsymbol{U}\times\boldsymbol{\omega}'+\boldsymbol{u}'\times\boldsymbol{\Omega}\rangle\right] \\
&\quad+\delta^2\langle\boldsymbol{\omega}'\cdot\boldsymbol{\omega}'-\boldsymbol{u}'\cdot\nabla\times\boldsymbol{\omega}'\rangle+\delta_d^2\left\langle\boldsymbol{u}'\cdot\nabla\left(\nabla\cdot\boldsymbol{u}'\right)\right\rangle \\
&\quad\left.+\left\langle\left\{\frac{\delta^2}{(\gamma-1)Pr}\nabla^2T+\delta_d^2\left(\nabla\cdot\boldsymbol{u}\right)^2\right\}\right\rangle\right\} \\
&-\varepsilon^4\left\{\nabla\cdot\left\langle\tfrac{1}{2}\rho'\boldsymbol{u}'\left(\boldsymbol{u}'\cdot\boldsymbol{u}'\right)\right\rangle-\left\langle\rho'\boldsymbol{u}'\cdot\left(\boldsymbol{u}'\times\boldsymbol{\omega}'\right)\right\rangle\right\}
\end{aligned} \tag{B.33}$$

From Eq. (B.33) the zeroth order vanishes as seen below:

$$-\frac{1}{\gamma(\gamma-1)}\left\langle-\bar{M}_b\nabla\cdot\left(\bar{P}\boldsymbol{U}\right)-\bar{M}_b(\gamma-1)\bar{P}\nabla\cdot\boldsymbol{U}\right\rangle-\nabla\cdot\left(\frac{\bar{M}_b\boldsymbol{U}\bar{P}}{\gamma(\gamma-1)}\right)-\frac{\bar{M}_b}{\gamma}\nabla\cdot\bar{P}\boldsymbol{U}=0 \tag{B.34}$$

Giving

$$\frac{\bar{M}_b}{\gamma}\nabla\cdot\bar{P}\boldsymbol{U}=\frac{\bar{M}_b\bar{P}}{\gamma}\nabla\cdot\boldsymbol{U}+\frac{\bar{M}_b\boldsymbol{U}}{\gamma}\cdot\nabla\bar{P} \tag{B.35}$$

and since we have defined the quasi-steady pressure as a property that is only time dependent, the second term on the RHS of Eq. (B.35) is zero by definition. Hence, we have

$$\frac{\bar{M}_b}{\gamma}\nabla\cdot\bar{P}\boldsymbol{U}=\frac{\bar{M}_b\bar{P}}{\gamma}\nabla\cdot\boldsymbol{U} \tag{B.36}$$

Using these simplifications, Eq. (B.33) can be written as:

$$\frac{\bar{M}_b}{\gamma}\nabla\cdot\bar{P}\boldsymbol{U}=\frac{\bar{M}_b\bar{P}}{\gamma}\nabla\cdot\boldsymbol{U}+\frac{\bar{M}_b\boldsymbol{U}}{\gamma}\cdot\nabla\bar{P} \tag{B.37}$$

$$\frac{\mathrm{d}\varepsilon}{\mathrm{d}t}=\frac{1}{2\langle E_2\rangle}\left\{\begin{array}{l}\varepsilon\left[\begin{array}{l}-\frac{1}{\gamma}\nabla\cdot\langle p'\boldsymbol{u}'\rangle-\frac{\bar{M}_b}{\gamma\bar{P}}\nabla\cdot\left\langle\boldsymbol{U}(p'/\gamma)^2\right\rangle\\ -\bar{M}_b\bar{P}\nabla\cdot\left\langle\frac{1}{2}\boldsymbol{U}(\boldsymbol{u}'\cdot\boldsymbol{u}')+\boldsymbol{u}'(\boldsymbol{U}\cdot\boldsymbol{u}')\right\rangle\\ +\bar{M}_b\bar{P}\left[\boldsymbol{U}\cdot\langle\boldsymbol{u}'\times\boldsymbol{\omega}'\rangle+\boldsymbol{u}'\cdot\langle\boldsymbol{U}\times\boldsymbol{\omega}'+\boldsymbol{u}'\times\boldsymbol{\Omega}\rangle\right]\\ +\delta^2\langle\nabla\cdot(\boldsymbol{u}'\times\boldsymbol{\omega}')\rangle+\delta_d^2\langle\boldsymbol{u}'\cdot\nabla(\nabla\cdot\boldsymbol{u}')\rangle\end{array}\right]\\ \qquad+\frac{1}{\varepsilon}\left\langle\frac{\delta^2}{(\gamma-1)Pr}\nabla^2T+\delta_d^2(\nabla\cdot\boldsymbol{u})^2\right\rangle\\ +\varepsilon^3\left[-\nabla\cdot\left\langle\frac{1}{2}\rho'\boldsymbol{u}'(\boldsymbol{u}'\cdot\boldsymbol{u}')\right\rangle+\langle\rho'\boldsymbol{u}'\cdot(\boldsymbol{u}'\times\omega')\rangle\right]\end{array}\right\} \tag{B.38}$$

The time average for the energy density has been carried over the chamber volume to account for all possible gas interactions. At the outset, one has

$$E^2\equiv\iiint_V\langle E_2\rangle\mathrm{d}V=\iiint_V\left\langle\frac{1}{\gamma^3\bar{P}}(p')^2+\frac{1}{2}\bar{P}\boldsymbol{u}'\cdot\boldsymbol{u}'\right\rangle\mathrm{d}V \tag{B.39}$$

Integrating over the volume, Eq. (B.38) becomes:

$$\frac{\mathrm{d}\varepsilon}{\mathrm{d}t}=\frac{1}{2E^2}\left\{\begin{array}{l}\varepsilon\iiint_V\left[\begin{array}{l}-\frac{1}{\gamma}\nabla\cdot\langle p'\boldsymbol{u}'\rangle-\frac{\bar{M}_b}{\gamma\bar{P}}\nabla\cdot\left(\boldsymbol{U}\left\langle(p'/\gamma)^2\right\rangle\right)\\-\bar{M}_b\bar{P}\nabla\cdot\left\langle\frac{1}{2}\boldsymbol{U}(\boldsymbol{u}'\cdot\boldsymbol{u}')+\boldsymbol{u}'(\boldsymbol{U}\cdot\boldsymbol{u}')\right\rangle\\+\bar{M}_b\left[\bar{P}\boldsymbol{U}\cdot\langle\boldsymbol{u}'\times\boldsymbol{\omega}'\rangle+\bar{P}\boldsymbol{u}'\cdot\langle\boldsymbol{U}\times\boldsymbol{\omega}'+\boldsymbol{u}'\times\boldsymbol{\Omega}\rangle\right]\\+\delta^2\nabla\cdot\langle\boldsymbol{u}'\times\boldsymbol{\omega}'\rangle+\delta_d^2\left\langle\boldsymbol{u}'\cdot\nabla(\nabla\cdot\boldsymbol{u}')\right\rangle\end{array}\right]\mathrm{d}V\\+\frac{1}{\varepsilon}\iiint_V\left\langle\frac{\delta^2}{(\gamma-1)Pr}\nabla^2T+\delta_d^2(\nabla\cdot\boldsymbol{u})^2\right\rangle\mathrm{d}V\\+\varepsilon^3\iiint_V\left[-\nabla\cdot\left\langle\frac{1}{2}\rho'\boldsymbol{u}'(\boldsymbol{u}'\cdot\boldsymbol{u}')\right\rangle+\left\langle\rho'\boldsymbol{u}'\cdot(\boldsymbol{u}'\times\boldsymbol{\omega}')\right\rangle\right]\mathrm{d}V\end{array}\right\}\tag{B.40}$$

Note that the rate of change of the system amplitude can be written in the convenient form

$$\frac{\mathrm{d}\varepsilon}{\mathrm{d}t}=\alpha^{(1)}\varepsilon+\alpha^{(2)}\varepsilon^2+\alpha^{(3)}\varepsilon^3+\cdots\tag{B.41}$$

where $\alpha^{(1)}$ represents the linear growth rate for the wave system. And since we are dealing with the linear theory, we focus our attention on the first term only, specifically,

$$\alpha^{(1)}=\frac{1}{2E^2}\left\{\iiint_V\left[\begin{array}{l}-\frac{1}{\gamma}\nabla\cdot\langle p'\boldsymbol{u}'\rangle-\frac{\bar{M}_b}{\gamma^3\bar{P}}\nabla\cdot\left(\boldsymbol{U}\left\langle(p')^2\right\rangle\right)\\-\bar{M}_b\bar{P}\nabla\cdot\left\langle\frac{1}{2}\boldsymbol{U}(\boldsymbol{u}'\cdot\boldsymbol{u}')+\boldsymbol{u}'(\boldsymbol{U}\cdot\boldsymbol{u}')\right\rangle\\+\bar{M}_b\left[\bar{P}\boldsymbol{U}\cdot\langle\boldsymbol{u}'\times\boldsymbol{\omega}'\rangle+\bar{P}\boldsymbol{u}'\cdot\langle\boldsymbol{U}\times\boldsymbol{\omega}'+\boldsymbol{u}'\times\boldsymbol{\Omega}\rangle\right]\\+\delta^2\nabla\cdot\langle\boldsymbol{u}'\times\boldsymbol{\omega}'\rangle+\delta_d^2\left\langle\boldsymbol{u}'\cdot\nabla(\nabla\cdot\boldsymbol{u}')\right\rangle\end{array}\right]\mathrm{d}V\right\}\tag{B.42}$$

The final expression becomes:

$$\alpha^{(1)} = \frac{1}{2E^2}\left\{\begin{array}{l} -\dfrac{1}{\gamma}\iint_S \boldsymbol{n}\cdot\langle p'\boldsymbol{u}'\rangle \mathrm{d}S - \dfrac{\bar{M}_b}{\gamma^3\bar{P}}\iint_S \boldsymbol{n}\cdot\boldsymbol{U}\left\langle (p')^2\right\rangle \mathrm{d}S \\ -\bar{M}_b\bar{P}\iint_S \boldsymbol{n}\cdot\left\langle \tfrac{1}{2}\boldsymbol{U}(\boldsymbol{u}'\cdot\boldsymbol{u}') + \boldsymbol{u}'(\boldsymbol{U}\cdot\boldsymbol{u}')\right\rangle \mathrm{d}S \\ +\bar{M}_b\bar{P}\iiint_V \boldsymbol{U}\cdot\langle \boldsymbol{u}'\times\boldsymbol{\omega}'\rangle \mathrm{d}V + \bar{M}_b\bar{P}\iiint_V \boldsymbol{u}'\cdot\langle \boldsymbol{U}\times\boldsymbol{\omega}'\rangle \mathrm{d}V \\ +\delta^2\iint_S \boldsymbol{n}\cdot\langle \boldsymbol{u}'\times\boldsymbol{\omega}'\rangle \mathrm{d}S + \delta_d^2\iiint_V \left\langle \boldsymbol{u}'\cdot\nabla(\nabla\cdot\boldsymbol{u}')\right\rangle \mathrm{d}V \\ +\bar{M}_b\bar{P}\iiint_V \boldsymbol{u}'\cdot\langle \boldsymbol{u}'\times\boldsymbol{\Omega}\rangle \mathrm{d}V \end{array}\right\} \qquad \text{(B.43)}$$

C. Time Averaging

After all needed terms in Eq. (4.47) and (4.50) are converted to surface integrals, time averaging can be pursued. To start, we define the time average function as

$$\langle f(t)\rangle = \lim_{T\to\infty}\frac{1}{T}\int_0^T f(t)dt \tag{C.1}$$

The hydrodynamic fluctuations can be written as

$$\begin{cases} \breve{p} = A_0|p|\left[\cos\left(n_r+q\theta+\beta_p\right)\cos\left(\omega t\right)+\sin\left(n_r+q\theta+\beta_p\right)\sin\left(\omega t\right)\right]e^{n_i} \\ \breve{u} = A_0|u|\left[\cos\left(n_r+q\theta+\beta_u\right)\cos\left(\omega t\right)+\sin\left(n_r+q\theta+\beta_u\right)\sin\left(\omega t\right)\right]e^{n_i} \end{cases} \tag{C.2}$$

The combustion instability fluctuations can be written as

$$\begin{cases} \hat{u}_z = \sin\left(M_b\omega z\right)\sin\left(\omega t\right) \\ \hat{p} = \cos\left(M_b\omega z\right)\cos\left(\omega t\right) \\ \tilde{u} = \tilde{u}_m^r\cos(\omega t)+\tilde{u}_m^i\sin(\omega t) \\ \tilde{p} = \tilde{p}_m^r\cos(\omega t)+\tilde{p}_m^i\sin(\omega t) \end{cases} \tag{C.3}$$

The time average of the terms in Eqs. (4.47) and (4.50) are summarized as follows:

$$\begin{cases} \langle\breve{p}\hat{p}\rangle = \frac{1}{2}|p|\,\hat{p}_m\cos\left(n_r+q\theta+\beta_p\right)e^{n_i} \\ \langle\breve{u}_z\hat{p}\rangle = \frac{1}{2}|u_z|\,\hat{p}_m\cos\left(n_r+q\theta+\beta_{u_z}\right)e^{2n_i} \\ \langle\breve{p}\breve{u}_z\rangle = \frac{1}{2}|p||u_z|\cos\left(\beta_p-\beta_{u_z}\right)e^{2n_i} \\ \langle\hat{u}_z\breve{u}_z\rangle = \frac{1}{2}\hat{u}_{m_z}|u_z|\sin\left(n_r+q\theta+\beta_{u_z}\right)e^{n_i} \\ \langle\breve{p}^2\rangle = \frac{1}{2}|p|^2e^{n_i} \\ \langle\breve{u}_z^2\rangle = \frac{1}{2}|u_z|^2e^{2n_i} \\ \langle\breve{u}_r^2\rangle = \frac{1}{2}|u_r|^2e^{2n_i} \\ \langle\breve{u}_\theta^2\rangle = \frac{1}{2}|u_\theta|^2e^{2n_i} \end{cases} \tag{C.4}$$

D. Integration Using Gaussian Quadrature

In what follows we describe the numerical discretization procedure for evaluating the various instability integrals. These correspond to the surface and nozzle growth rates given by Eqs. (4.65)–(4.68) in addition to the energy density functions given by Eqs. (4.70)–(4.71). Step-by-step, we thus have:

Surface growth rate:

$$q=0: \quad \alpha^{(1)}_{hyd,w}=\frac{\pi}{E^2}\left\{\begin{array}{l}\dfrac{M_b(1+A_b^r)A_0}{2\gamma}m_z\displaystyle\sum_{k=1}^{150}C_k\left[|p|\hat{p}_m\cos\left(n_r+\beta_p\right)\right]e^{n_i}\\ \dfrac{M_b m_z}{\gamma^3\overline{P}}\displaystyle\sum_{k=1}^{150}\left\{C_k\left[\frac{A_0^2}{2}|p|^2e^{2n_i}+\left(A_0|p|\hat{p}_m\cos\left(n_r+\beta_p\right)e^{n_i}\right)\right]\right\}\end{array}\right. \tag{D.1}$$

$$q\geq 1: \quad \alpha^{(1)}_{hyd,w}=\frac{\pi}{E^2}\left\{\frac{A_0^2M_b m_z}{2\gamma^3\overline{P}}\sum_{k=1}^{150}\left(C_k|p|^2e^{2n_i}\right)\right. \tag{D.2}$$

Nozzle growth rate:

$$q=0: \quad \alpha^{(1)}_{hyd,N}=\frac{\pi}{E^2}\left\{\begin{array}{l}-\dfrac{A_0m_r}{2\gamma}\displaystyle\sum_{k=1}^{150}C_k\left\{\left[\begin{array}{c}|u_z|\hat{p}_m\cos\left(n_r+\beta_p\right)\\ +|p|\left(\begin{array}{c}A_0|u_z|\cos\left(\beta_p-\beta_{u_z}\right)e^{n_i}\\ +\hat{u}_{m_z}\sin\left(n_r+\beta_p\right)\end{array}\right)\end{array}\right]r_ke^{n_i}\right\}\\ -\dfrac{A_0M_bm_r}{\gamma^3\overline{P}}U_z\displaystyle\sum_{k=1}^{150}C_k\left\{\left[\frac{A_0}{2}|p|^2e^{n_i}+|p|\hat{p}_m\cos\left(n_r+\beta_p\right)\right]r_ke^{n_i}\right\}\\ -\frac{1}{2}A_0M_b\overline{P}U_zm_r\displaystyle\sum_{k=1}^{150}C_k\left\{\left[\begin{array}{l}\hat{u}_{m_z}|u_z|\sin\left(n_r+\beta_p\right)\\ +\dfrac{A_0}{2}\left(|u_r|^2+|u_z|^2\right)e^{n_i}\\ +\hat{u}_{m_z}|u_z|\sin\left(n_r+\beta_p\right)\end{array}\right]r_ke^{n_i}\right\}\end{array}\right. \tag{D.3}$$

$$q \geq 1: \qquad \alpha_{hyd,N}^{(1)} = -\frac{\pi}{E^2}\left\{\begin{array}{l} \dfrac{M_b U_z A_0^2 m_r}{2\gamma^3 \bar{P}} \sum_{k=1}^{150} C_k \left(r_k |p|^2\right) e^{2n_i} \\ + \dfrac{M_b \bar{P} U_z A_0^2 m_r}{4} \sum_{k=1}^{150} C_k \left[r_k \left(|u_r|^2 + |u_\theta|^2 + |u_z|^2 \right) \right] e^{2n_i} \end{array}\right. \tag{D.4}$$

Energy density:

$$q = 0: \quad E_{hyd}^2 = \pi \left\{ \begin{array}{l} \underbrace{\dfrac{A_0^2 m_z m_r}{2} \sum_{k=1}^{150} C_k \left\{ \left[\sum_{p=1}^{p=150} C_p \left(|p|^2 + |u_r|^2 + |u_z|^2 \right) r_p \right] e^{2n_i} \right\}}_{\text{pure hydrodynamic}} \\ + A_0 m_z m_r \sum_{k=1}^{150} \left\{ C_k \left[\sum_{p=1}^{150} C_p \left(\begin{array}{c} |u_z| \left(\begin{array}{c} \tilde{u}_{m_z}^r \cos\left(n_r + \beta_{u_z}\right) + \\ \left(\tilde{u}_{m_z}^i + \hat{u}_{m_z}\right) \sin\left(n_r + \beta_{u_z}\right) \end{array} \right) \\ \hat{p}_m |p| \cos\left(n_r + \beta_p\right) \end{array} \right) r_p \right] e^{n_i} \right\} \end{array} \right. \tag{D.5}$$

$$q \geq 1: \qquad E_{hyd}^2 = \pi \left\{ \underbrace{\dfrac{A_0^2 m_z m_r}{2} \sum_{k=1}^{150} C_k \left\{ \left[\sum_{p=1}^{150} C_p \left(|p|^2 + |u_r|^2 + |u_\theta|^2 + |u_z|^2 \right) r_p \right] e^{2n_i} \right\}}_{\text{pure hydrodynamic}} \right. \tag{D.6}$$

Finally Eq. (4.75) can be represented as

$$A_0 = -\frac{\hat{p}_m e^{-n_i}}{2 \sum_{p=1}^{150} C_p \left(|p| \cos\left(n_r + q\theta\right) \right) r_p} \tag{D.7}$$

E. Integral Code

Program: General code
Author: Mr. Abu-Irshaid
Input: Admitance function value 'Ab', initial amplitude A_0 ='IAO', Mach number 'M', initial guesses for each motor which include at each Mach number 'M': the complex eigenvalue 'k', the critical axial location z_0='Z_Lo', and the maximum number of iteration 'itmax'
Output: Eigenvalues (σ_r, σ_i)= 'real(alfa),imag(alfa)', the six amplitude eigenfunctions $(u_r, u_\theta, u_z, p, \mathrm{d}u_\theta/\mathrm{d}r, \mathrm{d}u_z/\mathrm{d}r)$= 'ur,ut,uz,p,dut/dr, duz/dr', the surface growth rate $\alpha_{hyd,w}$= 'Total_solution', the hydrodynamic energy density E_{hyd}= 'Energy_den_hyd', and the initial amplitude A_0 ='IAO'

```
clear;clc;format long
dval=1e-4;
itmax=30;
npo1=149;
n=npo1+1;
q=0;
it=0;
uh=0;
Ab=1.2;
nf=0;

%L=10;
% M=[.0015:.0005:.01]; L=10
alfainitial_r=[33.471921944411,26.900444209217,22.459608042518,17.3446370120
33,14.879156689387,13.762096952704,12.078524798074,10.191963942742,...
%    10.977254033866,9.088390001920,7.928212269168,6.852857878782,6.348192
%    870463,6.348192870463,
%    4.969730025475,4.555590043621,4.555590043621,4.555590043621]; L=10
% alfainitial_i=[0.091808171586,0.079161258309,0.41551379648,  0.009170516374,
%0.082634894560, 0.265022029650, 0.244004566961,0.096242568466,...
%    0.672918802215,0.351836466065,0.207237040986,0.113499444392,
%    0.084463986313,
%    0.084463986313,0.064042425121,0.07875223704,0.07875223704,0.07875223
%    704];L=10
% Z_Lo=[10.5,8.3,6.5,5.7,4.9,4.3,3.9,3.7,3,3,3,3,3,3,3,3,3,3];L=10


% L=15:
% M=[.0008:.0002:.006];%L=15
```

%alfainitial_r=[44.432799547258,33.471921944411,27.25673692816 4,26.40178718523
0,22.239425870237,19.418212488541,17.344637012033,15.919697015563,14.22040453
9443,.13.190510441670,12.168563573867,10.894419800590,10.269597308680,9.28535
4702851,9.285354702851,8.406886173703,8.320083966442,7.928212269168,7.9282122
69168,7.928212269168,.6.348192870463,6.348192870463,6.348192870463,5.40649731
7340,5.406497317340,5.406497317340,5.406497317340];%L=15
alfainitial_i=[0.286474750698,0.091808171586,0.029440550511,0.342921609307,0.069
158727453,0.056918252156,0.009170516374,0.070989987907,0.040873137367,
0.059406990574,0.082669522069,0.024402588811,0.002172492812,0.044088571607,0.
044088571607,0.007137352460,0.094234365201,0.207237040986,0.207237040986,0.20
7237040986,
0.084463986313,0.084463986313,0.084463986313,0.060007205334,0.060007205334,0.
060007205334,0.060007205334];%L=15
Z_Lo=[14,10.5,8.6,7.8,7,6.2,5.7,5.2,4.8,4.5,4.2,4,3.9,3.6,3.6,3.5,3.3,3,3,3,3,3,3,3,3,3,3,3];
%L=15

%Small Motor Information
ik=linspace(-4,-3,25);%L=24
for mk=1:23;%L=24
M(mk)=5*10^ik(mk); %L=24
end
alfainitial_r=[43.838427422071,35.364988320857,35.364988320857,28.465347779322,
29.618785204536,25.058411673248,26.267041503918,22.234480069338,19.591871110
129,17.322536081951,17.895420279030,15.438874729746,13.396082143717,12.448413
332042,11.742165094193,9.829179767302,8.720712296408];%L=24
alfainitial_i=[0.076172741073,0.011726414903,0.011726414903,-
0.386386389122,0.008993459882,-0.116167175844,0.325442580304,0.020918459239,-
0.016941267156,0.090699428834,0.109263239525,0.170692381748,0.050369574219,0.
084753550811,0.155773623311,0.027284259711,0.063259226704];%L=24
Z_Lo=[14.2,11.3,11.3,9.8,9.4,8.2,7.8,7.1,6.4,5.9,4.8,4.5,4.6,4.3,4,3.8,3]; %L=24

%Small Motor Hybrid Information
ik=linspace(-4,-3,25);%L=24
for mk=1:23;%L=24
M(mk)=5*10^ik(mk); %L=24
end
alfainitial_r=[43.838427422071,35.364988320857,35.364988320857,28.465347779322,
29.618785204536,25.058411673248,26.267041503918,22.234480069338,19.591871110
129,17.322536081951,17.895420279030,15.438874729746,13.396082143717,12.448413
332042,11.742165094193,9.829179767302,8.720712296408];%L=24
alfainitial_i=[0.076172741073,0.011726414903,0.011726414903,-
0.386386389122,0.008993459882,-0.116167175844,0.325442580304,0.020918459239,-
0.016941267156,0.090699428834,0.109263239525,0.170692381748,0.050369574219,0.
084753550811,0.155773623311,0.027284259711,0.063259226704];%L=24

```
Z_Lo=[12.5,10.5,9.5,8.5,7.9,6.9,5.2,5,4.5,4.1,4,3.7,3.1,3,2.7,2.6,2.3]; %L=24


%Tactical Motor Information
ik=linspace(-4,-3,25);%L=19.9020
for mk=1:25;%L=19.9020
M(mk)=5*10^ik(mk); %L=19.9020
end
alfainitial_r=[49.194660772614,44.169888816567,43.838748032576,41.403291255816,
37.562487518150,34.074860582008,30.881455075293,29.198312889428,25.475474126
878....
23.168519334313,21.275125249024,19.143774806051,16.671854522302,14.648567382
937,13.048789406732,11.291632202158,9.963430122037];%L=19.9020
alfainitial_i=[-0.087386417467,-0.251965162658,
0.071892681461,0.558362829045,0.420355769451,0.316927438683,0.231136453681,0.
641718960276,0.171212854505,0.172434906567,0.258162455783,0.187839974292,0.07
4061846452,0.047960279535, 0.039479659651, 0.074430439733,0.017939127014];
%L=19.9020
 Z_Lo=[16.6,15,14,12.4,11.3,10.3,9.2,8.2,7.4,7,6.2,5.7,5.4,4.9,4.5,3.8,3];%L=19.9020


%Cold Flow Experiment Information
alfainitial_r=[66.780613118693893,64.034192755407318,54.181776304442650,52.7964
45371980,47.552356001161,43.738656312606,39.821563918926,36.317675244446,
33.163990338437,30.003937369879,27.380600637125,24.653185606767,22.370033385
900,20.198332226574,18.390187078149,16.627256618712,15.163215030964,
13.224904244232,12.199847228419,13.969869769223,13.341984210365,11.259263506
415,9.508984793336];%L=33.92156862745098;
alfainitial_i=[0.345762597314724,1.268017877123019,0.644511475505662,0.36096007
0954,0.030851539224,0.103298608397,0.037146037622,0.020510273120,
0.036049815877,-0.038750785849,-0.004422609142,-0.083628307265,-
0.076924041865,-0.096480091691,-0.050568596793,-0.044636554735,0.012684737705,
0.009501880535,-0.020476996434,0.649433745718,0.925730013724, 0.502495227289,
0.230718871243];%L=33.92156862745098;
Z_Lo=[23.3,20,18,17,15.4,14,12.8,11.6,10.5,9.6,8.7,8,7.3,6.7,6.1,5.6,5.1,4.6,4.4,3.8,3.3,3
.3,3]; % L=33.92156862745098;


%SRM Motor Information
alfainitial_r=[95.113431717843,89.733636314521945,84.601584248884095,78.1486302
14427655,74.736708454902228,68.181132827601090,65.965012611273565,60.8617126
70774,56.043885998658,51.856355206549,47.078918000661,43.346424457811,39.7406
30397981,36.198104639948,37.382417219133,34.133807452973,31.130917985098,
28.327645258284,25.982641359639,24.060362984905,21.609699377722,18.948692329
982,20.117931500274,17.747001912101,16.263907714059,14.376451182352,
```

```
13.776451182352,12.164960911733,10.533290420209,11.312851455277,
8.989407090868,9.236727557955 ]; %L=50.1429
alfainitial_i=[0.051779621729,0.106120392054404,0.137894382508959,0.05786042124
5631,0.207644890378530,0.137553779385685,0.066638761286988,0.071047253156,
0.017909176792,0.085140704238,-0.149548563458,-0.115929189068,-
0.127985749771,0.204169168269,0.217547904307,0.158570268908,0.106873308990,0.
050421284837,0.087752611310,0.212879919059,0.077354612718,0.179374649379,0.23
6222775588,0.015857289715,0.067346880218,0.205653031286,0.205653031286,0.0821
72654474,-0.066719736331,0.189737930488,0.062726507097,0.141474613215];
%L=50.1429
Z_Lo=[41,37,33,30,27,24.5,22,21.2,19.2,17.3,15.9,14.4,13.1,12,10.8,10.6,9.7,8.9,8.1,7.3,
6.8,6.5,5.9,5.8,5.3,4.7,4.4,4.2,4.1,3.8,3.4,3];%L=50.1429

wπ1 = pi./(M*L);
ci=complex(0,1);gama=1.23;
reynolds=5e3;delta=6.07e-4;

%10 points
%   t=[ 0.14887434 -0.14887434 0.43339539 -0.43339539 0.67940957 -0.67940957
0.86506337 -0.86506337 0.97390653 -0.97390653];
%    C=[0.29552422 0.29552422 0.26926672 0.26926672 0.21908636 0.21908636
0.14945135 0.14945135 0.06667134 0.06667134];

% % 50 points
% t=[-0.998866, 0.00290862,-0.994032, 0.0067598,-0.985354, 0.0105905, ...
% -0.972864, 0.0143808, -0.956611, 0.0181156,-0.936657, 0.0217802, ...
% -0.913079, 0.0253607,-0.885968, 0.028843,-0.85543, 0.0322137, ...
% -0.821582, 0.0354598,-0.784556, 0.0385688,-0.744494, 0.0415285, ...
% -0.701552, 0.0443275,-0.655896, 0.0469551,-0.607703, 0.0494009, ...
% -0.557158, 0.0516557,-0.504458, 0.0537106,-0.449806, 0.0555577, ...
% -0.393414, 0.0571899,-0.3355, 0.0586008,-0.276288, 0.0597851, ...
% -0.216007, 0.060738,-0.154891, 0.0614559,-0.0931747, 0.0619361, ...
% -0.0310983, 0.0621766,0.0310983, 0.0621766,0.0931747, 0.0619361, ...
%  0.154891, 0.0614559,0.216007, 0.060738,0.276288, 0.0597851, ...
%  0.3355, 0.0586008,0.393414, 0.0571899, ...
%  0.449806, 0.0555577,0.504458, 0.0537106,0.557158, ...
%  0.0516557,0.607703, 0.0494009, 0.655896, 0.0469551,0.701552, ...
%  0.0443275,0.744494, 0.0415285,0.784556, ...
%  0.0385688,0.821582, 0.0354598,0.85543, 0.0322137,0.885968, ...
% 0.028843,0.913079, 0.0253607,0.936657, 0.0217802,0.956611, ...
% 0.0181156,0.972864, 0.0143808,0.985354, 0.0105905, 0.994032, ...
% 0.0067598,0.998866, 0.00290862];

%150 points
t=[-0.999872, 0.000327609,-0.999327, 0.000762472,-0.998347, 0.00119765,...
-0.996932, 0.00163236, -0.995083, 0.00206637,-0.9928, 0.00249948,...
```

-0.990084, 0.0029315,-0.986937, 0.00336225,-0.98336, 0.00379153,...
-0.979355, 0.00421917,-0.974923, 0.00464496,-0.970066, 0.00506873,...
-0.964786, 0.00549029,-0.959086, 0.00590946,-0.952968, 0.00632605,...
-0.946435, 0.00673989,-0.939489, 0.00715079,-0.932134, 0.00755857,...
-0.924373, 0.00796306,-0.916209, 0.00836409,-0.907646, 0.00876146,...
-0.898687, 0.00915502,-0.889337, 0.00954459,-0.8796, 0.00993,...
-0.869479, 0.0103111,-0.858979, 0.0106877,-0.848105, 0.0110596,...
-0.836861, 0.0114267,-0.825253, 0.0117889,-0.813285, 0.0121459,...
-0.800963, 0.0124976,-0.788292, 0.0128438,-0.775277,0.0131845,...
-0.761925,0.0135194,-0.74824, 0.0138485,-0.73423, 0.0141715,...
-0.7199,0.0144883,-0.705255, 0.0147988,-0.690304, 0.0151029,...
-0.675052, 0.0154003,-0.659506, 0.0156911,-0.643672, 0.015975,...
-0.627558,0.016252,-0.61117, 0.0165219,-0.594516, 0.0167846,...
-0.577604, 0.01704,-0.560439, 0.0172879,-0.54303, 0.0175283,...
-0.525385,0.0177611,-0.507511, 0.0179862,-0.489415, 0.0182034,...
-0.471106,0.0184127,-0.452593, 0.0186139,-0.433881, 0.0188071,...
-0.414981,0.018992,-0.3959, 0.0191687,-0.376647, 0.019337,...
-0.357229,0.0194969,-0.337656, 0.0196483,-0.317935, 0.0197911,...
-0.298076,0.0199253,-0.278087, 0.0200509,-0.257977, 0.0201677,...
-0.237755,0.0202757,-0.217429, 0.0203749,-0.197008, 0.0204652,...
-0.176502,0.0205465,-0.155918, 0.020619,-0.135267,0.0206824,...
-0.114556, 0.0207368,-0.0937961, 0.0207822,-0.0729949,0.0208186,...
-0.052162, 0.0208458,-0.0313063, 0.020864,-0.0104369, 0.0208731,...
0.0104369,0.0208731,0.0313063, 0.020864,0.052162, 0.0208458,...
0.0729949,0.0208186,0.0937961, 0.0207822,0.114556, 0.0207368,...
0.135267,0.0206824,0.155918, 0.020619,0.176502, 0.0205465,...
0.197008,0.0204652,0.217429, 0.0203749,0.237755, 0.0202757,...
0.257977,0.0201677,0.27808,0.0200509,0.298076,0.0199253,0.317935, 0.0197911,...
0.337656,0.0196483, 0.357229, 0.0194969,0.376647, 0.019337,...
0.3959, 0.0191687,0.414981, 0.018992,0.433881,0.0188071,...
0.452593, 0.0186139,0.471106, 0.0184127,0.489415,0.0182034,...
0.507511, 0.0179862,0.525385, 0.0177611,0.54303,0.0175283,...
0.560439, 0.0172879,0.577604,0.01704,0.594516,0.0167846,...
0.61117, 0.0165219,0.627558,0.016252,0.643672, 0.015975,...
0.659506,0.0156911,0.675052, 0.0154003,0.690304,0.0151029,...
0.705255,0.0147988,0.7199, 0.0144883,0.73423,0.0141715,...
0.74824, 0.0138485,0.761925,0.0135194,0.775277,0.0131845,...
0.788292, 0.0128438,0.800963, 0.0124976,0.813285,0.0121459,...
0.825253, 0.0117889,0.836861, 0.0114267,0.848105, 0.0110596,...
0.858979, 0.0106877,0.869479, 0.0103111,0.8796, 0.00993,...
0.889337,0.00954459,0.898687, 0.00915502,0.907646,0.00876146,...
0.916209,0.00836409,0.924373,0.00796306,0.932134, 0.00755857,...
0.939489,0.00715079,0.946435,0.00673989,0.952968,0.00632605,...
0.959086, 0.00590946,0.964786,0.00549029,0.970066, 0.00506873,...
0.974923,0.00464496,0.979355,0.00421917,0.98336,0.00379153,...
0.986937,0.00336225,0.990084,0.0029315,0.9928,0.00249948,...

```
 0.995083,0.00206637,0.996932,0.00163236,0.998347, 0.00119765,...
 0.999327,0.000762472,0.999872,0.000327609];

[xi,matder] = chebdif(n,2);
ray=(1+xi)/2;
fid = fopen('tactical_motor_data_uh=0_q=0_new.dat','a');
fprintf(fid,'Title = " small_motor_L/R=24,Ab=2.5, Reynolds=5e3" \n');
%fprintf(fid,'Title = "Data File for hybridat q=1, Reynolds=5e3" \n');
 fprintf(fid,'Variables = "Mb","z", "Omega","RealAlpha","Imaginary Alpha","n","Nozzle
damping","growth_1","growth_2","growth_3","Energy_density","surface_total
growth","Total_solution","error" \n ');
fprintf(fid,'Zone T="q0"\n');
fprintf(fid,'I =42,J=1801,F = POINT \n');
fclose(fid) ;
fid1=fopen('Integral_Data_L_20_tactical_motor_q=0_uh=0_new.dat','a');
fprintf(fid1,'Title = "Small_Motor" \n');
fprintf(fid1,'Variables="Mb","L","Omega","Ab","IA","Nozzle
damping","growth_1","growth_2","growth_3","surface_total
growth","Energy_density","Total_solution","error" \n ');
fprintf(fid1,'Zone T="q0"\n');
fprintf(fid1,'I =42,J=1801,F = POINT \n');
fclose(fid1) ;
cin=3;
for in=21:25
if(in>17)
cin=cin+1;
in=17;
end
alfainitial=complex(alfainitial_r(in),alfainitial_i(in));
%aspect Ratio
% L=10;
Zin=Z_Lo(in);nop=round((L-Zin)/.1+1);
zl=linspace(Zin,L,nop);
wr1=wrr1(in+cin);
Mb=M(in+cin);
for ww=1:1
w=complex(wr1,0);
switch lower(ww)
case 1
alfainitial=alfa;
case 2
alfainitial=alfa11;
case 3
alfainitial=2*alfa22-alfa11;
alfainitial=2*alfa11-alfa22;
%otherwise
```

```
%alfainitial=3*(alfa33-alfa22)+alfa11;
%alfainitial=alfa11-3*(alfa33-alfa22);
% end

for zz=1:nop
z=zl(zz);
switch lower(zz)
case 1
alfa=alfainitial;
case 2
alfa=alfa1;
case 3
alfa=2*alfa2-alfa1;
otherwise
alfa=3*(alfa3-alfa2)+alfa1;
end
er=1;
%  Shooting method to achieve convergence for the eigenvalues using Mullar Method
while(er>1E-8& it<itmax)
it=it+1;
alfa1=alfa;
[solve]=resolcsICCC(alfa1,w,z,npo1,n,q,reynolds);
ur1=solve(1,1);
aur1=abs(ur1);
alfa2=alfa+dval;
[solve]=resolcsICCC(alfa2,w,z,npo1,n,q,reynolds);
ur2=solve(1,1);
alfa3=alfa2+dval;
[solve]=resolcsICCC(alfa3,w,z,npo1,n,q,reynolds);
ur3=solve(1,1);
h1=(alfa2-alfa3);delta1=(ur2-ur3);
h2=(alfa1-alfa3);delta2=(ur1-ur3);
a=(delta1*h2-delta2*h1)/(h1*h2*(h1-h2));
b=(delta2*h1^2-delta1*h2^2)/(h1*h2*(h1-h2));
value1=(2*ur3/(b-sqrt(b^2-4*a*ur3)));
value2=(2*ur3/(b+sqrt(b^2-4*a*ur3)));
alfaa=alfa-value1;
alfab=alfa-value2;
era=abs(value1)/abs(alfa);
erb=abs(value2)/abs(alfa);
if era<=erb;
alfa=alfaa;
er=era;
else
alfa=alfab;
er=erb;
```

```
end
abs(ur3);
end
if (zz = =1)
alfaw=alfa;
end
% Collecting the amplitudes for every eigenvalue at different z locations (spectra
calculations)
for i = 1:n
if ( imag(alfa)<=0)
urs(i,1) = abs(solve(6*(i-1)+1)) ;
uts(i,1) = abs(solve(6*(i-1)+2)) ;
duts(i,1) = abs(solve(6*(i-1)+3)) ;
uzs(i,1) = abs(solve(6*(i-1)+4)) ;
duzs(i,1) = abs(solve(6*(i-1)+5)) ;
ps(i,1) = abs(solve(6*(i-1)+6)) ;
% Calculation the magnitude of each amplitude and the phase angle
urs1(i,1) = (solve(6*(i-1)+1)) ;
thetaur(i,1)=angle(urs1(i,1));
theta(i,1)=angle(solve(6*(i-1)+1));
uts1(i,1) = (solve(6*(i-1)+2)) ;
thetaut(i,1)=angle(uts1(i,1));
theta(i,2)=angle(solve(6*(i-1)+2));
duts1(i,1) = (solve(6*(i-1)+3)) ;
thetadut(i,1)=angle(duts1(i,1));
theta(i,3)=angle(solve(6*(i-1)+3));
uzs1(i,1) = (solve(6*(i-1)+4)) ;
thetauz(i,1)=angle(uzs1(i,1));
theta(i,4)=angle(solve(6*(i-1)+4));
duzs1(i,1) = (solve(6*(i-1)+5)) ;
thetaduz(i,1)=angle(duzs1(i,1));
theta(i,5)=angle(solve(6*(i-1)+5));
ps1(i,1) = (solve(6*(i-1)+6)) ;
thetap(i,1)=angle(ps1(i,1));
theta(i,6)=angle(solve(6*(i-1)+6));
urs(i,1)=abs(solve(6*(i-1)+1)) ;
uts(i,1)=abs(solve(6*(i-1)+2)) ;
duts(i,1)=abs(solve(6*(i-1)+3)) ;
uzs(i,1)=abs(solve(6*(i-1)+4));
duzs(i,1)=abs(solve(6*(i-1)+5));
ps(i,1)=abs(solve(6*(i-1)+6));
end
%to flip the pressure and velocities amplitudes values,
for tt=1:n
pr(tt)=ps(n+1-tt,1);ur(tt)=urs(n+1-tt,1);ut(tt)=uts(n+1-tt,1);uz(tt)=uzs(n+1-
tt,1);duz(tt)=duzs(n+1-tt,1);%wpt(tt)=wpst(n+1-tt,1);
```

```
thetar(tt,:)=theta(n+1-tt,:);
end
% Calculating the n factor
if (imag(alfa)==0|imag(alfa)>0)
ji=0;
kji=ji+1;
alphaii=imag(alfa);
alphair=real(alfa);
end
if imag(alfa)<0
ji=ji+1;
kji=kji+1;
alphai(kji)=imag(alfa);
alphar(kji)=real(alfa);
end
switch lower(ji)
case 0
ni(kji)=0;
nr(kji)=0;
case 1
ni(kji)=-.5*.1*(alphai(kji)+alphaii);
nr(kji)=.5*.1*(alphar(kji)+alphair);
otherwise
nsi=(alphai(kji)+alphaii);
nsr=(alphar(kji)+alphair);
sumi=0;sumr=0;
for mi=2:kji-1
sumi=sumi+2*alphai(mi);sumr=sumr+2*alphar(mi);
end
ni(kji)=-.5*.1*(nsi+sumi);nr(kji)=.5*.1*(nsr+sumr);
end
nf=ni(kji);
nff=nr(kji);
if(ni(kji)>7)
ni(kji)=7;
end
% Saving the amplitudes and the eigenvalues at every axial location in a matrix to utilize
them in the energy calculation
if (imag(alfa)==0|imag(alfa)>0)
aa=zl(zz);
j=0;
k=j+1;
alpha_r(k)=real(alfa);
alpha_i(k)=imag(alfa);
for tt=1:n
```

```
prr(tt,k)=pr(tt);urr(tt,k)=ur(tt);utr(tt,k)=ut(tt);uzr(tt,k)=uz(tt);duzr(tt,k)=duz(tt);thetarr(tt,:,
k)=thetar(tt,:);%wptr(tt,k)=wpt(tt);
end
end
if imag(alfa)<0
b=zl(zz);
m=(b-aa)/2;c=(b+aa)/2;
j=j+1;
k=k+1;
for tt=1:n
prr(tt,k)=pr(tt);urr(tt,k)=ur(tt);utr(tt,k)=ut(tt);uzr(tt,k)=uz(tt);duzr(tt,k)=duz(tt);thetarr(tt,:,
k)=thetar(tt,:);%wptr(tt,k)=wpt(tt);
end
alpha_r(k)=real(alfa);
alpha_i(k)=imag(alfa);
end
% Creating a data file to save the eigenvalues
fid = fopen('tactical_motor_data_uh=0_q=0_new.dat','a');
fprintf(fid,'%10.5f %10.5f %10.5f %15.12f %15.12f %15.12f %15.12f %15.12e
\n',Mb,z,w,real(alfa),imag(alfa),nf,nff,er);
fprintf('%10.5f %10.5f %10.5f %15.12f %15.12f %15.12f %15.12f %15.12e
\n',Mb,z,w,real(alfa),imag(alfa),nf,nff,er);
fclose(fid);
% modifying the initial guesses for the next axial location shooting
switch lower(zz)
case 1
alfa1=alfa;
case 2
alfa2=alfa;
case 3
alfa3=alfa;
otherwise
alfa1=alfa2; alfa2=alfa3;alfa3=alfa;
end
it=0;
end   %end for zz
alfainitial=alfaw;
end  %end of ww
%start surface and volume integral calculations for the motor
%for IA=.001:.0005:.01
IAO=linspace(.00001,.001,25);
%for IA=.00001:.000005:.001
for IAA=1:25
IA=IAO(IAA);
%if(z==L)
switch lower(j)
```

```
case 0
first_term_int=0;
second_term_int=0;
third_term_int=0;
%Energy_den1=0;
Energy_den_ac=5/8*pi*zl(zz);
Energy_den_hyd=0;
Energy_den_total=Energy_den_ac;
 %  energy_denac1=0;
Total_solution=0;
Total_solution1=0;
Energy_nozzle=0;
complete_solution=0;
otherwise
ad=m*t(1,1:2:299)+c;
% round ad to the lowest integer
adi=floor(ad);
% subtract integer values from the real values to collect fractions
add=abs(adi-ad);
% to round the second digit, we multiply the difference by 10
add=add*10;
% round the difference
radd=round(add);
% returne the value back to the second digit
f=radd/10;
% add them to the integer values
nadd=adi+f;
kk=1;
nadd1=nadd(1);
ar(1)=alpha_r(kk);
ai(1)=alpha_i(kk);
nif(1)=ni(kk);
nrf(1)=nr(kk);
for jj=2:150
check=(abs(nadd(jj)-nadd1))*10;
if ( round(check)/10-0.1==0)
kk=kk+1;
nadd1=nadd(jj);
end
if (round(check)/10-0.2==0)
kk=kk+2;
nadd1=nadd(jj);
end
if (round(check)/10-0.3==0)
kk=kk+3;
nadd1=nadd(jj);
```

```
end
if (round(check)/10-0.4==0)
kk=kk+4;
nadd1=nadd(jj);
end
if (round(check)/10-0.5==0)
kk=kk+5;
nadd1=nadd(jj);
end
if (round(check)/10-0.6==0)
kk=kk+6;
nadd1=nadd(jj);
end
kk;
ar(jj)=alpha_r(kk);
ai(jj)=alpha_i(kk);
nif(jj)=ni(kk);
nrf(jj)=nr(kk);
% fit the data at every z step size to 150 points
for tt=1:n
prrr(tt,jj)=prr(tt,kk);urrr(tt,jj)=urr(tt,kk);utrr(tt,jj)=utr(tt,kk);uzrr(tt,jj)=uzr(tt,kk);duzrr(tt,jj
)=duzr(tt,kk);thetarrr(tt,:,jj)=thetarr(tt,:,kk);%wptrr(tt,jj)=wptr(tt,kk);
%prrrq(tt,jj)=prrq(tt,kk);urrrq(tt,jj)=urrq(tt,kk);utrrq(tt,jj)=utrq(tt,kk);uzrrq(tt,jj)=uzrq(tt,k
k);
end
% end of jj loop
end
sum1=0;
sum2=0;
sum21=0;
Energy_den=0;
rb=1;ra=0;
rm=(rb-ra)/2;rc=(rb+ra)/2;
rr=rm*t(1,1:2:299)+rc;
ray1=1-ray;mini=10;
% start of the axial direction loop
for i=1:150
ad_1= nadd(i);
ad_2=nadd(i);
nifr=nif(i);
nrfr=nrf(i);
arr=ar(i);
aii=ai(i);
% start of the radial direction loop
sum3=0;
sum4=0;
```

```
sump=0; %Pressure exit summation
pac=0;
%if (i==150)
% for ii=1:150
%sump=sump+t(1,2*ii)*prrr(ii,i)*ray1(ii);
%end
% pac=-2*rm*sump*cos(arr*ad_1+thetarrr(ii,4,i))*exp(-aii*ad_1);
%end
for p=1:150
for pp=1:n
if(nmini<=mini)
mini=nmini;
pre(p)=prrr(pp,i);ure(p)=urrr(pp,i);ute(p)=utrr(pp,i);uze(p)=uzrr(pp,i);duze(p)=duzrr(pp,i)
;ray11(p)=ray1(pp);thetarrre(p,:)=thetarrr(pp,:,i);%wpte(p)=wptrr(pp,i);
%preq(p)=prrrq(pp,i);ureq(p)=urrrq(pp,i);uteq(p)=utrrq(pp,i);uzeq(p)=uzrrq(pp,i);
end
% end of pp loop
end
pree=pre(p);uree=ure(p);utee=ute(p);uzee=uze(p);duzee=duze(p);r_d=ray11(p);%wptee=
wpte(p);
%  preeq=preq(p);ureeq=ureq(p);uteeq=uteq(p);uzeeq=uzeq(p);
% Start Nozzle exit Calculation
if (i==150)
Nozzle_E=num_evnz(arr,aii,ad_1,r_d,pree,uree,utee,uzee,preeq,ureeq,uteeq,uzeeq,wptee,
Mb,delta);
Nozzle_E=num_evnz11(arr,aii,ad_1,r_d,w,pree,uree,utee,uzee,duzee,thetarrre,p,Mb,delta
,nifr,nrfr,IA,L);
sum4=sum4+t(1,2*p)*Nozzle_E;
%sum4=sum4+Nozzle_E;
% Pressure exit Calculation
sump=sump+t(1,2*p)*pre(p)*cos(nrfr+thetarrre(p,6));
end
% End Nozzle exit Calculation
% Start Energy Density Calculation
% acoustic pressure at the nozzle exit
E=energy_dd(i,q,nifr,nrfr,IA,ad_1,r_d,w,pree,uree,utee,uzee,thetarrre,p,pac,Mb,delta);
sum3=sum3+t(1,2*p)*E;
% End Energy Density Calculation
% end of p loop
mini=10;
end
if (i==150)
Energy_nozzle=rm*sum4;
Pressure_exit=rm*sump;
AO=abs(exp(-nifr)/(Pressure_exit));
end
```

```
Energy_den=Energy_den+t(1,2*i)*rm*sum3;
[first_term,second_term,third_term]=num_ev_mod(aa,q,arr,aii,ad_1,nifr,nrfr,w,Mb,Ab,I
A,gama);
sum1=sum1+t(1,2*i)*first_term;
sum2=sum2+t(1,2*i)*second_term;
sum21=sum21+t(1,2*i)*third_term;
% end of i loop
end
%calculation of acoustic energy
% for ii=0:150
% ad_2=nadd(i);
% arr=ar(i);
% aii=ai(i);
%Energy_den1=m*Energy_den+5/8*pi*ad_1;
Energy_den_ac=5/8*pi*ad_1;
Energy_den_hyd=m*Energy_den;
Energy_den_total=Energy_den_hyd+Energy_den_ac;
first_term_int=m*sum1;
second_term_int=m*sum2;
third_term_int=m*sum21;
Total_solution=2*pi*(first_term_int+second_term_int+third_term_int);
Energy_nozzle=2*pi*Energy_nozzle;
complete_solution=Total_solution/Energy_den_ac;
end % end of switch j loop
fid1=fopen('Integral_Data_L_20_tactical_motor_q=0_uh=0_new.dat','a');;
 fprintf(fid1,'%10.5f %10.5f %10.5f %10.9f %15.12f %15.12f %15.12e %15.12e
%15.12e %15.12e %15.12e %15.12e
\n',Mb,L,Ab,IA,AO,w,Energy_den_hyd,first_term_int,second_term_int,third_term_int,T
otal_solution,complete_solution);
 fprintf('%10.5f %10.5f %10.5f %10.9f %15.12f %15.12f %15.12e %15.12e %15.12e
%15.12e %15.12e %15.12e
\n',Mb,L,Ab,IA,AO,w,Energy_den_hyd,first_term_int,second_term_int,third_term_int,T
otal_solution,complete_solution);
end %IA
end %in
```

F. Eigenvalue Matrix

Program: resolcs
Author: Dr. Casalis and Mr. Abu-Irshaid
Input: Number of points 'n', tangential wave number 'q', frequency 'omega', initial guess for complex eigenvalue 'k', axial location 'z', and Reynolds number 'reynolds', and 'npol' = n-1
Output: The converged value for 'k' and the eigenfunctions in 'solve'
Note: This code builds a matrix in the form of Z'-AZ = 0.

```
[solve]=resolcs(k,omega,z,npo1,n,q,reynolds);
%double precision;
[xi,matder] = chebdif(n,2);
ray=(1+xi)/2;
uh=0;
% n = npol+1 ;
ci = complex(0,1) ;
amat = zeros(6*n,6*n) ;
bvec = zeros(6*n,1) ;
%Classic Hybrid(rotational)
guz = pi*(z+uh)*cos(pi*ray.^2/2) ;
for i = 0:npo1-1
i1 = i + 1 ;
gur(i1,1) = -sin(pi*ray(i1,1)^2/2)/ray(i1,1) ;
end
gur(npo1+1,1) = 0 ;
gut = zeros(n,1) ;
dgut = zeros(n,1) ;
dgur = 2*matder(:,:,1)*gur ;
dguz = 2*matder(:,:,1)*guz ;
dxguz = guz /(z+uh) ;
for i = 1:n-1
% continuity
for j = 1:n
amat(6*(i-1)+1,6*(j-1)+1) = 2*matder(i,j,1) ;
end
amat(6*(i-1)+1,6*(i-1)+1) = amat(6*(i-1)+1,6*(i-1)+1) + 1/ray(i,1) ;
amat(6*(i-1)+1,6*(i-1)+2) = amat(6*(i-1)+1,6*(i-1)+2) + ci*q/ray(i,1) ;
amat(6*(i-1)+1,6*(i-1)+4) = amat(6*(i-1)+1,6*(i-1)+4) + ci*k ;
% derivation of ut
for j = 1:n
amat(6*(i-1)+2,6*(j-1)+2) = 2*matder(i,j,1) ;
end
amat(6*(i-1)+2,6*(i-1)+3) = amat(6*(i-1)+2,6*(i-1)+3) - 1 ;
```

```
% qmt
for j = 1:n
amat(6*(i-1)+3,6*(j-1)+3) = 2*matder(i,j,1) ;
end
amat(6*(i-1)+3,6*(i-1)+1) = amat(6*(i-1)+3,6*(i-1)+1) - reynolds*dgut(i,1) ...
reynolds*gut(i,1)/ray(i,1) + 2*ci*q/(ray(i,1)^2) ;
amat(6*(i-1)+3,6*(i-1)+2) = amat(6*(i-1)+3,6*(i-1)+2) + reynolds*ci*omega ...
- ci*q*reynolds*gut(i,1)/ray(i,1) - reynolds*gur(i,1)/ray(i,1) ...
- (1+q*q)/(ray(i,1)^2) - k*k - ci*k*reynolds*guz(i,1) ;
amat(6*(i-1)+3,6*(i-1)+3) = amat(6*(i-1)+3,6*(i-1)+3) - reynolds*gur(i,1) + 1/ray(i,1) ;
amat(6*(i-1)+3,6*(i-1)+6) = amat(6*(i-1)+3,6*(i-1)+6) - ci*q*reynolds/ray(i,1) ;
% derivation of uz
for j = 1:n
amat(6*(i-1)+4,6*(j-1)+4) = 2*matder(i,j,1) ;
end
amat(6*(i-1)+4,6*(i-1)+5) = amat(6*(i-1)+4,6*(i-1)+5) - 1 ;
% qmz
for j = 1:n
amat(6*(i-1)+5,6*(j-1)+5) = 2*matder(i,j,1) ;
end
amat(6*(i-1)+5,6*(i-1)+1) = amat(6*(i-1)+5,6*(i-1)+1) - reynolds*dguz(i,1) ;
amat(6*(i-1)+5,6*(i-1)+4) = amat(6*(i-1)+5,6*(i-1)+4) + ci*omega*reynolds ...
- ci*reynolds*q*gut(i,1)/ray(i,1) - ci*k*reynolds*guz(i,1) ...
- reynolds*dxguz(i,1) - q*q/(ray(i,1)^2) - k*k ;
amat(6*(i-1)+5,6*(i-1)+5) = amat(6*(i-1)+5,6*(i-1)+5) - reynolds*gur(i,1) ...
+ 1/ray(i,1) ;
amat(6*(i-1)+5,6*(i-1)+6) = amat(6*(i-1)+5,6*(i-1)+6) - ci*k*reynolds ;
% qmr
for j = 1:n
amat(6*(i-1)+6,6*(j-1)+6) = 2*matder(i,j,1) ;
end
amat(6*(i-1)+6,6*(i-1)+1) = amat(6*(i-1)+6,6*(i-1)+1) + q*q/(reynolds*ray(i,1)^2) ...
+ k*k/reynolds - ci*omega - gur(i,1)/ray(i,1) + dgur(i,1) + ci*q*gut(i,1)/ray(i,1) ...
+ ci*k*guz(i,1) ;
amat(6*(i-1)+6,6*(i-1)+2) = amat(6*(i-1)+6,6*(i-1)+2) + ci*q/(reynolds*ray(i,1)^2) ...
- ci*q*gur(i,1)/ray(i,1) - 2*gut(i,1)/ray(i,1) ;
amat(6*(i-1)+6,6*(i-1)+3) = amat(6*(i-1)+6,6*(i-1)+3) + ci*q/(reynolds*ray(i,1)) ;
amat(6*(i-1)+6,6*(i-1)+4) = amat(6*(i-1)+6,6*(i-1)+4) - ci*k*gur(i,1) ;
amat(6*(i-1)+6,6*(i-1)+5) = amat(6*(i-1)+6,6*(i-1)+5) + ci*k/reynolds ;
end
% boundary conditions
switch lower(q)
case 0
% ur(r=0) = 0
amat(6*(n-1)+1,6*(n-1)+1) = 1 ;
% ut(r=0) = 0
```

```
amat(6*(n-1)+2,6*(n-1)+2) = 1 ;
%       p(r=0) = 1
%       amat(6*(n-1)+3,6*(n-1)+6) = 1 ;
%        bvec(6*(n-1)+3,1) = 1 ;
% p(r=1) = 1
amat(6*(n-1)+3,6) = 1 ;
bvec(6*(n-1)+3,1) = 1;
% ut(r=1) = 0
amat(6*(n-1)+4,2) = 1 ;
amat(6*(n-1)+5,6*(n-1)+5) = 1 ;
% end
% uz(r=1) = 0
amat(6*(n-1)+6,4) = 1 ;
case 1
% Dur(r=0) = 0
for j = 1:n
amat(6*(n-1)+1,6*(j-1)+1) = 2*matder(n,j,1) ;
end
amat(6*(n-1)+2,6*(n-1)+3) = 1 ;
% end
% uz(r=0) = 0
amat(6*(n-1)+6,6*(n-1)+4) = 1 ;
% p(r=1) = 1
amat(6*(n-1)+3,6) = 1 ;
bvec(6*(n-1)+3,1) = 1;
% uz(r=1) = 0
amat(6*(n-1)+4,4) = 1 ;
% ut(r=1) = 0
amat(6*(n-1)+5,2) = 1 ;
otherwise
% ur(r=0) = 0
amat(6*(n-1)+1,6*(n-1)+1) = 1 ;
% ut(r=0) = 0
amat(6*(n-1)+2,6*(n-1)+2) = 1 ;
% uz(r=0) = 0
amat(6*(n-1)+3,6*(n-1)+4) = 1 ;
% p(r=1) = 1
amat(6*(n-1)+4,6) = 1 ;
bvec(6*(n-1)+4,1) = 1 ;
% uz(r=1) = 0
amat(6*(n-1)+5,4) = 1 ;
% ut(r=1) = 0
amat(6*(n-1)+6,2) = 1 ;
end
% Inversion amat . Z = bvec
solve = amat\bvec ;
```

G. Hydrodynamic Energy Equation

Program: energy_dd
Author: Mr. Abu-Irshaid
Input: Admitance function value 'Ab', initial amplitude A_0 ='IA', Mach number 'Mb', initial guesses for each motor which include at each Mach number 'Mb': the complex eigenvalue 'k', the critical axial location 'ad', frequency 'w', amplitude values (u_r, u_θ, u_z, p)= 'ur,ut,uz,p', phase angles 'theta', initial amplitude IA, viscous lengthscale 'delta', amplification rate 'ni', and wave number 'nr'
Output: Hydrodynamic energy density E_{hyd} = 'E'

```
[E]=energy_dd(i,q,ni,nr,IA,ad,r,w,p,ur,ut,uz,theta,pc,pac,Mb,delta);

S=w*Mb/Mb;
zz=0.5*pi*r^2;si=-Mb*w/(pi*Mb)*log(tan(0.5*zz));
Ix=zz+1/18*zz^3+7/1800*zz^5+31/105840*zz^7;exc=(w*Mb*delta)^2/Mb^3;
Ip=pi/2+1/18*(pi/2)^3+7/1800*(pi/2)^5+31/105840*(pi/2)^7;
phi=exc/pi^2*(1-1/sin(zz)-zz*cos(zz)/(sin(zz))^2+Ix-Ip);
utr=sin(zz)*exp(phi)*sin(si)*sin(sin(zz)*Mb*w*ad);
uti=-sin(zz)*exp(phi)*cos(si)*sin(sin(zz)*Mb*w*ad);
uh=sin(Mb*w*ad);
ph=cos(Mb*w*ad);
switch lower(q)
   case(0)
E=pi*(IA*p*ph*cos(nr+theta(pc,6))*exp(ni)+(IA)^2/2*p^2*exp(2*ni)...
    +(IA)^2/2*(ur^2+uz^2)*exp(2*ni)+IA*uh*uz*sin(nr+theta(pc,4))*exp(ni)...
    +IA*uz*(utr*cos(nr+theta(pc,4))+uti*sin(nr+theta(pc,4)))*exp(ni))*r;
 otherwise
E=(IA)^2/2*pi*(p^2+ur^2+uz^2+ut^2)*exp(2*ni);
End
```

H. Surface Growth Rate Equation

Program: num_ev_mod
Author: Mr. Abu-Irshaid
Input: Admitance function value 'Ab', initial amplitude A_0 ='IA', Mach number 'Mb', initial guesses for each motor which include at each Mach number 'Mb': the complex eigenvalue 'k', the critical axial location 'ad', frequency 'w', amplitude values (u_r, u_θ, u_z, p)= 'ur,ut,uz,p', phase angles 'theta', initial amplitude IA, ratio of specific heats 'gama', amplification rate 'nifr', and wave number 'nrfr'
Output: Hydrodynamic energy density, $\alpha_{hyd,w}$ = 'first_term+second_term+third_term'

```
[first_term,second_term,third_term]=num_ev_mod(q,ad,nifr,nrfr,w,Mb,Ab,IA,gama);
switch lower(q)
case 0
first_term=(1+Ab)*IA*Mb/(2*gama)*cos(nrfr)*cos(Mb*w*ad)*exp(nifr);
second_term=Mb*(IA)^2/(2*gama^3)*exp(2*nifr);
third_term=Mb*IA/(gama^3)*(cos(nrfr)*cos(Mb*w*ad))*exp(nifr);
otherwise
first_term=0;
second_term=Mb*(IA)^2/(2*gama^3)*exp(2*nifr);
third_term=0;
end
```

I. Discretization Subroutine

Program: chebdif
Author: Dr. Casalis
Input: Number of points 'N', discretized mean flow or amplitude values (for example, M= ut, uz, or Uz) 'M'
Output: Lobatto points 'x', derivatives of M, 'DM' (for example, DM= dut/dr, duz/dr, dUz/dr)

```
function [x, DM] = chebdif(N, M)
I = eye(N);                    % Identity matrix.
L = logical(I);                % Logical identity matrix.
n1 = floor(N/2); n2 = ceil(N/2);    % Indices used for flipping trick.
kk = [0:N-1]';                 % Compute theta vector.
th = kk*pi/(N-1);
x = sin(pi*[N-1:-2:1-N]'/(2*(N-1))); % Compute Chebyshev points.
T = repmat(th/2,1,N);
DX = 2*sin(T'+T).*sin(T'-T);        % Trigonometric identity.
DX = [DX(1:n1,:); -flipud(fliplr(DX(1:n2,:)))];   % Flipping trick.
DX(L) = ones(N,1);             % Put 1's on the main diagonal of DX.
C = toeplitz((-1).^kk);        % C is the matrix with
C(1,:) = C(1,:)*2; C(N,:) = C(N,:);    % entries c(k)/c(j)
C(:,1) = C(:,1)/2; C(:,N) = C(:,N);
Z = 1./DX;                     % Z contains entries 1/(x(k)-x(j))
Z(L) = zeros(N,1);             % with zeros on the diagonal.
D = eye(N);                    % D contains diff. matrices.
for ell = 1:M
D = ell*Z.*(C.*repmat(diag(D),1,N) - D); % Off-diagonals
D(L) = -sum(D');               % Correct main diagonal of D
DM(:,:,ell) = D;               % Store current D in DM
end
```

Vita

Esam Abu-Irshaid received the B.S. degree in Mechanical Engineering from the College of Engineering, University of Mosul. He then participated in a special training program sponsored by the Ministry of Public Works and Housing before beginning his career in HVAC system design and installation at the East-Arabian firm, Jordan. Mr. Abu-Irshaid later received his M.S. degree in thermal science from the Jordan University of Science and Technology (JUST), Department of Mechanical Engineering, in 2000. After graduating from the University of Mosul in 1997, he has served as a Teaching Assistant and a Research Assistant at both JUST and the University of Wisconsin at Milwaukee (UWM). He recently completed another M.S. degree under the supervision of Professor Majdalani in Aerospace Engineering, University of Tennessee (UTSI), Tullahoma, TN. His Ph.D. project involves developing and implementing a hydrodynamic instability algorithm that applies to certain solid and hybrid rockets. His work on hydrodynamic instability has necessitated the development of a code that permits the resolution of instability in injection driven chambers. So far, Mr. Abu-Irshaid has authored seven archival papers; these involve heat transfer from wavy surfaces, permeability experiments, rocket instability, and asymptotic solutions for isentropic flow and shock wave equations across nozzles.